Department of Chemistry
Physical Chemistry

Optical spectroscopy on lanthanide-modified nanomaterials for performance monitoring

Doctoral thesis

in fulfilment of the requirements for the degree
"doctor rerum naturalium"
(Dr. rer. nat.)
in the scientific discipline "Physical Chemistry"

submitted to the
Faculty of Science of the University of Potsdam
by

Sitshengisiwe Chemura

Potsdam, 1 December 2023

Unless otherwise indicated, this work is licensed under a Creative Commons License Attribution 4.0 International.
This does not apply to quoted content and works based on other permissions.
To view a copy of this licence visit:
https://creativecommons.org/licenses/by/4.0

Principal supervisor: apl. Prof. Dr. Michael Kumke

Published online on the
Publication Server of the University of Potsdam:
https://doi.org/10.25932/publishup-61944
https://nbn-resolving.org/urn:nbn:de:kobv:517-opus4-619443

Zusammenfassung

der Arbeit mit dem Titel:

Optical spectroscopy on lanthanide-modified nanomaterials for performance monitoring

eingereicht von Sitshengisiwe Chemura, June 2023, an der Universität Potsdam.

Ceroxid-Nanomaterialien auf Lanthanidbasis sind aufgrund ihrer Redox-Eigenschaften wichtige praktische Materialien, die in der Technik und den Biowissenschaften von Nutzen sind. In dieser Dissertation wurden verschiedene Eigenschaften und das Potenzial für katalytische und biologische Anwendungen von Ln^{3+}-dotierten Ceroxid-Nanomaterialien untersucht. $Ce_{1-x}Gd_xO_{2-y}:Eu^{3+}$, gadoliniumdotierte Ceroxid (GDC) ($0.0 \leq x \leq 0.4$) Nanopartikel wurden durch Flammenspray-Pyrolyse (FSP) synthetisiert und untersucht, gefolgt von 15 % $Ce_xZr_{1-x}O_{2-y}:Eu^{3+}|YSZ$ ($0 \leq x \leq 1$) Nanokompositen. Außerdem wurden $Ce_{1-x}Yb_xO_{2-y}$ ($0.004 \leq x \leq 0.22$) Nanopartikel durch thermische Zersetzung synthetisiert und charakterisiert. Schließlich wurden $CeO_{2-y}:Eu^{3+}$-Nanopartikel durch eine Mikroemulsionsmethode synthetisiert, biofunktionalisiert und charakterisiert. In den durchgeführten Studien wird ein neuartiger Ansatz zur Strukturaufklärung von Nanomaterialien auf Ceroxidbasis mittels Eu^{3+}- und Yb^{3+}-Spektroskopie und Verarbeitung der spektroskopischen Daten mit der Zerlegungsmethode PARAFAC vorgestellt. Für die Entfaltung der Spektren wurden Datensätze mit den drei Variablen Anregungswellenlänge, Emissionswellenlänge und Zeit verwendet.

GDC-Partikel aus FSP sind Nanometer groß und besitzen eine grob kubische Form und Kristallstruktur ($Fm\bar{3}m$). Raman-Daten zeigten vier Schwingungsmoden bei Gd^{3+}-haltigen Proben, während $CeO_{2-y}:Eu^{3+}$ nur zwei aufweist. Die bei Raumtemperatur aufgezeichneten zeitaufgelösten Emissionsspektren bei $\lambda_{Anregung}$ = 464 nm zeigen, dass die Gd^{3+}-Dotierung im Vergleich zu reinem Ceroxid zu deutlich veränderten Emissionsspektren führt. Die PARAFAC-Analyse für die reinen Ceroxidproben zeigt zwei Spezies: eine hochsymmetrische Spezies und eine niedrigsymmetrische Spezies. Die GDC-Proben liefern im selben Experiment zwei niedrigsymmetrische Species. Hochauflösende Emissionsspektren, die bei 4 K nach der Untersuchung des $^5D_0$-$^7F_0$-Übergangs aufgezeichnet wurden, ergaben zusätzliche Variationen bei den niedrigsymmetrischen Eu^{3+}-Stellen in reinem Ceroxid und GDC. Die Daten der Gd^{3+}-haltigen Proben deuten darauf hin, dass die durchschnittliche Ladungsdichte um die Eu^{3+}-Ionen im Gitter in umgekehrter Beziehung zur Gd^{3+}- und Sauerstoffleerstellen-Konzentration steht.

Die Partikelkristallite der bei 773 K und 1273 K geglühten Yb^{3+}-Ceroxid-Nanostrukturen sind nanoskalig und haben eine kubische Fluoritstruktur mit vier Raman-Schwingungsmoden. Elementverteilungen zeigen deutlich, dass sich bei 773 K, geglüht mit einer hohen Yb^{3+}-Ionenkonzentration ab 15 Mol-% im Ceroxidgitter, Cluster bilden. Diese Cluster werden beim Glühen auf 1273 K zerstört. Die Emissionsspektren, die bei Messungen bei Raumtemperatur und 4 K für die $Ce_{1-x}Yb_xO_{2-y}$-Proben beobachtet wurden, weisen vielfältige Banden auf, die dem $^2F_{5/2}$-$^2F_{7/2}$-Übergang der Yb^{3+}-Ionen entspricht. Es werden einige kleine Verschiebungen im Stark-Aufspaltungsmuster beobachtet, die durch die Variationen des Kristallfeldes verursacht werden, in Abhängigkeit der Positionen der Yb^{3+}-Ionen in den Kristallgittern. Beim Mischen von Ceroxid mit hohen Yb^{3+}-Konzentrationen wird der $^2F_{5/2}$-$^2F_{7/2}$-Übergang auch im Stark-Aufspaltungsmuster beobachtet, aber die Spektren bestehen aus zwei breiten, vom Hintergrund dominierten Peaks. Das Ausglühen der Nanomaterialien bei 1273 K für 2 Stunden verändert die spektrale Signatur, da neue Emissionsbanden entstehen. Die Entfaltung ergab die Lumineszenz-Abklingkinetik sowie die begleitenden Lumineszenzspektren von drei Spezies für jede der niedrig Yb^{3+}-dotierten Ceroxidproben, die bei 773 K geglüht wurden, und eine Spezies für die bei 1273 K geglühten Proben. Die bei beiden Temperaturen geglühten Ceroxidproben mit hoher Yb^{3+}-Konzentration ergaben jedoch eine Spezies mit geringeren Abklingzeiten als die Yb^{3+}-dotierten Ceroxidproben nach der PARAFAC-Analyse.

Durch die Kalzinierung der Nanokomposite bei zwei hohen Temperaturen wurde die Entwicklung der Emissionsmuster von spezifischen Eu^{3+}-Gitterplätzen verfolgt, die auf strukturelle Veränderungen der Nanokomposite hinweisen. Die Ergebnisse der Spektroskopie ergänzten die mit den konventionellen Techniken gewonnenen Daten. Das Ausglühen der Proben bei 773 K führte zu amorphen, ungeordneten Domänen, während die totalen Lumineszenzpektren der Nanokomposite bei 1273 K zwei unterschiedliche Stellen erkennen lassen, wobei die meisten rotverschobenen Eu^{3+}-Spezies von reinem Eu^{3+}-dotiertem ZrO_2 auf dem YSZ-Träger stammen.

Schließlich wurde für Eu^{3+}-dotiertes Ceroxid ein erfolgreicher Transfer von der hydrophoben in die Wasserphase und eine anschließende Biokompatibilität mit ssDNA erreicht. Die PARAFAC-Analyse für Eu^{3+} in Nanopartikeln, die in Toluol und Wasser dispergiert wurden, ergab eine Eu^{3+}-Spezies mit leicht unterschiedlichen Oberflächeneigenschaften der Nanopartikel, was die Lumineszenzkinetik und die Lösungsmittelumgebung betraf. Mehrere funktionalisierte Nanopartikel, die nach der Hybridisierung auf Origami-Dreiecken konjugiert waren, wurden mit Hilfe der Rasterkraftmikroskopie (AFM) sichtbar gemacht. Die Eu^{3+}- und Yb^{3+}-Spektroskopie wurde eingesetzt, um die strukturellen Veränderungen zu überwachen und die Möglichkeit des Transfers der Nanopartikel in Wasser zu bestimmen. PARAFAC erweist

sich als ein leistungsfähiges Instrument zur Analyse von Lanthanidenspektren in kristallinen Feststoffen und in Lösungen, die durch zahlreiche Stark-Übergänge gekennzeichnet sind und bei denen Messungen in der Regel eine Überlagerung verschiedener Emissionsbeiträge zu einem bestimmten Spektrum ergeben.

Abstract

of the work titled:

Optical spectroscopy on lanthanide-modified nanomaterials for performance monitoring

submitted by Sitshengisiwe Chemura, June 2023, at the University of Potsdam.

Lanthanide based ceria nanomaterials are important practical materials due to their redox properties that are useful in technology and life sciences. This PhD thesis examined various properties and potential for catalytic and bio-applications of Ln^{3+}-doped ceria nanomaterials. $Ce_{1-x}Gd_xO_{2-y}$: Eu^{3+}, gadolinium doped ceria (GDC) ($0 \leq x \leq 0.4$) nanoparticles were synthesized by flame spray pyrolysis and studied, followed by 15 % $Ce_xZr_{1-x}O_{2-y}$: Eu^{3+}|YSZ ($0 \leq x \leq 1$) nanocomposites. Furthermore, $Ce_{1-x}Yb_xO_{2-y}$ ($0.004 \leq x \leq 0.22$) nanoparticles were synthesized by thermal decomposition and characterized. Finally, CeO_{2-y}: Eu^{3+} nanoparticles were synthesized by a microemulsion method, biofunctionalized and characterized. The studies undertaken presents a novel approach to structurally elucidate ceria-based nanomaterials by way of Eu^{3+} and Yb^{3+} spectroscopy and processing the spectroscopic data with the multi-way decomposition method PARAFAC. Data sets of the three variables: excitation wavelength, emission wavelength and time were used to perform the deconvolution of spectra.

GDC nanoparticles from flame spray pyrolysis are nano-sized and of roughly cubic shape and crystal structure ($Fm\bar{3}m$). Raman data revealed four vibrational modes exhibited by Gd^{3+} containing samples whereas CeO_{2-y}: Eu^{3+} displays only two. The room temperature, time-resolved emission spectra recorded at $\lambda_{excitation}$ = 464 nm show that Gd^{3+} doping results in significantly altered emission spectra compared to pure ceria. The PARAFAC analysis for the pure ceria samples reveals two species; a high-symmetry species and a low-symmetry species. The GDC samples yield two low-symmetry spectra in the same experiment. High-resolution emission spectra recorded at 4 K after probing the $^5D_0$-$^7F_0$ transition revealed additional variation in the low symmetry Eu^{3+} sites in pure ceria and GDC. The data of the Gd^{3+}-containing samples indicates that the average charge density around the Eu^{3+} ions in the lattice is inversely related to Gd^{3+} and oxygen vacancy concentration.

The particle crystallites of the 773 K and 1273 K annealed Yb^{3+} -ceria nanostructure materials are nano-sized and have a cubic fluorite structure with four Raman vibrational modes. Elemental maps clearly show that cluster formation occurs for 773 K annealed with high Yb^{3+} ion concentration from 15 mol % in the ceria lattice. These clusters are destroyed with annealing to 1273 K. The emission spectra observed from room temperature and 4 K measurements for

the $Ce_{1-x}Yb_xO_{2-y}$ samples have a manifold that corresponds to the $^2F_{5/2}$-$^2F_{7/2}$ transition of Yb^{3+} ions. Some small shifts are observed in the Stark splitting pattern and are induced by the variations of the crystal field influenced by where the Yb^{3+} ions are located in the crystal lattices in the samples. Upon mixing ceria with high Yb^{3+} concentrations, the $^2F_{5/2}$-$^2F_{7/2}$ transition is also observed in the Stark splitting pattern, but the spectra consist of two broad high background dominated peaks. Annealing the nanomaterials at 1273 K for 2 h changes the spectral signature as new peaks emerge. The deconvolution yielded luminescence decay kinetics as well as the accompanying luminescence spectra of three species for each of the low Yb^{3+} doped ceria samples annealed at 773 K and one species for the 1273 K annealed samples. However, the ceria samples with high Yb^{3+} concentration annealed at the two temperatures yielded one species with lower decay times as compared to the Yb^{3+} doped ceria samples after PARAFAC analysis.

Through the calcination of the nanocomposites at two high temperatures, the evolution of the emission patterns from specific Eu^{3+} lattice sites to indicate structural changes for the nanocomposites was followed. The spectroscopy results effectively complemented the data obtained from the conventional techniques. Annealing the samples at 773 K, resulted in amorphous, unordered domains whereas the TLS of the 1273 K nanocomposites reveal two distinct sites, with most red shifted Eu^{3+} species coming from pure Eu^{3+} doped ZrO_2 on the YSZ support.

Finally, for Eu^{3+} doped ceria, successful transfer from hydrophobic to water phase and subsequent biocompatibility was achieved using ssDNA. PARAFAC analysis for the Eu^{3+} in nanoparticles dispersed in toluene and water revealed one Eu^{3+} species, with slightly differing surface properties for the nanoparticles as far as the luminescence kinetics and solvent environments were concerned. Several functionalized nanoparticles conjugated onto origami triangles after hybridization were visualized by atomic force microscopy (AFM). Putting all into consideration, Eu^{3+} and Yb^{3+} spectroscopy was used to monitor the structural changes and determining the feasibility of the nanoparticle transfer into water. PARAFAC proves to be a powerful tool to analyze lanthanide spectra in crystalline solid materials and in solutions, which are characterized by numerous Stark transitions and where measurements usually yield a superposition of different emission contributions to any given spectrum.

Table of Contents

Chapter 1: Introduction

An additional specific introduction of the topic is found at the beginning of every chapter.

Advancing ceria-based nanoparticles

In today's world, lanthanide materials have become vital due to their applications in profound and novel technologies. The fact that they have found applications in catalysis, sensors, semi-conductors, insulators, in luminescence-based materials and in biomedical fields such as in magnetic resonance imaging (MRI) agents, proves that they have become indispensable[1-3]. Lanthanide materials have sharp and long-lived excited states of the f-f transitions, retain the benefits of low quantum defect and high conversion efficiency[4,5]. Due to these noble optical properties, they are significant keys in the field of lanthanide luminescence-based materials.

In the last decades, lanthanide material applications have increased across different sectors. Among the lanthanide materials that have found significant attention, ceria is at the center as it is a remarkable versatile material with excellent catalytic capabilities[6,7]. Multiple studies have been devoted to implementing ceria into novel nanotechnologies. Therefore, it has been frequently used in numerous engineering applications, such as, in automotive three-way catalysis[8-10]. Ceria has also been applied in agriculture where for example, the nanoparticles have been used to alleviate nitrogen stress in rice[11]. Recently, ceria in the nanometer size range (nanoceria) was found to be able to mimic multiple types of enzymes due to its ability to cycle between its two oxidation states and thus, it is increasingly becoming a captivating material in the biological field[12-16]. However, used alone, ceria has some limitations for the best applications. Due to these limitations, several lanthanides, tetravalent and transition elements have to be incorporated into the ceria lattice to improve the structural and optical properties. Integrating zirconium into ceria clearly increase both the thermal stability and the catalytic activity of the mixed oxide resulting in fascinating material for solid oxide fuel cell (SOFC) applications[17,18]. Modification of the ceria lattice due to doping with other metal ions results in improved properties, for example for catalysis due to lower operating temperature. Dopants with selected optical properties can be used as a probe to understand or investigate processes on a molecular level. The goal is to produce tailored materials for selected applications. As an example, adding Eu^{3+} in a ceria lattice produces highly luminescent lanthanide-doped ceria nanoparticles[19-21]. Information obtained from Eu^{3+} luminescence can then be used to correlate the structure of the materials and activity when the material is used as a catalyst[21].

It is anticipated that not only does the combination of ytterbium dopant and ceria host (or other host materials) retain almost the same lattice constant as an undoped ceria thereby increasing the ionic conductivity, but can enhance luminescence in the near infrared region, consequently shedding light on the local structure. Yb^{3+} has several noble qualities as it is used as a sensitizer in upconversion

processes[22,23]. Firstly, the Yb^{3+} ion possesses only two electronic states ($^2F_{7/2}$ - $^2F_{5/2}$) and has a very simple energy level scheme. Secondly, the energy of its electronic transitions is in resonance with 976 nm radiation and has a reasonably large absorption cross-section[24]. Thirdly, an energy gap of about 10,000 cm^{-1} between the transitions overlaps with many f-f transitions of typically used Ln (III) ions, allowing efficient energy-transfer upconversion from Yb^{3+} to other ions, among other merits[4,5,25]. In different morphologies, for example where Yb^{3+} ions are incorporated in fluoride and calcium-based materials, clusters of Yb^{3+} ions form even in low doping concentrations, which mostly act as emission quenching centers[26]. It is interesting to note that other lanthanide ions can be added, for example Gd^{3+}, to modify the structures by changing the Yb^{3+} environment, thereby breaking the clusters. Also, annealing the nanomaterials at a high temperature as compared to the synthesis temperature eliminates the luminescence quenching centers[27].

There are several ways that can be used to correlate the catalytic activity of ceria-based materials with the structural properties of the oxides. H_2-temperature-programmed reduction (TPR) experiments can show whether the reduction occurs in the bulk and or on the surface depending on the temperature at which water traces evolve during the experiments[21,28]. This information is useful in determining the effectiveness of the ceria- based catalyst. Overall, depending on the synthesis routes, the precursors used, the amount of dopant used, post thermal treatment after synthesis and the surface modification of the ceria nanoparticles for biocompatibility, high-quality nanomaterials with high luminescence properties and sufficient defect sites where redox reactions during catalysis can occur, can be produced[1,29-31]. These are the factors to consider for a successful and sustainable ceria nanomaterial production.

Due to the interest in lanthanide (Ln^{3+}) doped ceria, many studies have been focusing on the influence of the synthesis approach, on the characteristics of the powders[32,33]. However, there is paucity of information in the investigations of Eu^{3+} doping in mixed oxides (for example in ceria-gadolinium mixed oxides) to understand the structure at the atomic level and also the symmetry at the dopant site (e.g., Eu^{3+}) and how it is dependent on the Gd^{3+} ion concentration. Amorphous materials and those with multiple phases (for example Eu^{3+} doped ceria based nanocomposites) are difficult to analyze using conventional techniques such as X-ray diffraction (XRD)[34]. However, spectroscopic techniques can be used for an in-depth structural analysis on the nano-scale. The unique Eu^{3+} ions' luminescence properties permit the gain of structural insights into amorphous and of course crystalline materials on the atomic level. It was found that the distribution of Eu^{3+} ions over different lattice sites in nanomaterials is strongly reliant on the synthesis and on the thermal treatment of the doped ceria nanomaterials[21].

In substantial communications, up-conversion emission has been used as a probe tool to track Yb^{3+} distribution in the ceria lattice together with other lanthanide ions and corroborate the data from XRD, scanning electronic microscopy (SEM) and Raman on the formation of homogenous solid solutions[35]. Therefore, in this work, reliance of Yb^{3+} spectroscopy on the concentration of only Yb^{3+} ions in the host and on the effect of annealing the nanomaterials at different temperatures was quantitatively investigated in terms of the clustering of Yb^{3+} ions in nanoparticles annealed (at temperatures up to 1273 K in static air). Also, the decay kinetics of Yb^{3+} in ceria-based $Ce_{1-x}Yb_xO_2$ mixed oxides with increasing Yb^{3+} content at two measurement conditions, that is at room temperature and 4 K were studied.

Decades and decades of research have been dedicated on ceria and upconversion nanoparticles in general, for biomedical applications. Although there are many positive reviews on the use of the nanoparticles by utilizing their super antioxidant ability, there have been reports on their restrictions in the biological area usage due to the formation of a protein bio corona, toxicity and low stability restraining the further progression of the nanoparticles to a possible theranostic. Hence, for the efficient medical application of the nanoparticles, it is imperative to find novel ideas which will simultaneously increase the circulation time, reduce the inherent toxicity while preserving the unique catalytic regenerative attributes. Further action has to be done including surface modification with biocompatible agents[36]. DNA nanotechnology could be developed and incorporated in the nanotechnology due to the easy programmability of DNA, its cheap cost of synthesis[37], and ease of chemical modification[38]. In addition to redox reactivity, ceria surface is susceptible to modification by electrostatic interactions, which are the interactions reported to have adsorbed proteins and other biological active materials, thus tailor making the nanoparticles for the required application[39]. Also, the synthesis routes that result in reasonably non-aggregated small nanoparticles produce hydrophobic nanoparticles and ways to convert them into hydrophilic biocompatible nanomaterials are imperative.

Aim and objectives

In this study, fluorescence line narrowing spectroscopy (FLNS) and the parallel factor analysis (PARAFAC) algorithm were used individually and in combination. This was done to achieve two specific goals; (i) develop the combination of techniques into a new tool for the characterization of Ln^{3+}-doped materials to obtain structural information on a molecular level (in contrast to e.g., XRD which give bulk information but no information of minor species) and (ii) connect the gained molecular-level information with macroscopic properties, e.g., catalytic power or the potential improved application in life science,

Specific objectives were to:

i. Synthesize tailored nanomaterials for specific applications.

ii. Structurally elucidate europium-doped $Ce_{1-x}Gd_xO_{2-y}$: Eu^{3+} nanoparticles based on high-resolution emission spectroscopy under cryogenic conditions with special emphasis on using the intrinsic selectivity of the $^5D_0$-$^7F_0$ transition.

iii. Monitor structural changes of Eu^{3+} doped ceria-zirconia multiphase nanocomposites induced by thermal subjection at two temperatures by exploiting the benefits of the combination of ultra-low high-resolution spectroscopy and Eu^{3+} and conventional techniques in probing the samples.

iv. Determine the changes in luminescence properties of Yb^{3+} ion doped in a ceria host lattice at different concentrations and measured at distinct temperatures.

v. Functionalize tailored ceria nanoparticles with ssDNA so as to hybridize them on DNA origami.

State of the art

Chapter 2 presents an introduction to the Ln^{3+} doped ceria nanomaterials that find applications in catalysis and biological applications. A literature review on the different lanthanide dopants that are included in a ceria matrix, the advantages they present, their optical properties, the different synthesis approaches and prerequisites to produce ceria nanoparticles and nanocomposites of high quality is presented. The superiority of ultra-low high-resolution spectroscopy (in some parts referred to as FLNS) over conventional methods is discussed. Surface modification strategies to engineer biocompatible lanthanide doped nanoceria are also presented.

Experimental and characterization methods

In this section, the implemented synthesis protocols, characterization techniques and instrumentation as well as the post data analysis treatment methods used were described.

Results and discussion

This chapter consists of four parts namely:

1. Europium-doped ceria–gadolinium mixed oxides synthesized by a flame pyrolysis method, PARAFAC analysis and high-resolution emission spectroscopy of the Eu^{3+} ions under cryogenic conditions for structural analysis were described.
2. Structural changes induced by post synthesis thermal subjection at two different temperatures on Eu^{3+} doped ceria yttrium stabilized zirconia (YSZ) supported nanocomposites were monitored. The influence on the phases due to the relative amounts of Ce and Zr was determined.

3. Ceria nanomaterials mixed with ytterbium in low and high concentrations were synthesized and the down conversion luminescence of Yb^{3+} ions was analyzed in the near infrared region.
4. Eu^{3+} doped ceria nanoparticles were synthesized for biological applications. A surface modification strategy to make the nanoparticles biocompatible was tested and preliminary studies to conjugate the biocompatible nanoceria to DNA origami were explored.

Summary and conclusions

The thesis conclusion and perspectives are discussed in the final chapter.

Chapter 2: State of the art

2.1 Ceria-based nanomaterial properties and applications

Cerium oxide (ceria, CeO_2) is a rare earth oxide that has found numerous applications in technological and biomedical applications. With increasing environmental consciousness, green energy production has become topical. In this regard, ceria-based oxides have found applications, among others, in SOFCs where they have a great prospect to produce green energy (converting chemical energy of fuels into electrical energy with high efficiency and with negligible green-house gases emission)[40]. The commonly used electrolyte in SOFCs is YSZ. However, its ionic conductivity reaches an optimum at temperatures above 1073 K, which can be difficult to achieve or maintain in other environments[41]. Thus, other electrolyte materials with higher ionic conductivities that could reduce the SOFCs' operating temperature to intermediate temperatures (673−973 K) are being urgently sought, as this could significantly increase their applicability and effectiveness due to reduced thermal stress, longer lifetime and reduced heat loss[42].

Mixing ceria oxide with other metallic elements has been found to be beneficial, thus gadolinium doped ceria (GDC) is suggested as one of the most promising solid electrolyte materials for operation of SOFC operated at intermediate temperature (IT, 873 K − 1073 K)[41,43-46]. The oxygen ion conductivity of GDC and precisely of $Ce_{0.8}Gd_{0.2}O_{1.9}$ is 4-5 times higher than of YSZ at temperatures 773-973 K[46]**.** Also, the conductivity of GDC ($Ce_{0.9}Gd_{0.1}O_{1.95}$) has been reported to be double that of samarium doped ceria (SDC) ($Ce_{0.8}Sm_{0.2}O_{1.9}$) at 873 K[47]. Therefore, there is huge potential for enhancing the catalytic efficiency of these oxides through doping.

There are various schemes that have been employed to improve stability of ceria-based materials under intermediate to high temperature working conditions for best applications. One of those considered and tested for their ionic activities is ceria impregnated on different support materials at a nanoscale. These materials range from ceria nanoparticles supported on YSZ, ceria-zirconia mixed oxides supported on YSZ, on an alumina and silica on surface with the goal of achieving better dispersion of the active phase and improvement of oxygen exchange rate[48]. For alumina supported nanocomposites, the essential stabilization concept is generating a diffusion barrier between neighboring mixed oxide particles, which allows for maintaining dispersion and oxygen storage capacity (OSC)[49]. Anchoring isolated ceria-zirconia nanostructures onto the surface of a support material constitutes an alternative way of implementing this diffusion barrier concept, as long as diffusion at high temperature into the bulk of the carrier material is limited. Useful results have been obtained which can increase the sources for the SOFC materials, thus anchored ceria and ceria−zirconia nanomaterials have been reported to be highly resistant to sintering under reduction−oxidation treatments[50]. Also, strategizing the synthesis in order to prepare ceria and ceria–zirconia supported materials at a low temperature, with total ceria or doped

ceria below 20 % and without noble metals (which are expensive), has been proven to produce materials with high OSC, which are highly reducible and more efficient as a component of oxygen storage formulations[51].

The applications in SOFC rely on oxygen vacancy migration in ceria. Pure ceria contains a fraction of Ce^{3+} ions, resulting in oxygen vacancies in the oxygen sub-lattice to balance the effective negative charge (intrinsic vacancies). However, CeO_2 alone has poor thermal stability and can be easily sintered at high temperature, causing a rapid decrease in its oxygen storage/release capacity and catalytic activity. Also, its ionic conductivity is very low as it is an insulator thus, for its effective use in SOFC, it has to be mixed with other ions[47]. By so doing, further vacancies are introduced.

2.2 Doping with other lanthanides

CeO_2 nanoparticles has a fluorite lattice structure with a face centered cubic cell. The cell is composed of tetravalent Ce^{4+} ions and divalent O^{2-} ions. The balance of the oxygen vacancies and the trivalent Ce^{3+} ions results in defects in the crystal lattice. Oxygen can freely move to fill the oxygen vacancies thus permitting oxygen mobility in the lattice and facilitating the rapid generation of surface vacancy sites. This characteristic facilitates the redox switch between the Ce^{3+} and Ce^{4+} ions enabling redox reactions at the particle surface[16]. For better properties, one of the straightforward ways of modifying ceria's oxygen vacancy defect concentration is by doping[52]. This is where one or more of the cerium atoms are substituted with di- or trivalent ions, especially lanthanides[53,54]. Dopants that have been integrated into the ceria lattice include europium (Eu), gadolinium (Gd), ytterbium (Yb), and zirconia (Zr). Experimental results by Acharya et al. showed that 15 % Gd^{3+} was the optimal dopant concentration for achieving high conductivity as measured by impedance spectroscopy[55]. Besides the dopant concentration, the size of the dopant ions also plays an important role: when the dopant ion radius is close to the radius of the ceria host, then the doped ceria displays high oxygen ion conductivity with the same molar fraction of dopants[33]. Since Eu^{3+} has an ionic radius of 0.1066 nm, which is between that of Ce^{4+} (0.097 nm) and Ce^{3+} (0.1143 nm), extensive solubility within the ceria lattice is promoted[53]. Also, the high O^{2-}-conductivities recorded in gadolinium doped ceria (GDC) have been linked to the ionic radius of the Gd^{3+} ion (0.105 nm), which is close to radius of Ce^{4+} ion (0.097 nm)[44,56]. Although pure ceria is known for antioxidant activity, based on the Ce^{3+}/Ce^{4+} ratio, it is possible to increase this ratio and thus enhance the catalytic activity. Therefore, doping ceria with Zr^{4+} would also increase the Ce^{3+}/Ce^{4+} ratio and increase the number of defect sites in the nanomaterials, thereby increasing the catalytic ability. Given the potential of GDC in SOFC applications, many studies have been carried out to understand and develop frameworks for its applications. For example using computational methods, Lucid, et al. [44] studied the structure and reducibility of CeO_2 doped with lanthanide ions and established that the defect structure is principally dependent on the ionic radius of the dopant cations.

Introducing Yb^{3+} ions in the ceria lattice is also an advantage as it has an ionic radius of 0.0985 nm which is close to that of Ce^{3+} and Ce^{4+} ions. Thus, by doping, there is the possibility of the enhancement of optical and catalytic properties due to the increment of oxygen vacancies created to maintain the charge neutrality in the lattice through the insertion of one or more Ln^{3+} ions. Owing to that phenomenon, there is the reduction of Ce^{4+} to Ce^{3+} [57]. Such vacancy provides an increase in the active sites for oxidative species to undergo catalytic reaction and also for execution of antioxidant activity in medical applications[58].

Upon doping ceria with Ln^{3+} ions, the site preference of oxygen vacancies as nearest neighbor (NN) or next-nearest-neighbor (NNN) to the dopant ion is determined by the strength and nature of their interaction, both of which rely on dopant ion size. Thus, Ln^{3+} ions with ionic radii greater than Gd^{3+}, such as Eu^{3+}, favor the oxygen vacancy in the NNN position, while those smaller than Gd^{3+} favor the NN position[21,59-61]. Theoretical studies on trivalent lanthanide doped ceria have shown that doping with smaller trivalent ions induces more oxygen vacancies and these vacancies are associated with the dopant ions.[13–15] Zhang et al. have also reported that trivalent lanthanide ions smaller than Sm^{3+} tend to form oxygen vacancies as their NN or associated with dopants while larger trivalent ions formed oxygen vacancies as the NNN[62].

As doping is often used to tailor the properties of ceria for different applications, it can furthermore be used as a way of introducing luminescence properties. Sorbello et al.studied the structural variation of Ce-Gd^{3+}-Eu^{3+} oxide phosphors at a fixed Eu^{3+} doping of 5 mol % with respect to the application as a bio-probe, and concluded that up to a molar fraction of 20 % of Gd^{3+} in the host lattice, a cubic structure was found to be stable (space group $Fm\bar{3}m$) [55]. At the same time Eu^{3+} ions are powerful structural probes, as they can provide information about the crystal field symmetry and strength determined by their local environment, and they allow to monitor even small changes in that environment, based on Judd-Ofelt theory[63,64]. Yb^{3+} ions also work as a luminescence probe showing near infra-red (NIR) emission and it has also found applications as a sensitizer in upconversion (UC) mechanisms where it is reliably excited and then non-radiatively transfers the energy to an activator ion[65,66].

2.3 Preparation strategies of ceria-based nanomaterials

The lanthanide ion doped oxides of ceria have been synthesized via different routes including co-precipitation[41,56,67] the hydrothermal synthesis[68], EDTA-citrate complexing method[33], sol-gel synthesis[69], flame spray pyrolysis[46], via solid-state reaction[59], thermal decomposition, microemulsion and impregnation. The advantage of the flame spray synthesis process is its potential to produce sophisticated material at high production rates[70]. Additionally, even on pilot-plant scale process conditions can be varied to adjust the material properties. This method produces small crystalline nanoparticles obtainable in a one-step process by optimizing the flame spray pyrolysis parameters[46,71].

Thermal decomposition method yields small and highly monodisperse nanoparticles with high crystallinity and good morphology that can be bio-conjugated for biological applications[72-74]. The impregnation technique is a well-known and effective procedure in the formulation of heterogenous catalysts[75,76]. It has wide application in preparing supported nano-catalysts as it is easy to control and shows reliable reproducibility[77]. Microemulsion presents also as a low-cost effective method for synthesizing small and highly monodisperse nanoparticles[78,79] . As the synthesis methods are important in the design and fabrication of ceria nanomaterials, it is imperative to choose a method that offers a great advantage in terms of cost, large surface area, and flexibility on choosing dopant materials, high yield and flexibility in the surface modifications for best applications.

2.4 Influence of Ln^{3+} doping concentration

The amount of dopant in a nanoparticle matrix has an influence on the structural properties, and on luminescence properties. A decrease in the particle size and an increase in lattice parameter of the Yb^{3+} doped ceria nanoparticles synthesized with an increase in the dopant concentration was observed[17]. The explanation was that doping with slightly larger sized Yb^{3+} ions increase the lattice parameter of ceria and with increasing of Yb^{3+} ion concentration the cubic ceria lattice will expand. However, results from Babu et al. are in contradiction, where they found out that there is lattice contraction with increasing the amount of Yb^{3+} ions in the ceria lattice[80]. This was also experienced with introducing more and more Sm^{3+}, Gd^{3+} and Eu^{3+} in the ceria matrix, although the degree of the lattice parameter changes with the trivalent dopant[81,82]. It therefore remains a subject of research to find out what circumstances or synthesis procedures which would make results converge towards decrease or increase of lattice parameters in response to doping with Yb^{3+} ions.

Different crystal symmetries are identified with different dopant concentrations through following the sample matrices' luminescence processes. With Yb^{3+} ions doped in a CaF_2 matrix, Petit et al. identified three dominant types of Yb^{3+} isolated ion centers even at very low dopant concentration (circa 0.03 at. %), which are cubic, tetragonal and trigonal symmetries[26]. However, upon introducing the Yb^{3+} ions in the matrix at high concentrations, only one dominant class of Yb^{3+} center was identified corresponding to some hexameric cluster whereby the Yb^{3+} ions are found in nearly tetragonal crystal-field environments. Depending on the doping levels, different spectral signatures are obtained. For 1–4 mol % in their Gd_2O_3:Yb^{3+} phosphor, Tamrakar et al. observed no apparent emissions in the near infra-red (NIR) region and they only detected emission after 5 mol %[4]. Nevertheless, the NIR emission due to Yb^{3+} ion increases with increasing Yb^{3+} ion concentration[4]. Cluster formation occurs as Yb^{3+} concentration increases, resulting in Yb^{3+} -Yb^{3+} pairs, thus reducing the emission of isolated Yb^{3+} ions[4]. When the doping concentrations of Yb^{3+} ions are relatively low the decay times are long, showing a slow rate of energy migration between the isolated Yb^{3+} ions[1]. In contrast, when the doping concentrations are further elevated from 20 mol % up to 100 mol %, Mei et al. observed that the Yb^{3+}

ions in their samples showed small decay time values[2]. So generally, doping concentrations have an effect on the spectral signatures and the decay times for the ions in different lattice sites. Upon increasing the Ln^{3+} doping levels in CeO_2 host lattice, internal defects within can also act as luminescence quenching sites[1].

In upconversion (UC) luminescence studies, there is an optimum Yb^{3+} ion doping concentration that results in a maximum upconversion emission intensity. However, past that optimum, there is high possibility of aggregation of Yb^{3+} ions leading to the birth of quenching centers. By so doing, the Yb^{3+} ions may act as trapping centers prompting luminescence quenching[35,83]. Han et al. observed that emission intensity initially increases and then decreases with increasing Yb^{3+} doped concentrations in ceria[84].

2.5 Effect of calcination on the nanomaterials

The temperature at which nanomaterials are post treated after synthesis has an effect on their structural and subsequently also on their luminescence properties. While producing only minor structural changes, the addition of dopants significantly altered the optical properties of the Ln^{3+} doped ceria nanocubes[1]. The annealing process plays a crucial role in removing both oxygen vacancies and undesired impurities from the reactions occurring during the synthesis of the nanomaterials for example nitrates, carbonates and remaining H_2O. When calcination temperature increased, CeO_2: Er/Yb particle size, lattice parameter and the ratio of surface adsorption oxygen to lattice oxygen increased gradually[84]. Crystallization through annealing of YSZ films obtained by deposition using wet chemical techniques and at low to intermediate temperatures, results in changes in the amorphous character and that of the phases originally present. However, the conversion to more stable, but simultaneously phases of lower symmetry require a high calcination temperature[85].

Luminescence properties also change with calcination. Defects and imperfections are removed from the lattice of the ceria nanomaterials after calcination and evidence of migration of the surface Eu^{3+} inside ceria fluorite structure has been observed through luminescence measurements[86]. With Eu^{3+} doped as-synthesized ceria and ceria-zirconia mixed oxide samples; very broad Eu^{3+} ions' excitation and emission peaks with strong variations in the crystal field strength and no distinct, sharp emission or excitation bands have been observed. This is reported to be as a result of pronounced amorphous character of the particles before annealing[21]. With charge transfer (CT) excitation of high temperature annealed samples (for example at 1273 K), a bathochromic shift of the band is observed and additional species can be excited via CT excitation. Primus et al. also observed that the asymmetry ratio, R increases with the annealing temperature[21]. Annealing temperature also totally changes the total luminescence spectra (TLS) as a result of full nanoparticle crystallization leading to a consequent redistribution of the Eu^{3+} dopants over well-defined lattice sites. With the Gd_2O_3:Yb^{3+} phosphor, luminescence intensity was

observed to become higher with increasing annealing temperature[4]. This is envisaged to be due to lattice distortion which is eliminated by heating to a higher temperature and promoting crystallite growth, which in turn is responsible for the enhancement of NIR emission. Annealing Yb^{3+} doped CaF_2 crystals in inert atmosphere also results in the reduction of Yb^{3+} to Yb^{2+} and this also reported for $BaZrO_3$:$Yb3^{+}$ after a calcination temperature of 1273 K[27].

2.6 Optical properties of dopants in different matrices

2.6.1 Eu^{3+} optical properties

The exceptional luminescence properties of Eu^{3+} allow structural understanding of amorphous and crystalline nanomaterials on the atomic level[87,88]. Judd–Ofelt theory stipulates that the emission spectra of Ln^{3+} dopants, in this case, Eu^{3+}, are determined by their particular atomic surroundings that is by the crystal field symmetry and strength[20]. It has been shown that the emission characteristics of Eu^{3+} are sensitive to its local environment[89] and the emission has been monitored to understand the changes in the local structure due to trivalent ion doping as well as subsequent co-doping with vanadium[62]. The trivalent Eu^{3+} ion is a conventional activator for red-emitting phosphors and also a sensitive probe of lattices[90]. It is known not only as a result of its red luminescence, but also the narrow transitions in the luminescence spectra. The spectroscopic data obtained relays information on the point group symmetry of the Eu^{3+} site in this case, referred to as species. A species is a homogeneous group of Eu^{3+} ions that are found on defined, iso-symmetric lattice sites[20].

2.6.2 Eu^{3+} ion transitions

Materials doped with Eu^{3+} ions show photoluminescence, due to the transitions from the $^5D_0$ excited state to the J levels of the ground term ^7F (J = 0– 6). The occurrence of the $^5D_0$ -$^7F_0$ transition (strictly forbidden based on the Judd–Ofelt theory) implies that the Eu^{3+} ion occupies a site with C_{nv}, C_n or C_s symmetry. Owing to the non-degeneracy in the ground state ($^7F_0$) and the first excited state ($^5D_0$) of Eu^{3+}, the resultant electronic transition of a particular Eu^{3+} species comprises of only one single peak[21]. The observation of more than one peak in this spectroscopic region shows that more than one species is present[91]. The magnetic dipole (MD) transition ($^5D_0$ -$^7F_1$) is largely independent of the environment of the Eu^{3+} ion and reveals the crystal-field splitting of the $^7F_1$ level. This crystal field splitting is measured by using the crystal field splitting parameter (N_v (B_2q)). This parameter, is frequently used to reliably and uniformly compare the effect of the surrounding lattice on different ions doped in a host with different site symmetries[92,93]. It is calculated as[92]:

$$N_v(B_{2q}) = \sqrt{\pi.\frac{(2+\alpha^2)}{0.3}}.\Delta E \qquad [1]$$

Where $\alpha = (E_{b-}\ E_2\ )/(0.5.\Delta E)$ [2]

E_b being the average of the energies of the 3 Stark levels in the $^5D_0$-$^7F_1$ transition,

$$\Delta E = E_3 - E_1 \quad [3]$$

and E_2, the energy possessed by the central stark level in the $^5D_0$-$^7F_1$ transition.

When a Eu^{3+} ion site in a centrosymmetric environment, the $^5D_0$-$^7F_1$ transition is the most intense of all transitions observed. As with the $^5D_0$-$^7F_0$ transition, the existence of more than three lines for this transition indicates the presence of more than one Eu^{3+} species. The $^5D_0$-$^7F_2$ transition, also known as the "hypersensitive transition", has its intensity influenced by the local symmetry of the Eu^{3+} ion and the nature of the ligands[91]. When the $^5D_0$-$^7F_0$ transition is observed along with a highest intensity of the $^5D_0$-$^7F_2$ transition, then Eu^{3+} ions occupy a non-centrosymmetric site with symmetry C_s, C_n or C_{nv}[94]. Eu^{3+} ions at the Y: C_n sites in a Eu^{3+}-doped $YSiO_2N$ sample have been reported to show intense $^5D_0$-$^7F_2$ electric dipole luminescence which is a result of the lack of inversion center[95,96].

The Eu^{3+} ions' $^5D_0$-$^7F_3$ transition is generally very weak as it is forbidden according to the Judd–Ofelt theory, and can gain intensity only via J-mixing. Luminescence can also originate from the $^5D_1$, $^5D_2$ and $^5D_3$ levels, the higher emission excited states. According to Binnemans, the $^5D_0$-$^7F_4$ transition should be compared to the intensity of the $^5D_0$-$^7F_1$ transition and not considered in terms of absolute values as it is found in a spectroscopic region where most photomultiplier tubes have a low sensitivity[97]. Finally, the transitions $^5D_0$-$^7F_5$ and $^5D_0$-$^7F_6$ are infrequently seen as they are out of range of the measurement by most spectrofluorimeters, and if they are measurable, in most instances, have very low intensities. With Eu^{3+} spectroscopy, one can determine the point group symmetry of the Eu^{3+} site by counting the number of crystal-field components that are observed in individually probed species for the transitions $^5D_0$ - ^7F_J.

2.6.3 The asymmetry ratio, R

The asymmetry ratio (R), is a parameter frequently used to approximate the degree of inversion symmetry in a coordination polyhedron or how much a site is distorted and it clearly identifies the high symmetry data[20,91]. Mathematically, it is defined as the integrated intensity ratio between the hypersensitive electronic dipole transition, the $^5D_0$ - $^7F_2$ and the magnetic dipole transition $^5D_0$ - $^7F_1$ (around $\lambda_{emission}$ = 610 nm), that is:

$$R = \frac{I(^5D_0 - ^7D_2)}{I(^5D_0 - ^7D_1)} \quad [4]$$

2.6.4 The Judd–Ofelt (JO) intensity parameters

The JO parameters provide an insight into the local structure and bonding in the vicinity of rare earth ions[98-100]. The JO parameters, that is the oscillator strength, photoluminescence branching ratios (β_k), excited state radiative lifetimes (τ), radiative transition probabilities (A) and emission cross-sections are predicted by using only three intensity parameters: Ω_2, Ω_4 and Ω_6[94]. To calculate the JO parameters, the dipole strength, D, of Eu^{3+} is derived from the MD transition and can be calculated and used as a reference for transitions originating from the $^5D_0$[101,102].

Therefore, $D_{MD} = 9.6 \times 10^{-42}\ esu^2cm^2 = 9.6 \times 10^{-6}\ Debye^2$ [5]

Reduced matrix elements $|\langle J|U^{\lambda}|J'\rangle|^2$ are abbreviated as U^{λ} for λ = 2, 4, 6

$$U^2 = 0.0032 \quad [6]$$

$$U^4 = 0.0023 \quad [7]$$

$$U^6 = 0.0002 \quad [8]$$

U^{λ} for the electric dipole transitions originating from the $^5D_0$ are zero, except to the levels $^7F_{\lambda}$.

The experimental dipole strengths of the transitions are defined by three parameters Ω_{λ} where λ = 2, 4, and 6 and is calculated as:

$$\Omega_{\lambda} = \frac{D_{MD}v_1^3}{e^2v_{\lambda}^3U^{\lambda}} \frac{9n^3}{n(n^2+2)^2} \frac{J_{\lambda}}{J_1} \quad [9]$$

where $J_k = \int I_k(\tilde{\upsilon})d\tilde{\upsilon}$ is the integrated intensity of the transition $^5D_0$-^7F_k and $\tilde{\upsilon}_k$ is the average wavenumber in cm^{-1}, the barycenter of the transition to the ^7F_k level:

$$\tilde{\upsilon}_k = \frac{\int \tilde{\upsilon} I_k(\tilde{\upsilon})d\tilde{\upsilon}}{J_k} \text{ (for k = 1,2,4,6)} \quad [10]$$

Thus, radiation transition probabilities, A_k is calculated as:

$$A_k = \frac{64\pi^4\tilde{\upsilon}_{\lambda}^3}{3h} \frac{n_{\lambda}(n_{\lambda}{}^2+2)^2}{9} D_{ED}^{\lambda},\ A_1 = \frac{64\pi^4\tilde{\upsilon}_1^3}{3h} n_1^3 D_{ED}^{\lambda} \quad [11]$$

where the dipole strengths of the ED transitions for Eu^{3+}, $D^{\lambda}{}_{ED} = e^2\Omega_{\lambda}U^{\lambda}$, (e = $4.803\times 10^{-10}\ esu$) is the elementary charge, h, the Planck's constant ($6.63\times 10^{-27}\ erg.s$) and $1\ erg = 10^{-5}Ncm$.

The total radiation transition probability, A_R, is the sum of all radiation transition probabilities given by:

$$A_R = \sum_{\lambda = 1,2,4,6} A_k \quad [12]$$

The radiative lifetime, τ_R, is the reciprocal of the total radiative decay rate (A_R) that is:

$$\tau_R = \frac{1}{A_R} \quad [13]$$

Then non-radiative probability, A_{NR} is calculated as: $A_{NR} = \frac{1}{\tau} - A_R$ [14]

And finally, the emission quantum efficiency, $\eta = \frac{A_R}{A_R + A_{NR}}$ [15]

These JO parameters are now easily calculated using software[101].

2.7 Information obtained from Eu^{3+} ion spectra

By using Eu^{3+} spectroscopy in probing structural properties, information on the homogeneity of a distinct lattice site can be obtained[21]. Through recording a three- dimensional plot (total luminescence spectra, TLS) for the Eu^{3+} ions in the investigated samples, different environments where Eu^{3+} is found can be easily identified[103]. TLS are acquired by scanning over the $^5D_0$-$^7F_0$ transition absorption range (y-axis) and simultaneously recording the emission spectra (x-axis). The spectra are plotted by translating the emission intensities to a color scale from the lowest to the highest intensities (Z axis). From the $^5D_0$-$^7F_0$ excitation spectrum, the degree of inhomogeneity (for instance small variations in bond lengths, bond angles) can be evaluated[93]. Using the TLS approach, each Eu^{3+} species excited via its particular $^5D_0$-$^7F_0$ absorption will display as bright spots in the TLS. The number of these well-defined species appearing at different excitation wavelengths and the broadening in excitation and emission shows the homogeneity of a probed lattice site. When a site with a specific symmetry is more homogeneous, then the peaks are sharper and vice versa, while retaining the same splitting pattern[21]. Small variations in the crystal field strength and symmetry results in broadened excitation and emission bands. Also, spectral band broadening is encountered when measurements are carried out at room temperature[93].

It is of importance to note that in order to gain a full insight into Eu^{3+} luminescence spectroscopy results for speciation analysis, the need to curb the effect of inhomogeneous broadening cannot be overemphasized and that the measurements have to be performed under site-selective excitation conditions to produce detailed information on the species distribution in a given material[20,103,104]. These fundamentals can be achieved when working under cryogenic conditions (temperatures less than 10 K)[91] and exciting the Eu^{3+} ions in the samples using a tunable, narrow-bandwidth laser[93]. The respective emission splitting patterns of each species that can be obtained without mixing of emission profiles originating from another species contain information about the site symmetry, thus other variables; spectral broadening, asymmetry ratio, and the Stark splitting patterns where site-selective excitation is carried out can consequently be explored[20].

Eu^{3+} dopants in ceria can be electronically excited via direct or indirect excitation routes. In the former case there is excitation of one of the many f−f absorption bands Eu^{3+} exhibits in the UV-Vis spectral range. For example, the $^5D_2$–$^7F_0$ transition at around 464 nm, the $^5L_6$–$^7F_0$ excited at about 394 nm and $^5D_0$–$^7F_0$ transition around 580 nm, which is used for site-selective excitation with a narrow-bandwidth laser source[88]. Indirect excitation of Eu^{3+} doped ceria via the Ce^{4+}–O^{2-} charge transfer (CT) band ($\lambda_{excitation}$ = 280−375 nm) results in a sensitization of Eu^{3+} dopants[95]. Primus et al. observed that CT excitation results in narrowed emission bands, signifying that the energy transfer from a Ce^{4+}–O^{2-} pair to Eu^{3+} is only probable in very ordered, homogeneous environments[21]. With this information, a conclusion that CT excitation shows some degree of selectivity on the basis of the sensitization mechanism via the Ce^{4+}–O^{2-} absorption was reached[21]. Depending on the excitation route and measurements conditions, the splitting of the excited levels differs for different lattice sites in nanomaterial samples, resulting in the excitation of multiple sites. The emission lines from different sites superimpose, thus requiring extensive and careful data analysis for acceptable conclusive results as opposed to the $^5D_0$-$^7F_0$ excitation, which is inherently selective and make no room for doubtful results[20].

The formation of different crystalline phases, high resolution spectroscopy is established to be a powerful analytical approach in studying nanoparticles and analyzing host lattice effects. The results obtained, based on its sensitivity and selectivity overrides that from the conventional methods (e.g., XRD). For Eu^{3+} doped CeO_2 nanoparticles, the phase transformation upon annealing could be observed and successfully linked to the nanomaterials' catalytic properties [20,21]**.** Tiseanu et al. reported that the luminescence data they recorded after annealing their ceria based nanocrystals, revealed the existence of several Eu^{3+} species; one of high-symmetry with almost temperature independent physical properties and one or more distorted Eu^{3+} species siting on surface or inner sites with strongly temperature dependent properties [86].

Luminescence measurements can be carried out at room temperature or under cryogenic conditions (ultra-low temperatures). Although invaluable information is obtained from room temperature measurements, these studies are complicated by the difficulty in separating luminescence signals emanating from different Eu^{3+} sites as a result of spectral broadening when using conventional emission spectroscopy[93]. Also, energy transfer phenomena, spectral overlap in excitation and emission amounts to an uncertainty for the interpretation of the spectroscopic results. Though some information about the decay kinetics of the Eu^{3+} species in a probed lattice can be estimated by using standard software packages, e.g., the Origin software, some errors especially human errors can lead to over or underestimation of the results. However, to curb the occurrence of this phenomena, in this thesis, a parallel factor (PARAFAC) analysis algorithm have been suggested and executed to partly separate the emission spectra.

2.8 Yb^{3+} optical properties

In luminescence upconversion materials based on lanthanides, the Yb^{3+} ion is a frequently used sensitizer due to its decent absorption of 10^{-20} cm^{-2} at around 980 nm[105]. In such materials the down conversion luminescence of Yb^{3+} is rarely investigated, instead the luminescence of the activator ions (Er^{3+}, Tm^{3+} or Ho^{3+}) is detected[106]. For the measurement of the down conversion luminescence of Yb^{3+} ions, standard detectors are often not suited since the quantum efficiencies of the respective photo-responsive material is very low, but with the latest generation of electron multiplying charge coupled device (EMCCD) cameras, the NIR spectral range is now accessible.

Yb^{3+} can exhibit sharp luminescence emissions via intra-4f or 4f-5d transitions and since it is excitable in higher wavelength regions, highly desired imaging in NIR region is enabled[107]. Yb^{3+} ion has only two states; the electronic ground and excited states assigned to the $^2F_{7/2}$ and $^2F_{5/2}$ state, respectively[2,25,27].These two states can be further split into different Stark level multiplets subject to the crystal field, thus the transitions between the splitting levels are sensitive to the lattice site environment although it has also been shown to be sensitive to temperature[108]. As an example, at a low C_S symmetry, the ground state $^2F_{7/2}$ can split into four and the excited state $^2F_{5/2}$ into three Kramer's doublets[2,4,26,109,110]. Figure 1 shows the splitting that can happen due to the thermal vibrations of the crystal lattice.

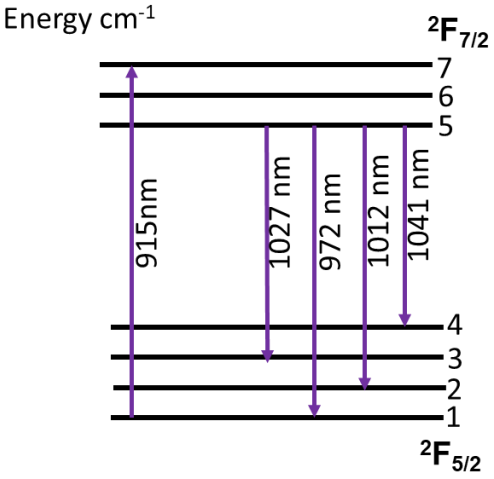

Figure 1. Crystal field energy level scheme for Yb^{3+} ions (Adapted from Tamrakar et al[4] and Mei et al[2])

The intra-configurational f- f transitions are projected to be relatively sharp, however, in some materials broader bands are also observed. In case of Yb^{3+}, they might be attributed to charge transfer transitions (an assignment to inter-configurational d-f transitions seem to be unrealistic since the d-levels are expected at very high energies; in case of Yb^{2+} the situation is different)[24] . The emission and absorptions lines of the Yb^{3+} ions when they site in different environments (cubic (O_h), tetragonal (C_{4v}) and trigonal C_{3v} environments) during crystal growth have been recorded. Table 1 displays the emission lines obtained for Yb^{3+} ions in different symmetry environments.

Table 1. Emission lines obtained for Yb^{3+} ions in different symmetry environments[26]

Symmetry	Emission lines observed (nm)						
O_h	922	963	1027	1019	1041		
C_{4V}	930	968	1012	1019	1026		
C_{3V}	961	975	987	1011	1038	1068	1107
	968	986	999	995			

2.9 Clustering tendency of Yb^{3+} in materials

Trivalent rare-earth ions doped nanomaterials are susceptible to form clusters structure that contain at least two rare-earth ions in close environments in high amounts in crystal lattices and even in low dopant concentrations (e.g. $Yb^{3+}{}_{(mol\ \%)} > 0.05\ \%$)[25]. Depending on the doping amount, the type of lanthanide ion, and the post synthesis thermal treatment of the crystal lattice, the resulting clusters which act as quenching centers, can be dimeric, trimeric, hexameric, or even higher[5,26]. Internal defects inside a CeO_2 lattice created as a result of doping, can act as quenching sites at high Yb^{3+} concentrations[1]. Mixing Yb^{3+} at high concentration in the lattice can also cause a decrease in luminescence because of the aggregation of Yb^{3+} ions and close distance between the ions. Yb^{3+} clusters can likewise act as trapping centers resulting in a fast non-radiative decay from Yb^{3+} ion clusters[35,83]. The influence of doping amount on clustering, and the characterization of typical lines in the absorption and emission spectra was intensively studied for Yb^{3+} doped CaF_2 [111,112]. Characteristic absorption profiles vary with the local symmetry of the Yb^{3+} ion the distribution, thus for Yb^{3+}-doped cubic phase lattice matrices exhibiting high symmetry, cubic centers (O_h) are formed consisting of an F^--cage with an Yb^{3+} ion siting in the center[113].

2.10 Cooperative luminescence

Cooperative luminescence or transition refers to processes where two Yb^{3+} ions emits one photon by simultaneous radiative relaxation from their excited states and this happens in the spectral regions where these individual ions do not have absorption or emission[25,114]. The 4f electrons of Yb^{3+} ions interact strongly with its surrounding, but that interaction is comparatively stronger with neighboring Yb^{3+} than other rare earth ions. It is reported that this instantaneous de-excitation of a pair of excited Yb^{3+} ions accompanied by the emission of a visible photon may be responsible for the blue emission around 488 nm[115]. Multi-ion cooperative processes were also observed from Yb^{3+} ion clusters in a CaF_2 matrix

where NIR excitation resulted in UV emissions[25]. The Yb^{3+} ions' narrow-band excited state ($^2F_{5/2}$) is metastable with a lifetime of up to a few ms, increasing its probability of interacting with the neighboring ground-state Yb^{3+} ions. When this happens, it quickly transfers its excited energy instead of producing radiative emission. Simultaneously, the other nearby Yb^{3+} ions are affected in a cascade fashion when any type of phonon coupling of an excited state Yb^{3+} ion occurs inside the lattice. In this case, the multi-parameter Yb^{3+} spectroscopy quickly amplifies displaying the quenching of one excited Yb^{3+} ions and activation of another Yb^{3+} ions to an excited state[2]. Annealing nanoparticles containing Yb^{3+} results in improved crystalline structure and removes some of the quenching centers resulting in intensification of high temperature annealed samples' NIR emission[27].

2.11 Post spectroscopic data treatment: PARAFAC analysis

The PARAFAC model is used to deconvolute time delay and excitation dependent emission data into several species, based on the understanding that the total measured emission spectrum is the superposition of the weighted single species spectra[116,117]. This way it is possible to deconvolute the data into the pure decay function, excitation spectrum and emission spectrum (depending on the data set) of each pure Eu^{3+} or Yb^{3+} species. In a situation when there is distribution of similar but only slightly different spectra/species, PARAFAC will fuse those distributions into a single species with an average emission spectrum or decay time. Additionally, when a two-dimensional analysis (for example with a delay-emission tensor) the algorithm gives an indication of the number of present species but the core consistency value is in this case not useful. Thus, a decision on the probable species that may be present can be informed by directly comparing raw data to PARAFAC results for the best decision to accept or reject the results. For the identification of Eu^{3+} or Yb^{3+} species in challenging samples where many sites contribute to the overall emission, the PARAFAC algorithm is exceptional.

2.12 Ceria in biological applications

Ceria, among other inorganic nanoparticles, has been reported to have enzyme-like activity, and is stable under harsh environments, inexpensive to produce and is not susceptible to denaturation as compared to protein enzymes[37,118]. The unique properties of nanoceria makes it a candidate for many bio-catalytic functions, ranging from peroxidase, catalase, superoxide dismutase (SOD) and glucose oxidase like activities[37,38,119,120]. These catalytic properties are a result of ceria's ability to reversibly cycle between its ionic states (Ce^{4+} and Ce^{3+}),[121] high stability and high oxygen storage capacity[52,54]. Korsvik et al. reported the molecular mechanism of the catalytic activity of ceria nanoparticles in biological systems[119]. They assessed the capability of mixed valence state ceria nanoparticles to react with superoxide in vitro and their results showed that ceria nanoparticles with higher Ce^{3+}/Ce^{4+} ratio were able to act like the cellular defense (superoxide dismutase), by displaying an antioxidant behaviour[119]. The Ce^{3+}/Ce^{4+} ratio can be altered, as it is dependent on the nanoparticle unique particulate characteristics such as nanoparticle size or specific reaction conditions used in synthesis[122,123].

The urgent need to obtain nano-therapeutic agents with the ability to treat specific diseases at the tissue and cell level resulted in the use of ceria in the fabrication of nanoparticles. Reactive oxygen species (ROS) or oxygenated free radicals such as superoxide, O^{2-} and peroxynitrite $ONOO^-$ are normal by-products of cellular metabolic reactions and are also reported to play a significant role in the pathogenesis of many diseases when they are present in abnormal amounts. In addition to their usual roles as secondary messengers in cell signaling and as immune activators, excess in ROS often results in adverse effects through damaging proteins and lipids[54]. Diseases resulting from the damage include sepsis, cancer, schizophrenia, depression, Alzheimer's, and Parkinson's[52,57]. Ceria has attracted special interest since it scavenges ROS[121,124]. The above-mentioned properties of ceria to mimic enzymes such as SOD, catalase or oxidase could be useful in biotechnology and therapeutics[120,125]. Ceria nanoparticles for biological applications have been synthesized alone[126-128], with Zr^{4+} ions[129], with Gd^{3+} ions[121], Eu^{3+} ions[52,57,130] and incorporated with gold[131]. Incorporating zirconia in ceria nanoparticle synthesis is believed to control the Ce^{3+} to Ce^{4+} ratio and the rate of conversion between the two oxidation states, producing a positive effect in catalysis. In addition to the +3/+4 ratio, other effects such as particle size, pH and buffer species can affect the specific enzyme-mimetic properties of ceria[121,132].

Although numerous publications on positive results of using ceria nanoparticles in biomedical applications have been celebrated, there are considerations to be made to modify the nanoparticles, so that many go past clinical trials and even to clinical practice. The effects of toxicity, nanoparticle instability and the formation of a protein layer on the nanoparticle surface after their administration in the body need to be considered as they can inflammation and induce immunotoxicity[133]. There is the growing realization that while the distinct obstacles that hinder adequate delivery of therapeutics to tumors are indeed complex, they are by no means avoidable[134].

2.13 Surface modification of ceria nanoparticles

To ensure the nanoparticles linger in the body for them to be efficient, do not form a bio-corona and are not nocuous, functionalization as a way of modifying the surface is done. Functional groups of modified nanomaterials can improve the dispersion and stability of nanoparticles in aqueous solutions. They are also a bonafide candidate to conjugate various biomolecules. Soh et al. functionalized their hydrophobic nanoparticles by using a polyethylene glycolation method (PEGylation)[129]. This method resulted in nanoparticles' high body circulation lifetimes following intravascular administration[133-137]. On the contrary, PEGylated nanoparticles have an increased hydrodynamic size and display a significantly reduced unspecific cellular uptake. Also, due to PEG's non-biodegradability, there have been reports of its accumulation as well as uncontrolled oxidative degradation into toxic products[138]. Therefore, the use of biodegradable polymers in the encapsulation is imperative. Recent research efforts are also aimed at functionalizing nanoparticles with zwitterionic materials as surface charge of nanoparticles has proven to be a major determinant of cellular internalization, which can cause degradation of

nanoparticles[139]. Also, there has been growing research in converting hydrophobic nanoparticles from thermal decomposition and from microemulsion methods of synthesis into water dispersible materials using inorganic material affinitive compounds such as dopamine, alendronate, and polyacrylic acid with a possibility of subsequent bioconjugation with different agents like peptides[12,36,38,140]. In this thesis, the possibilities of bio functionalizing ceria nanoparticles with DNA is explored.

2.14 Functionalizing ceria nanoparticles with DNA

DNA is an outstanding biopolymer providing a diversity of functionality due to well-defined sequences, programmable self-assembly and specific base-pairing rules. DNA nanotechnology could be developed because of the programmability of DNA, its inexpensive cost of synthesis[37], and ease of chemical modification[38]. In addition to redox reactivity, nanoceria surface is susceptible to modification by electrostatic interactions[39]. Through these electrostatic interactions, it has been reported to adsorb proteins. Highly negatively charged double-stranded (ds) DNA can interact with surfaces by electrostatic forces, whilst with single strand DNA (ssDNA), many intermolecular forces can take place including aromatic stacking, metal coordination, hydrogen bonding, hydrophobic force and electrostatic force[37,39]. Also, apart from sensing applications, using ssDNA to stabilize nanoceria particles is feasible, thereby enhancing its surface reactivity [39]. DNA has tunable length and sequence which also is an advantage, facilitating systematic studies[37,120]. It has been stated that DNA covering at the interface of inorganic nanomaterials inhibited the catalytic activities of nano enzymes due to steric hindrance[37].

Optimizing the length of the DNA would curb this effect. However, it has also been reported that attaching DNA to nanomaterials could accelerate the peroxidase-like activities of nanoceria because of high affinity with substrates[38]. Furthermore, there is increased research on functionalizing nanoceria with DNA, owing to its many advantages[37,141]. Binding ssDNA with nanoceria is not an arduous task as it is a single step process involving electrostatic interactions between the particles and the phosphate backbone[120]. As lanthanide-doped upconversion nanoparticles (UCNPs) have shown promise in biomedical applications, DNA has been used prepare uniform DNA-modified upconversion nanoparticles (DNA-UCNPs) as versatile bio probes, which are normally challenging to prepare as they are capped with hydrophobic ligands. The approach can directly convert the as-synthesized hydrophobic UCNPs into water-soluble DNA-UCNPs without any chemical modification of UCNPs or oligonucleotides[141]. Figure 2 shows the post synthetic strategies to modify the surface functionality of hydrophobic nanoparticles and their transfer into a hydrophilic phase.

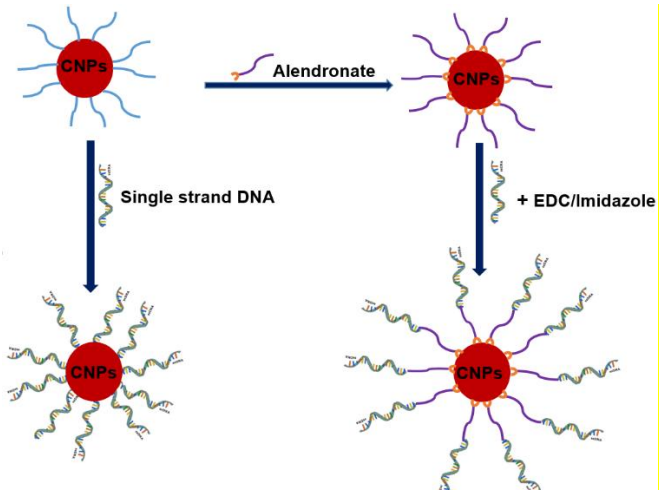

Figure 2. Overview of converting hydrophobic nanoparticles into aqueous media.

2.15 Hybridization of nanomaterials on DNA origami

It is also vital to understand the effect of spatial arrangement of ROS scavenger (ceria- based nanomaterials) and substrate (ROS) on nano-enzymatic activity to inform the decisions in their application to cellular environments. With DNA nanotechnology it is feasible to reliably organize nanoscale systems through the programmability of DNA hybridization and versatility of DNA-biomolecule conjugation strategies[142]. DNA origami, a technique for creating arbitrary shapes and patterns on an approximately 100 nm scale, has developed into an extremely valuable tool to arrange chemical entities such as nanoparticles, biomolecules, dyes and other molecules with nanometer precision[143,144,145-147]. In the meantime, DNA origami is used in very different fields such as chemical and biological sensing, drug delivery, molecular biology and materials science[144,148-150]. The development of DNA origami technique provides an addressable platform upon which to display ligands, permitting the precise patterning of multiple proteins, nanoparticles or other elements[142,151,152]. Consequently, DNA origami is well suited to study distance-dependent reactivities of a ROS source and sink (scavenger)[153]. Hybridization of metal nanoparticles on DNA origami nanostructures have been reported[145]. Atomic force microscopy (AFM) has been used as a read-out where biological process applications have been mimicked[154-157]. Figure 3 shows the envisioned hybridization of the hydrophilic nanoparticles onto the origami triangle.

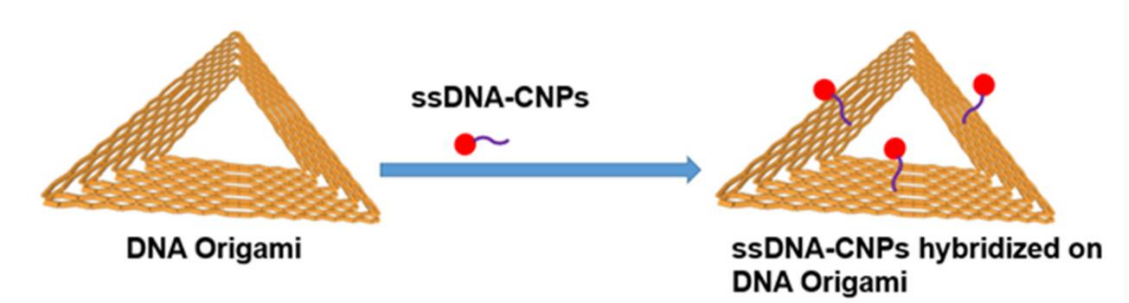

Figure 3. Overview of hybridization of nanomaterials onto DNA origami. Note the nanoparticles will site at the position determined by the patterning and availability of overhangs onto the origami.

As already been highlighted, ceria-based nanomaterials, doped with different lanthanides possess very interesting properties. These properties can be fully exploited for applications in catalysis, to solve emerging problems on the planet and in biological applications. When they are synthesized strategically, undergo the right surface modification routes, with the right post thermal treatments and taken in the right proportions, they can become a viable and feasible theranostic.

Chapter 3: Experimental and characterization methods

3.1 Chemicals and Materials

3.1.1 Nanoparticle Synthesis

All chemicals used to synthesize the ceria nanomaterials were of highest grade available and were used without further purification. Chemical name, supplier and purity are listed in Table 1. Distilled water (resistance 18.2 MΩ·cm (298 K)) obtained from Milli-Q® Advantage A10 Water Purification System (Merck, Germany) was used.

Table 2. Chemical name, supplier and purity.

Chemical name	Supplier	Purity
Cerium (III) nitrate hexahydrate	Alfa Aesar	≥99.5%
Gadolinium (III) nitrate hexahydrate	Sigma Aldrich	≥99.9%
Europium (III) nitrate hexahydrate	Strem Chemicals, Sigma Aldrich	≥99.9%
2-ethylhexanoic acid (EHA)	Sigma Aldrich	≥99%
Precursor solution based on ethanol	Th. Geyer	>99.9 %
Zirconium (IV)nitrate hydrate	Sigma Aldrich	99.99 %
Ytterbium (III) nitrate pentahydrate	Sigma Aldrich	99.9 %
Oleylamine	Sigma Aldrich	70 %
1-octadecene	Sigma Aldrich	90 %
Toluene	Sigma Aldrich	99.9 %,
Dioctyl sulfosuccinate sodium salt (AOT)	Sigma Aldrich	≥97%
Hydrogen peroxide (30 %)	Sigma Aldrich	97 %
TAE buffer	Sigma Aldrich	
$MgCl_2$	Sigma Aldrich	≥99 %

3.1.2 DNA sequences used in the study

ssDNA coating strands used for Eu^{3+}- doped CeO_2 surface functionalization are listed in Table 3 and the modified ssDNA staple sequences used in the origami design in Table 4.

Table 3. ssDNA coating strands used for Eu^{3+}- doped CeO_2 surface functionalization. All the DNA were obtained from Metabion, Germany and used without further purification.

DNA Code	Sequence
(TTT)8 GG NP	TTTTTTTTTTTTTTTTTTTTTTT GG
(TTT)12GG NP	TTTTTTTTTTTTTTTTTTTTTTTTTTTTTTTTTTGG
(CCC)12GG NP	CCCCCCCCCCCCCCCCCCCCCCCCCCCCCCCCCCGG
(AAA)12GG NP	AAAAAAAAAAAAAAAAAAAAAAAAAAAAAAAAAAGG

Table 4. Modified ssDNA staple sequences used in the origami design. These situate around the middle positions of the triangles. All the DNA were supplied by Metabion, Germany.

DNA	Modified DNA origami Sequence
t-1s6e	AAA AAA AAA AAA AAA AAA AAA AAA TTT TTA GTA TCG CCA ACG CTC AAC AGT CGG CTG TC
t-1s16e	AAA AAA AAA AAA AAA AAA AAA AAA TTT ATT CGG TCT GCG GGA TCG TCA CCC GAA ATC CG
t-1s26e	AAA AAA AAA AAA AAA AAA AAA AAA TTT GCC AGT GCG ATC CCC GGG TAC CGA GTT TTT CT

3.2 Ceria nanomaterial synthesis

3.2.1 Ceria and gadolinium mixed oxides (GDC) synthesis

The GDC powders were synthesized by spray flame pyrolysis in a reactor, which is equipped with a SpraySyn burner. This burner is developed for fundamental understanding of particle formation in spray flames[158], but also suitable for production of nano-powders in a scale of 10 g/h. The liquid precursor solution (Nitrates in EtOH/Water) is delivered by a syringe pump to a capillary in the center of the burner, where it is atomized by O_2 in a two-fluid nozzle. For ignition and stabilization of the flame, the spray is injected into a surrounding premixed CH_4/O_2 pilot flame. The synthesis is performed at a pressure of 1000 mbar in the reaction chamber. The salts are dissolved in ethanol by stirring. To avoid precipitation, the particle synthesis is started immediately after preparation of the precursor solution. Once the solution is clear, demineralized water and 2-ethylhexanoic acid is added dropwise into the continuously stirred solution. These are added to stabilize the solution and suppress the formation of particles in the size regime above 20 nm[159]. Table 5 shows the different compositions of the precursor solutions. In each synthesis the concentration of Eu, EHA and water was kept constant and the ratio of Ce/Gd was varied from 60/40 to 100/0. The Eu^{3+} ion concentration was set to be about 1% of the total metal content. Different nanoparticle samples synthesized required different composition of precursor solution. These are shown in Table 5.

Table 5. Composition of precursor solution for three different GDC synthesis.

Sample number	Ce [mol/l]	Gd [mol/l]	Eu [mol/l]	EHA [vol%]	H_2O [vol%]
1	0.06	0.04			
2	0.08	0.02	0.001	30	5
3	0.09	0.01			

3.2.2 $Ce_xZr_{1-x}O_2:Eu^{3+}$|YSZ nanocomposite (NC) synthesis

Synthesis of NC was conducted using a modified version of the incipient wetness impregnation method described by Arias-Duque et al., using multiple precursor nitrates[50]. The YSZ support, containing 8 mol % of Y, was generously provided by Kefarol GmbH. Cerium (III) nitrate, zirconium (IV)nitrate hydrate, and europium (III)nitrate hydrate were used. The incipient wetness impregnation of YSZ to produce 15% $Ce_{0.5}Zr_{0.5}O_{2-y}$: Eu^{3+}|YSZ , 15% CeO_{2-y}:Eu^{3+}|YSZ, and 15% Zr_{O2-y}: Eu^{3+}|YSZ nanocomposites was achieved by repeatedly applying a few drops of the Ce^{3+}/Eu^{3+} and/or Zr^{4+} mixture (1.2M) onto 1g of YSZ powder to yield a wet powder but not a slurry, followed by drying in a 383K heated oven (Thermo Scientific Heraeus) until the required amount of precursor solution was consumed. After impregnation, the samples were dried overnight in the 383K heated oven. Subsequently, annealing in air at 773K and 1237K was performed for 2 hours on separate as-synthesized samples in an oven MLM VEB Electro Bad Frankenhausen (type LM 212.11). These samples will be denoted as in the Table 6.

Table 6. NC sample name and how they will be denoted in the thesis

NC sample name	Name used in thesis
15% $Ce_{0.5}Zr_{0.5}O_{2-y}$: Eu^{3+}|YSZ	NC-Ce50
15% CeO_{2-y}: Eu^{3+}|YSZ	NC-Ce100
15% Zr_{O2-y}: Eu^{3+}|YSZ	NC-Zr100

Figure 4 shows the overview of the synthesis of ceria-based YSZ supported nanomaterials by an incipient wetness impregnation method and post synthesis thermal treatment at 773 K for 2 h.

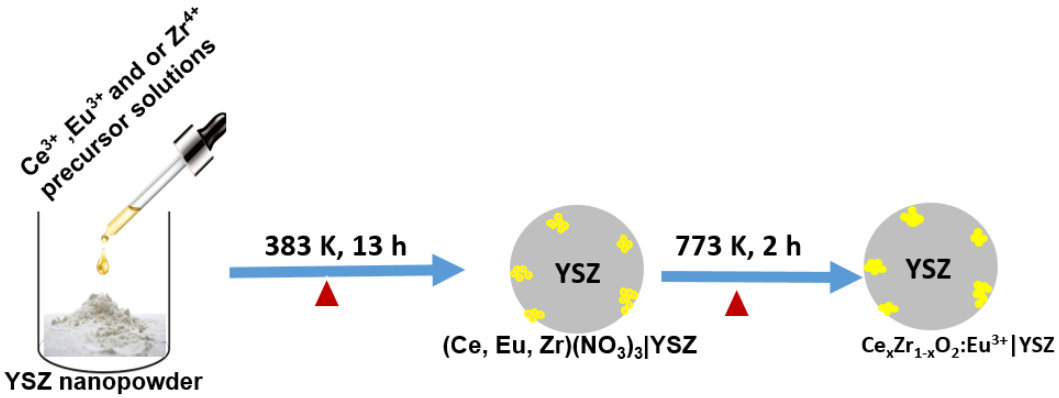

Figure 4. Scheme showing the overview of the synthesis of ceria-based YSZ supported nanomaterials by an incipient wetness impregnation method and post synthesis thermal treatment at 773 K for 2 h. The precursor nitrates are successively applied on the support and dried. Heating the impregnated powder at a higher temperature produces the nanoparticles on the support surface. Figure adapted from Yeste et al[34].

3.2.3 $Ce_{1-x}Yb_xO_2$ nanomaterial synthesis

Thermal decomposition method was used to synthesize ceria nanoparticles doped or mixed with ytterbium**.** ytterbium (III) nitrate pentahydrate (0.03 mmol; 0.0135 g), cerium (III) nitrate hexahydrate (0.97 mmol; 0.4212 g) were dissolved in oleylamine (0.990 mL; ~0.805 g) and 1-octadecene (5 mL; 4 g). The mix proportions of ytterbium and cerium were varied according to the desired final product. The mixture was stirred (600 rpm and at 353 K) for 30 min under vacuum using Heidolph MR Hei-Standard hot plate. Thereafter, it was heated to 533 K to react for 2 h. After cooling to room temperature, 80 mL acetone was added to the solution and the nanoparticles were collected by centrifugation (30 min; 4500 rpm) using an Eppendorf centrifuge (model 5804). The nanoparticles were redispersed in hexane (max. 3 mL). The nanoparticles were washed three more times in the same way and finally dispersed in 10 mL hexane and stored in the fridge for further analyses. To obtain a powder, the volumes of the nanoparticle solvent were reduced in a Heidolph rotary evaporator equipped to a Heidolph vacuum pump, before being dried in an oven at dried at 353 K in an oven for an hour. The powders obtained were calcined in air at 773 K and 1273 K for 2 h after that (in an oven MLM VEB Electro Bad Frankenhausen).

3.2.4 Synthesis of Eu^{3+} doped ceria nanoparticles

The nanoparticle synthesis was accomplished by a micro-emulsion method described by Yang et al[140]. Toluene, dioctyl sulfosuccinate sodium salt (AOT), cerium (III) nitrate hexahydrate and europium nitrate pentahydrate and hydrogen peroxide (30 %) were used in the synthesis of 1 mol % doped cerium oxide nanoparticles. AOT (1.5 g and in other syntheses, different amount of surfactant was used) was dissolved in 50 mL of toluene at room temperature, stirring at 600 rpm. After the surfactant was fully dissolved, cerium and europium nitrate precursor solution (2.5 mL, 0.1 mol/L) was added dropwise and the microemulsion formed was stirred for 45 min followed by adding 5 mL of 30 % H_2O_2. Thereafter, the solution was stirred. Stirring was stopped after an hour and the mixture was allowed to separate into two layers. The organic layer containing the nanoparticles were collected for characterization and surface modification.

3.3 Surface modification using single strand DNA (ssDNA)

Initially, Poly Adenine $(AAA)_{12}$, poly Thymine $(TTT)_{12}$ and poly Cytosine $(CCC)_{12}$) coating strands (shown in Table 3), were screened for ssDNA adsorption on commercial nanoparticles obtained from Sigma Aldrich. 1 ml of 58 µM ceria nanoparticles were mixed with 4 µL of 100 nM DNA and stirred overnight at room temperature and at 300 rpm using a Peqlab Thriller shaker. The resultant coated nanoparticles were washed three times using a microcentrifuge and dispersed in 1 mL of milli Q water and characterized using DLS Malvern Zetasizer Nano instrument and Witec Alpha 300 TEM instrument.

The Eu^{3+} doped ceria nanoparticles dispersed in toluene were functionalized in a single step using the poly Thymine DNA ($(TTT)_8$ and $(TTT)_{12}$) sequences shown in Table 3. The method used was adapted from the method by Li et al[141]. Typically, the AOT capped Eu^{3+}-doped ceria nanoparticles diluted with toluene up to 100 µL (about 10 µM) was slowly added into a 200 µL water solution containing 200 nmol ssDNA, and the solution was vigorously stirred overnight. Afterward, the nanoparticles could be transferred into the bottom water phase from the toluene phase due to the ssDNA attachment. The aquatic solution was transferred to a microtube. Excess ssDNA was recovered from DNA conjugated NPs by centrifugation (using a Thermo scientific Heraus Fresco 17 centrifuge) and washing in a 100 KDa filter centrifuge tube.

3.4 Triangular DNA origami Synthesis

Table 4 shows the modified staple sequences used in the triangular DNA Origami design. The triangular DNA origami nanostructures were folded using M13mp18 (5 µL; 100nM) viral strand with 208 short oligonucleotides (30 µL) in 10× TAE buffer containing 150 mM $MgCl_2$ and Milli-Q water in a total volume of 100 µL. The solution was subjected to annealing at 353 K and gradually cooled down to 281 K in 2 h using a thermal cycler (PEQLAB, VWR). The annealed solution was purified by centrifugal filtration using 100 KDa MWCO centrifugal filters (Merck Millipore) by following three step washing cycles with 1× TAE with 15 mM $MgCl_2$. The final filtered solution was collected in an Eppendorf tube and final concentration of the DNA origami was calculated following UV-vis absorption measurement using NanoDrop 2000 (Thermo Scientific). Figure 5 shows the overview of the fabrication of the origami triangle.

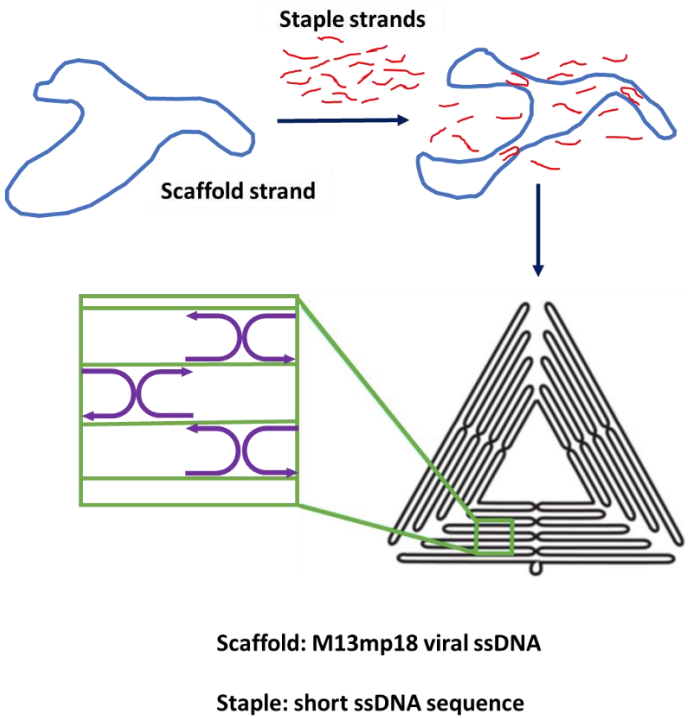

Figure 5. Scheme showing how DNA origami is fabricated. Figure adapted from Bald and Keller[160].

3.5 DNA Origami - Nanoparticle Hybridization

The folded DNA origami solution (13.7 nM) was mixed with fully ssDNA coated ceria nanoparticles (circa 80 nM) in a ratio of 1:3 in 1× Tris acetate EDTA (TAE), 15 mM $MgCl_2$ solution, heated up to 318 K and cooled down to 298 K over 1 h 40 min using the thermal cycler. The hybridized DNA origami-nanoparticle dispersion was then purified in three step washing cycles with 1× TAE with 15 mM $MgCl_2$. The final filtered solution was collected in an Eppendorf tube and immobilized on a plasma cleaned silicon substrate (using an instrument Electronic diener) and then imaged using Nanosurf atomic force microscopy (AFM) C3000 instrument operated in non-contact mode with a set point of 65 %.

3.6 Characterization techniques

3.6.1 GDC nanomaterials

X-ray Powder diffraction data were collected on a PANalytical Empyrean powder X-ray diffractometer in a Bragg–Brentano geometry. It is equipped with a PIXcel1D detector using Cu Kα radiation (λ = 1.54187 Å) operating at 40 kV and 40 mA. θ / θ scans were run in a 2θ range of 4-70° with step size of 0.0131° and a sample rotation time of 1s. The diffractometer is equipped with a programmable divergence and anti-scatter slit, and a large Ni-beta filter. The detector was set to continuous mode with an active length of 3.0061°. The sizes of the crystallites were calculated using the Scherrer-equation:

$$D = \frac{K\lambda}{\beta Cos\theta} \qquad [16]$$

where D is the crystallite size, K = 0.9; the Scherer constant, λ = 0.15418 nm, β is the FWHM in radians and θ is the peak position in radians.

Raman spectra were recorded to examine the lattice vibrations in the nanoparticles at room temperature with an excitation source of 633 nm laser using a Raman microscope (model Witec Alpha 300) with a grating of 2400 l/mm.

Fluorescence line narrowing spectroscopy measurements were accomplished by cooling dry samples contained in NMR tubes placed inside a copper sample holder and set in a vacuum chamber attached to the cold plate of a closed cycle liquid helium cryostat. The cryostat is composed of a helium compressor unit (CKW-21, Sumitomo Heavy Industries Ltd.), a vacuum pump for the sample chamber (Turbolab 80, Oerlikon Leybold Vacuum), and a temperature controller (331, Lakeshore). A pulsed Nd:YAG laser (Quanta Ray, Spectra Physics, USA) with a set repetition rate of 10 Hz was coupled to an optical parametric oscillator (OPO, GWU Lasertechnik, Germany), serving as a light source for the Eu^{3+} excitation at λ_{ex} = 575-583 nm ($^5D_0$–$^7F_0$ transition). The excitation light was coupled into one of the branches of a Y-shaped fiber bundle, whereas the other branch was connected to a spectrograph (Shamrock SR-303i, Andor Technology) equipped with an intensified charge-coupled device (iCCD) camera (iStar DH 720, Andor Technology). The combined excitation and emission bundles were mounted in front of a lens system that allows excitation of the sample and acquisition of the emission light at the same time. Four samples can be measured separately by moving the lens system on a translational stage between the samples.

Room temperature time resolved emission spectra (TRES) were recorded using a wavelength tunable Nd:YAG-laser /OPO system (Quanta Ray, Spectra Physics/Scan master, GWU) operated at 20 Hz as excitation light source and an intensified CCD camera (i-Star DH 720, Andor Technology) coupled to a spectrograph (MS257 Model 77700A, Oriel Instruments) equipped with a 300 l/mm grating as detection system. The initial gate delay, Δt was set to 500 ns and the gate width was set at 500 μs. The emission spectra for the $^5D_0$-^7F_J (J= 0-6) transition of the samples were recorded at room temperature at wavelength of excitation, λ_{ex} = 464nm. The photoluminescence decays were analyzed by fitting with a multi-exponential function f(t), using Origin 2019b software:

$$f(t) = \sum A_i exp\left(-\frac{t}{\tau_i}\right) + B \qquad [17]$$

where A_i is the decay amplitude, B is a constant and t_i is the time constant of the decay, i.

3.6.2 $Ce_xZr_{1-x}O_2$:Eu^{3+}|YSZ nanocomposites

The powders were characterized by high-resolution spectroscopy under ultra-low temperature conditions, Raman spectroscopy, XRD, scanning transmission electron microscope-X-ray energy-dispersive spectroscopy (STEM-EDX) and TPR. The ultra-low temperature high resolution spectroscopy, X-ray diffraction and Raman spectroscopy measurements were accomplished in the same way and using the same instruments as for the GDC nanomaterials. Samples for microscopy measurements were prepared by sonicating nanocomposite solid samples dispersed in hexane. The suspension was dropped directly onto holey-carbon-coated copper grids. STEM studies, in both High-angle annular dark-field imaging (HAADF) and analytical EDX modes, were performed on a double AC FEI Titan3 Themis 60–300 microscope operating at 200 kV. A condenser aperture of 50 μm and a 115 mm camera length were used, obtaining an electron probe with a convergence angle of 21.4 mrad. To obtain a high signal-to-noise ratio, a beam current of 120 pA was used. The XEDS hypermaps were recorded using the high-efficiency SuperX G2 detection system equipped in a microscope that integrates four windowless detectors surrounding the sample and high-performance signal-processing hardware.

The surface and or bulk lattice oxygen reduction behaviours of the synthesized nanocomposites were determined using H_2-TPR. Typically, 50 mg of sample was placed in a curved quartz reactor filled with heated glass wool to immobilize the sample and prevent small nanoparticles from being dragged along by the gas flow. The reactor was coupled to the gas mixing unit on one end and to a mass spectrometer (Pfeiffer Omni ^{Star} GSD 320 mass spectrometer) on the other. The lower part of the reactor containing the sample was fixed and positioned inside a cylindrical furnace where a temperature sensor was attached to the reactor wall. Initially, samples were cleaned by heating them to 303K for 30 minutes, then to 773 K under 5 % O_2/He flowing at 80 ml/min via a gas analysis system Omni ^{Star}, at a heating rate of approximately 10 K/min; they were then kept for 30 minutes at this temperature and further cooled to 353 K under He with a flow rate of 60 ml/min. After cleaning the nanocomposite samples, the reduction procedure was done by heating under flowing H_2 (5%)/Ar (60 ml/min) from room temperature up to 1173 K, at a heating rate of 10 K/min and followed by $3\frac{1}{2}$ h of isothermal treatment at 1173 K. After this, the gas flow was switched to He (60 ml/min), for 1 h, and the sample was cooled to 298 K under this inert gas at a flow rate of (60 ml/min). The TPR signal was plotted in the form of water (mass/charge ratio = 18) produced during the reduction process against temperature was detected using a mass spectrometer detector.

3.6.3 Yb-doped ceria nanoparticle characterization

The powders were characterized by XRD, TEM, Raman spectroscopy and high-resolution spectroscopy at room temperature and ultra-low temperature conditions. X-ray diffraction and Raman spectroscopy

measurements were accomplished in the same way and using the same instruments and procedure as in the analysis of GDC nanoparticles. The difference with the Raman measurements was the instrument used here was the Horiba LabRam HR Evolution.

SEM and EDXS experiments were done on a JEOL JSM-6510 with a W-filament operated at 15 kV and equipped with an Oxford Instruments INCAx-act detector. Small amounts of the samples were deposited on a carbon glue pad. Prior to analysis, all samples were coated with 25 nm of carbon by vaporizing a thin carbon wire under extremely high temperatures in a vacuum chamber using a Polaron CC7650 Carbon Coater. The Back Scattered Electron (BSE) detector was used for material contrast, the Secondary Electron (SEE) detector for topographic images at 15 kV. TEM measurements were done using a JEOL microscope (model JEM 1011). The room temperature and ultra-low temperature high resolution spectroscopy were done using the same instrumentation as with Eu^{3+} -doped GDC. The only difference was that the dopant Yb was excited in the NIR region at 915 nm. The initial delay and gate width were pegged at 5 µs and 100 µs respectively using a slit width of 10 µm.

3.7 Parallel Factor analysis (PARAFAC)

The PARAFAC algorithm is deconvoluting time delay and excitation dependent emission data into several species, based on the assumption that the total measured emission spectrum is the superposition of the weighted single species spectra[116,117]. This way it is possible to deconvolute the data into the pure decay functions, excitation spectra and emission spectra (depending on the data set) of each pure europium and ytterbium species. In the case of lanthanide emission experiments the word species describes groups of ions located in identical lattice sites, yielding the same spectrum. In case of a distribution of similar but only slightly different spectra/species, PARAFAC will combine those distributions into a single species with an average emission spectrum or decay time. Additionally, when doing a three-dimensional analysis (for example a delay-excitation-emission tensor) the algorithm gives an indication of the number of present species by way of the core consistency value.

As TLS for the GDC samples were measured at 4 K at different initial delays, PARAFAC was used for a sample-by-sample deconvolution of the excitation-emission-delay tensor to find the single excitation spectrum, emission spectrum, and decay time for each present species. As only three different delays were used in the experiment, the error of the decay times is rather large (three data points for a two-parameter exponential).

For the time-resolved emission spectra of the GDC samples (measured at room temperature), a sample-by-sample deconvolution of the emission-delay matrix was used to find the single emission spectra and decay constants of each present species. However, for the ceria Yb^{3+} mixed oxides (measured at room temperature and 4 K) and for Eu^{3+} doped ceria (AOT and ssDNA capped), all the samples were deconvoluted in one global function. No reasonable core consistencies were calculated in these the cases

as the TRES results are two-dimensional. In the analyses, PARAFAC was executed in MATLAB 2019b (The MathWorks, Inc.). Deconvolution by a monoexponential constraint in the time dimension was conducted by the procedure described by Drobot, et al. [161].

Chapter 4: Structural analysis of Eu^{3+} and Gd^{3+} co doped ceria mixed oxides

Chapter 4 forms part of the following publication:

Chemura, S., Haubitz, T., Primus, P. A., Underberg, M., Hülser, T., & Kumke, M. U. (2020). Europium-Doped Ceria–Gadolinium Mixed Oxides: PARAFAC Analysis and High-Resolution Emission Spectroscopy under Cryogenic Conditions for Structural Analysis. *The Journal of Physical Chemistry A*, *124*(24), 4972-4983.

4.1 Introduction

Ceria-based oxides have attracted special attention in numerous technological applications. Solid oxide fuel cells (SOFC)[43,44,67,162] are great prospects to produce and store green energy in the face of climate change. The ionic conductivity of the commonly used electrolyte in SOFC, yttrium-stabilized zirconia (YSZ) reaches an optimum at temperatures above 1073 K[41]. Electrolyte materials with higher ionic conductivities that could lower the SOFC operating temperature to intermediate temperatures (673−973 K) are being considered, e.g., gadolinium-doped ceria (GDC) for significant increase in the applicability and effectiveness of solid oxide fuel cells. [42,41,43-46]. The applications in SOFC rely on oxygen vacancy migration in ceria. Pure ceria contains a fraction of Ce^{3+} ions, resulting in oxygen vacancies in the oxygen sub-lattice to balance the effective negative charge (intrinsic vacancies).

Dopant concentration and the size of the dopant ions plays an important role, that is when the dopant ion radius is close to the radius of the ceria host, then the doped ceria displays high oxygen ion conductivity with the same molar fraction of dopants[33]. When ceria is doped with lanthanide ions, the site preference of oxygen vacancies as NN or NNN to the dopant ion is determined by the strength and nature of their interaction, both of which rely on dopant ion size[59,60,163].

Doping is often used to modify the properties of ceria for different applications, such as the introduction of luminescence properties. At the same time Eu^{3+} ions are powerful structural probes, as they can provide information on the crystal field symmetry and strength determined by their local environment, and they allow to monitor even small changes in that environment, based on Judd-Ofelt theory [63,64].

$Ce_{1-x}Gd_xO_{2-y}$: Eu^{3+} ($0 \leq x \leq 0.4$) nanoparticles were synthesized using flame spray pyrolysis[46]. Eu^{3+} and Gd^{3+} co-doped ceria nanoparticles were structurally elucidated based on high resolution emission spectroscopy carried out under cryogenic conditions with special emphasis on using the intrinsic selectivity of the $^5D_0 - ^7F_0$ transition. The potential PARAFAC analysis to gain similar structural insight from more common, low-resolution, room temperature emission data was exploited.

4.2 Results and discussion

4.2.1 Characterization of the GDC nanoparticles by conventional techniques

The morphology of the powders was analyzed by transmission electron microscopy (TEM). TEM micrographs for CeO_{2-y}: Eu^{3+} and $Ce_{0.6}Gd_{0.4}O_{2-y}$: Eu^{3+} are shown in Figure 6 (top). As can be seen, the particles are nano-sized (particle sizes around 10 nm) and of roughly cubic shape. The results are comparable to the obtained crystallite sizes from XRD (*vide infra*). The XRD patterns of $Ce_{1-x}Gd_xO_{2-y}$: Eu^{3+} nanocrystals are shown in Figure 6. The diffraction patterns indicate a single phase, which matches with standard cubic fluorite structure (space group $Fm\bar{3}m$). We found good agreement with reference data (see the JCPDS file numbers shown in the Table 7).

In order to evaluate the effect of the Gd^{3+} concentration on the sample properties, the crystallite size was determined based on the Scherrer equation (see equation 16). It was found that the crystallite size slightly decreased inversely with the Gd^{3+} concentration in the samples. As shown in Figure 6 (middle, right) and Table 7, a reasonable correlation was found. The decrease in crystallite size could partly be a consequence of slightly changed reaction condition in the flame due to the presence of Gd^{3+}.

Moreover, there is a minor shift to lower 2θ values of the peak from 28.3º for CeO_{2-y}: Eu^{3+} with the increase in Gd^{3+} concentration, exemplified by inset 1 in Figure 6 (middle, left). This indicates homogeneous mixing of the Gd^{3+} ions into the fluorite structure, causing lattice expansion with increasing concentration of the slightly larger Gd^{3+}. The results are confirmed by Acharya, et al. [55] and Sorbello, et al. [60,164] and they are in good agreement with effective ionic radii considerations (Gd^{3+} ion has a larger ionic radius of 0.105 nm compared to the radius of Ce^{4+} ion of 0.097 nm), where there is substitution of the smaller Ce^{4+} ions by the larger Gd^{3+} ions. Similar trend was reported due to incorporation of Sm^{3+} (0.1079 nm ionic radius), Pr^{3+} (ionic radius 0.1126 nm) and incorporating high concentrations of Eu^{3+} into the ceria[57]. It has also been found out that doping smaller trivalent ions e.g. Yb^{3+} (ionic radius 0.0985 nm) results in ceria lattice contraction, although the extent of the lattice parameter changes with the concentration of the trivalent dopant ion. Babu et al. confirmed this also the results from our recent findings with Yb^{3+}-doped ceria also supports this assertion (see Chapter 6) [80].

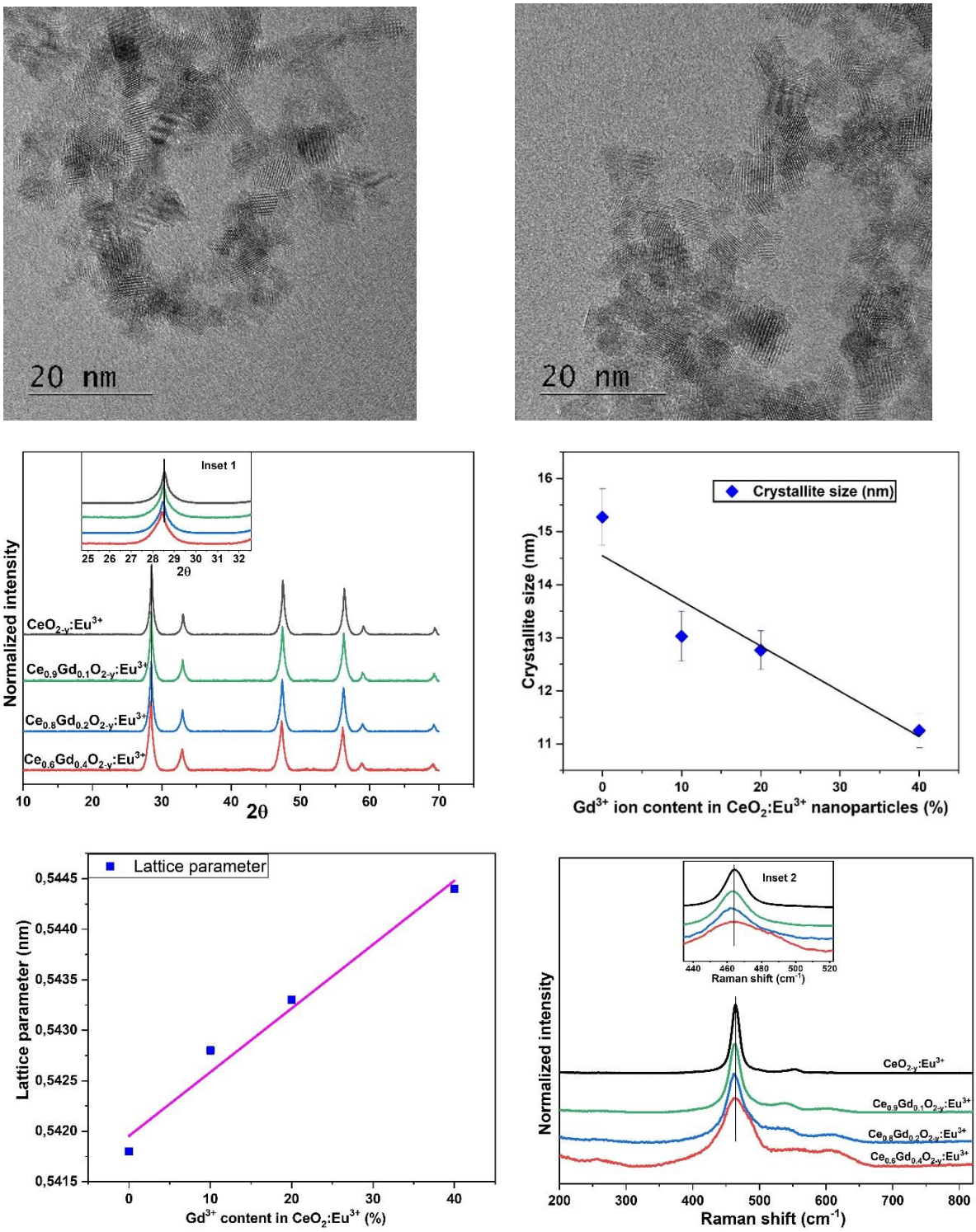

Figure 6. TEM micrographs of CeO_{2-y}: Eu^{3+} (top left) and $Ce_{0.6}Gd_{0.4}O_{2-y}$: Eu^{3+} (top right), X-ray powder diffraction patterns of CeO_{2-y}: Eu^{3+} and $Ce_{1-x}Gd_xO_{2-y}$: Eu^{3+} nanocrystals; Cu-K_α radiation (λ= 1.54187 Å) (left, middle). Crystallite size versus Gd^{3+} ion content in CeO_{2-y}: Eu^{3+} and $Ce_{1-x}Gd_xO_{2-y}$: Eu^{3+} nanoparticles (right, middle). Lattice parameter versus Gd^{3+} concentration in $Ce_{1-x}Gd_xO_{2-y}$: Eu^{3+} nanocrystals (left, bottom). Finally, Raman spectra for CeO_{2-y}: Eu^{3+} and $Ce_{1-x}Gd_xO_{2-y}$: Eu^{3+} (λ_{Laser} = 633 nm) (right bottom).

The lattice expansion is reflected by the calculated lattice parameters shown in Table 6.

The lattice parameter, a, was calculated using the formula:

$$d = \frac{\lambda}{2Sin\theta} \quad [18]$$

$$a = d\sqrt{h^2 + k^2 + l^2} \quad [19]$$

where a, is the lattice parameter, d is the inter-planar spacing and θ is the diffraction angle of the peak with the highest intensity.

Furthermore, the absence of characteristic reflections matching the Gd_2O_3 or Eu_2O_3 phases suggests random mixing of Ce^{3+}, Eu^{3+}, and Gd^{3+} cations, indicating the formation of a solid solution of $Ce_{1-x}\ Gd_xO_{2-y}$: Eu^{3+}. However, it has to be kept in mind, that phases with a content below 5 % and also small crystallites (below 5 nm) are generally hardly detectable by XRD.

Table 7. Crystallite sizes of the $Ce_{1-x}Gd_xO_{2-y}$: Eu^{3+} nanocrystals as calculated by the Scherrer equation, lattice parameters and JCPDs file numbers.

Sample	Crystallite size(nm)	Lattice parameter(nm)	Peak position(º)	FWHM	JCPDS File No
CeO_{2-y}:Eu^{3+}	15.3±0.53	0.5418±3.2E-5	28.54	0.64±0.004	98-005-3995
$Ce_{0.9}Gd_{0.1}O_{2-y}$: Eu^{3+}	13.0±0.47	0.5428±3.9E-5	28.48	0.76±0.005	98-015-5605
$Ce_{0.8}Gd_{0.2}O_{2-y}$: Eu^{3+}	12.8±0.37	0.5433±3.1E-5	28.46	0.73±0.004	98-007-2155
$Ce_{0.6}Gd_{0.4}O_{2-y}$: Eu^{3+}	11.2±0.32	0.5444±3.2E-5	28.40	0.85±0.004	98-015-5607

In addition to the frequently reported TEM and XRD data, Raman data was also collected. The Raman spectra of the CeO_{2-y}: Eu^{3+} and $Ce_{1-x}Gd_xO_{2-y}$: Eu^{3+} samples are shown in Figure 6 (right, bottom). Raman spectra of Gd^{3+} containing samples showed vibrational modes around 461, 550, and 605 cm^{-1}, respectively, while the Raman spectrum of CeO_{2-y}: Eu^{3+} exhibits only two modes, around 464 and 554.5 cm^{-1}. A very weak Raman mode at 253 cm^{-1} can be seen for the sample with highest Gd^{3+} content. This can be assigned to the doubly degenerated 2TA mode. The absence of characteristic band for Gd_2O_3, at 360 cm^{-1} evidently corroborates the incorporation of Gd^{3+} ions into CeO_2 lattice (solid solution), confirming the absence of any impurity phase in the lattice, which agrees with XRD results.

The mode around 464 cm^{-1} corresponds to the Raman active F_2g mode of the CeO_2 fluorite structure and originates from the symmetrical breathing mode of oxygen ions around the Ce^{4+} ions, which is sensitive to disorder in the oxygen sub-lattice as a result of non-stoichiometry[33,165]. This mode is slightly shifted to lower wavenumbers as Gd^{3+} ions are added into the ceria lattice. The weak signals around 550 cm^{-1} and 605 cm^{-1} increased with increasing Gd^{3+} concentration (see Figure 6, bottom left). These changes in the Raman spectra when ceria is incorporated with Gd^{3+} ions are a consequence of inhomogeneous strain and defects caused by substitution at the smaller radii Ce^{4+} (0.097 nm) site by larger Gd^{3+} (ionic radii 0.105 nm) ions[33,166] as well as by charge compensation (Ce^{4+}/ Gd^{3+}).

4.2.2 Eu^{3+} luminescence-based characterization

Eu^{3+} dopants in ceria can be electronically excited via direct or indirect excitation routes. In the former case, there is excitation of one of the many f−f absorption bands Eu^{3+} exhibits in the UV-Vis spectral range, for example the $^5D_2$–$^7F_0$ transition around 464 nm (this transition was used in the room temperature measurements) and $^5D_0$–$^7F_0$ transition around 580 nm, which is used for site-selective excitation with a narrow-bandwidth laser source (this transition was used in the ultra-low temperature measurements). Indirect excitation of Eu^{3+}-doped ceria via the Ce^{4+}–O^{2-} charge transfer (CT) band ($\lambda_{excitation}$ = 280−375 nm) results in a sensitization of Eu^{3+} dopants by ceria.

4.2.2.1 Time-resolved luminescence measurements at room temperature (non-site-selective excitation at $\lambda_{excitation}$ = 464 nm)

The time-resolved emission spectra were recorded ($\lambda_{excitation}$ = 464 nm,) at room temperature (RT) for the complete emission range of Eu^{3+} covering the full transitions of $^5D_0$-$^7F_0$ to $^5D_0$-$^7F_6$. In Figure 7 (left) the emission spectra collected with a delay time Δt = 100 μs after the laser pulse are shown. It was found that upon Gd^{3+} doping, the emission spectra significantly differ from that of pure ceria. The major difference is the very sharp distinct emission peak at $\lambda_{emission}$ = 591 nm. In Figure 7 (right), the time-resolved emission spectra of the CeO_{2-y}: Eu^{3+} sample are shown. Here, it can be seen that the relative contribution of the other emission bands to the sharp peak is changing with increasing delay time, indicating that this signal was originating from a Eu^{3+} species unique for the ceria sample. This emission was only observed under non-site-selective excitation conditions. We attribute this emission to Eu^{3+} ion in a high-symmetry environment. Since for the ceria, the lattice was of the cubic fluorite type, an O_h point group at the Eu^{3+} location could explain this sharp single emission peak found for the $^5D_0$-$^7F_1$ transition (the other emission bands seem to be of very low, if any, intensity (see Figure 7, right). This interpretation is further supported by the fact that no such peak was observed in the emission spectra recorded under site-selective excitation conditions in the spectral range of the $^5D_0$-$^7F_0$ transition, because for the high symmetry site, this transition is strictly forbidden and consequently excitation is very improbable (*vide infra*). In contrast to the pure ceria sample, all Gd^{3+}-doped samples showed rather

similar emission spectra with respect to the spectral intensity distribution of the different luminescence peaks (see Figure 7, left).

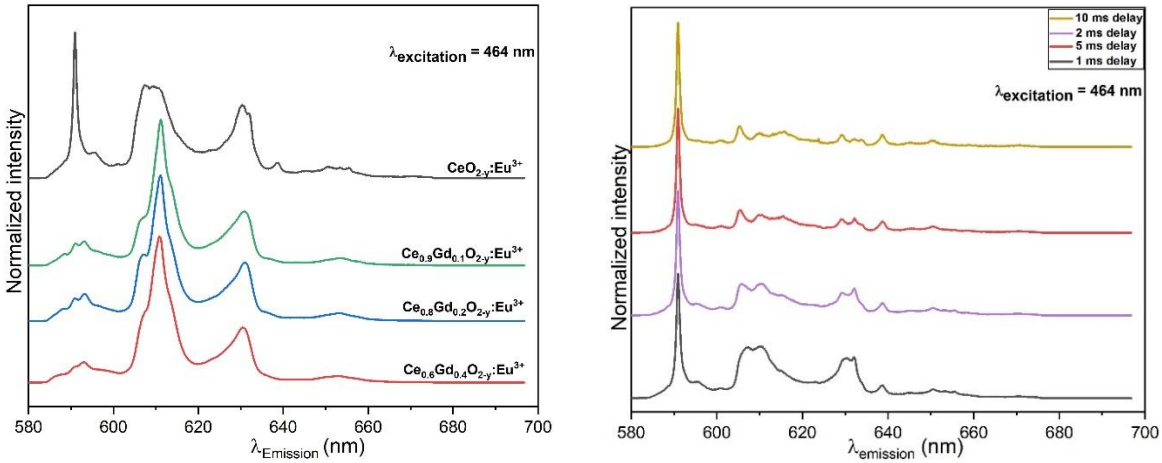

Figure 7. Emission spectra of Eu^{3+}-doped ceria with increasing Gd^{3+} content (left) (Δt = 100 µs) showing the spectral range of the $^5D_0$–$^7F_0$ to $^5D_0$–$^7F_4$ luminescence bands of Eu^{3+}. CeO_{2-y}: Eu^{3+} at different delays, Δt after the laser pulse (right). Emission spectra were recorded at RT and $\lambda_{excitation}$ = 464 nm.

Inspection of the emission spectra showed rather broad emission peaks, e.g. the $^5D_0$-$^7F_2$ transition (see Figure 7, left). Since the emission spectra were collected under direct excitation at $\lambda_{excitation}$ = 464 nm, Eu^{3+} ions located at different sites contribute to the recorded luminescence. The non-selectivity originates from using the $^5D_2$-$^7F_0$ transition for excitation, which splits into up to five potentially overlapping transitions for each species. Nevertheless, differences between the different GDC mixed oxides originate from increased variety in coordination environments of the Eu^{3+} dopants. With rising Gd^{3+} content, more and more defect sites are introduced, giving rise to greater structural variations.

Due to the spectral broadening effects, an attempt for site-selective excitation of the $^5D_0$-$^7F_0$ transition (which does not split in the crystal field) at room temperature failed. In order to identify different Eu^{3+} species from the time-resolved luminescence spectra collected at RT, PARAFAC analysis was performed. In Figure 8, the decay curves, spectra and speciation results obtained after deconvolution for $Ce_{1-x}Gd_xO_{2-y}$: Eu^{3+} are shown.

Two different Eu^{3+} species were identified in the samples after deconvolution. The PARAFAC analysis yields luminescence decay kinetics as well as the luminescence spectra for each species identified to contribute to the luminescence signal after excitation at $\lambda_{excitation}$ = 464 nm. For the CeO_{2-y}: Eu^{3+} sample, Figure 8 (top left), a high symmetry Eu^{3+} species (HS, characterized by its sharp emission peak at 591 nm and long luminescence lifetime (~3 ms)) and a low symmetry Eu^{3+} species (LS) were identified. Both differ greatly in spectral intensity distribution as well as in luminescence decay kinetics.

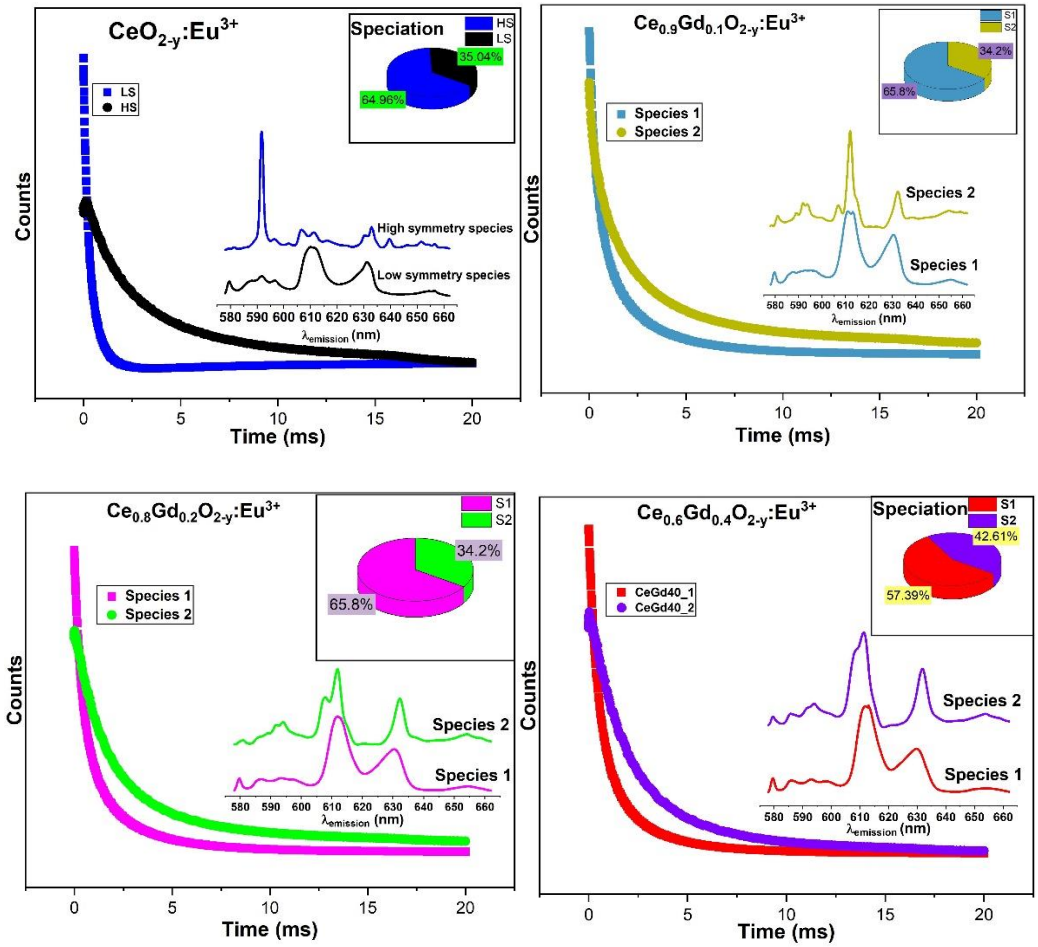

Figure 8. PARAFACed results of the luminescence spectra ($\lambda_{excitation}$ = 464 nm, RT) of $Ce_{1-x}Gd_xO_{2-y}$: Eu^{3+} (top and bottom).

The HS species resembles the spectrum measured after selective CT excitation and allows to assess the quality of the deconvolution by comparison (Figure 9, black curve), and allows to eliminate additional background peaks in unprocessed time-delay measurement data (ochre curve).

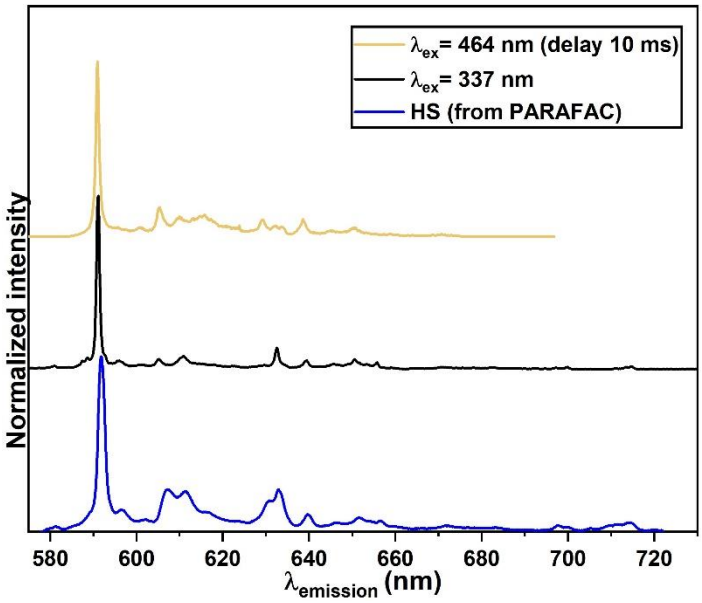

Figure 9. Luminescence spectra of the high-symmetry species in CeO_{2-y}: Eu^{3+} obtained through different excitation mechanisms: ochre curve, $\lambda_{excitation}$ = 464 nm with a long delay (10 ms); black curve, charge transfer excitation at $\lambda_{excitation}$ = 337 nm yielding only HS emission; blue curve, a HS spectrum from PARAFAC deconvolution.

For the ceria samples containing Gd^{3+}, no high symmetry Eu^{3+} species were found (see Figure 8, right, bottom left and right), instead in all cases two Eu^{3+} species with lower symmetry (judging from the ratio of the $^5D_0$-$^7F_1$ to $^5D_0$-$^7F_2$ ratio, the presence of a $^5D_0$-$^7F_0$ transition, and from the threefold Stark splitting of the $^5D_0$-$^7F_1$ transition). The deconvolution in single component spectra using PARAFAC on the RT luminescence data did not fully separate the luminescence spectra originating from different Eu^{3+} species expected to be present in the samples.

That can be seen: i) in the deconvoluted spectrum of the high symmetry species (see Figure 9), which is still "contaminated" by other luminescence signals, ii) from the width of the luminescence bands, and iii) considerations about the amount of possible symmetries of NN and NNN defect sites with rising Gd^{3+} content (nearest neighbor and next-nearest neighbor). There are similarities in the spectra and decay times of the species for Gd^{3+} containing ceria and it can be concluded that the same low symmetry species (maybe slightly distorted) are found in the nanomaterials (Table 8). Table 8 shows the species decay times in the individual mixed oxides.

Table 8. Species decay times in the $Ce_{1-x}Gd_xO_{2-y}$: Eu^{3+} mixed oxides.

Sample	Species	Decay time (μs)
CeO_{2-y}: Eu^{3+}	HS	2944±4
	LS	328±3
$Ce_{0.9}Gd_{0.1}O_{2-y}$: Eu^{3+}	1	729±8
	2	1546±6
$Ce_{0.8}Gd_{0.2}O_{2-y}$: Eu^{3+}	1	2012±2
	2	711±8
$Ce_{0.6}Gd_{0.4}O_{2-y}$: Eu^{3+}	1	2264±18
	2	736±7

In order to improve the resolution, site-selective luminescence measurements were performed (excitation of the $^5D_0$-$^7F_0$ transition) in combination with ultra-low temperature (T = 4 K) to reduce the inhomogeneous spectral broadening.

4.2.2.2 Site-selective high-resolution emission spectroscopy at ultra-low temperature

In Figure 10, the total luminescence spectra (TLS) for Eu^{3+} doped ceria and Eu^{3+} doped ceria-gadolinium samples are shown. The TLS show the emission intensity (z-axis) (based on the brightness of the spots in the Figure) at different excitation wavelengths ($\lambda_{excitation}$, y-axis) and emission wavelengths ($\lambda_{emission}$, x-axis).

Since the $^5D_0$-$^7F_0$ transition of Eu^{3+} is non-degenerate, this transition is especially valuable to resolve the emission spectra of Eu^{3+} dopants located on distinctly different sites, depending on the crystal field strength and symmetry. A broadening of the excitation band indicates a distribution of Eu^{3+} ions in slightly different coordination environments, which differ in distances to and nature of the neighboring ions. The comparison of the TLS presented in Figure 10 immediately shows a significant difference between the Eu^{3+}-doped ceria (left, top) and the other samples, which contained Gd^{3+}.

Comparing the excitation spectra (Y- axis), Eu^{3+} doped ceria displays three distinct bright and sharp spots in the TLS at excitation wavelengths $\lambda_{excitation}$ = 579.8, 580.2 and 580.4 nm, respectively. In contrast, for the Gd^{3+}-containing samples, one broadened excitation band was found, which has an intensity maximum shifted to lower excitation wavelengths. As seen from the CeO_{2-y}: Eu^{3+} TLS, the Eu^{3+} species at $\lambda_{excitation}$ = 580.4 nm is the most red shifted, which implies that it is experiencing the strongest crystal field in this sample (as shown by the crystal field strength parameter, N_v (B_2q) in Table 9, which could be attributed to smallest number of defects in the close vicinity of the Eu^{3+} ion. The species excited at $\lambda_{excitation}$ = 580.2 nm are experiencing a medium field as they are less red shifted than

the earlier. This could be attributed by the loss of oxygen ions occupying the NNN position in relation to the Eu^{3+} in this site, slightly weakening the electrical field experienced by Eu^{3+}. Finally, the species which is excited at $\lambda_{excitation}$ = 579.8 nm is experiencing the weakest field. This could be due to the removal of an O^{2-} ion from the NN position, hence there is probably the largest number of vacancies around the Eu^{3+}.

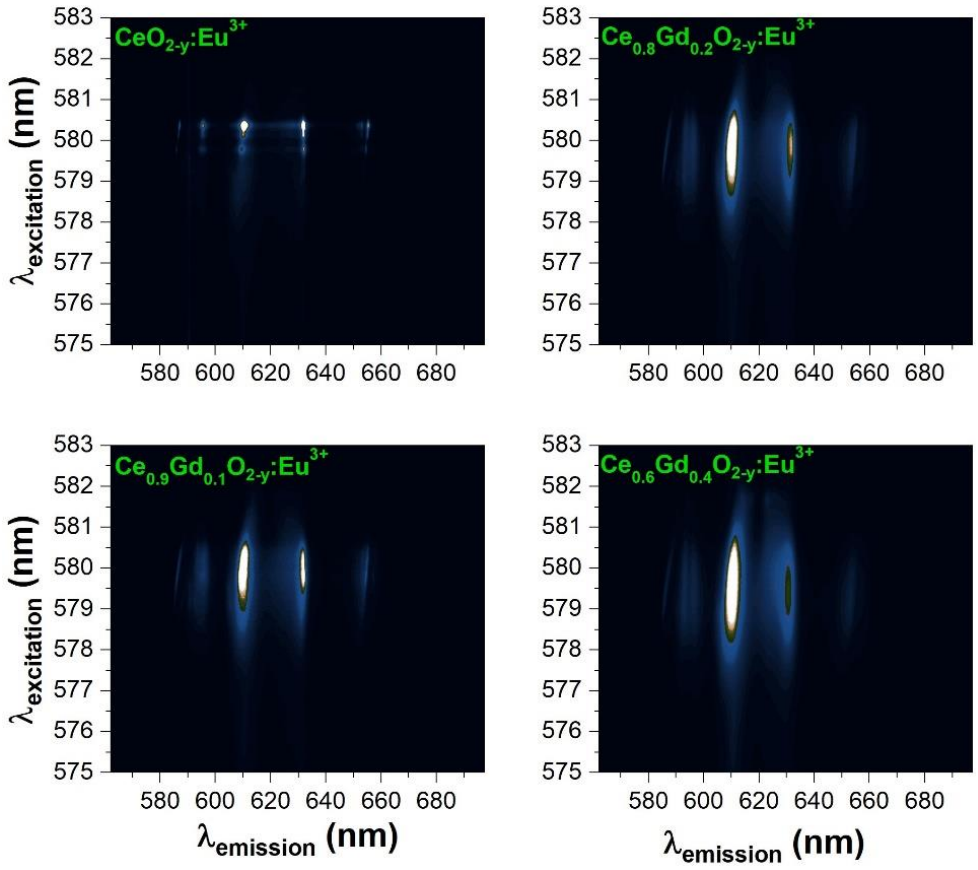

Figure 10. Total luminescence spectra (logarithmic intensity/color scale) of CeO_{2-y}: Eu^{3+}, $Ce_{0.9}Gd_{0.1}O_{2-y}$: Eu^{3+}, $Ce_{0.8}Gd_{0.2}O_{2-y}$: Eu^{3+}, and $Ce_{0.6}Gd_{0.4}O_{2-y}$: Eu^{3+} after excitation in the spectral range of the $^5D_0$–$^7F_0$ transition (575 nm < $\lambda_{excitation}$ < 583 nm) at T = 4 K. The delay after the laser pulse was 1μs with a gate width of 2 ms.

For the Gd^{3+}-containing samples the emission and excitation spectra increase in broadness with the increase in the gadolinium concentration. This indicates that the probed Eu^{3+} ions are located in less homogeneous environments compared to CeO_{2-y}: Eu^{3+}, with more variation of charge (more vacancies) and distances (lattice expansion), resulting in differing crystal field strength felt by more individual Eu^{3+} ions. With the increase in Gd^{3+} ions, the Eu^{3+} signal broadens only asymmetrically towards shorter wavelengths, as more and more oxygen vacancies are introduced for charge compensation, leading to weaker and weaker crystal fields around the Eu^{3+} ions.

The crystal field splitting parameter N_v (B_2q) for the Eu^{3+} ions is calculated for three different excitation wavelengths according to equations 1-3 and shown in Table 9.

Table 9. N_v parameters of the species in the $Ce_{1-x}Gd_xO_{2-y}$: Eu^{3+} samples obtained from the TLS

Sample	λ_{ex} (nm)	N_v parameter (cm^{-1})
$Ce_{0.6}Gd_{0.4}O_{2-y}$: Eu^{3+}	579.8	1291
	580.2	1116
	580.4	1026
$Ce_{0.8}Gd_{0.2}O_{2-y}$: Eu^{3+}	579.8	1289
	580.2	1179
	580.4	1125
$Ce_{0.9}Gd_{0.1}O_{2-y}$: Eu^{3+}	579.8	1407
	580.2	1184
	580.4	1205
CeO_{2-y}: Eu^{3+}	579.8	1403
	580.2	1127
	580.4	1111

The results (see Table 9) show that generally the variances in N_v (B_2q) are small, showing that there are only minor differences between the different locations for Eu^{3+} in the host lattice. Nevertheless, these differences can be resolved under site-selective excitation conditions at T = 4 K, whereas the PARAFAC analysis of the RT data only revealed two species, which resemble the signals visible in the TLS with the exception of the high-symmetry species measured for CeO_{2-y}: Eu^{3+}.

In Figure 11, the site selective emission spectra of the samples collected at $\lambda_{excitation}$ = 579.8 nm and $\lambda_{excitation}$= 580.4 nm are compared. The emission spectra collected at different excitation wavelength show only slight differences for each sample with respect to the Stark splitting, position and spectral width of the emission bands. The increase in Gd^{3+} content of the sample lead to a more pronounced effect on the emission spectra (see Figure 11). Here, for the same excitation wavelength the emission bands become broader with increasing Gd^{3+} concentration. Moreover, also the spectral intensity distribution (e.g., the Stark splitting of the $^5D_0$-$^7F_1$ transition) changed. The biggest change was found when going from "no Gd^{3+}" to "Gd^{3+}", but gradual alterations within the set of Gd^{3+}-containing samples are clearly visible. Like the excitation spectra, the emission spectra also indicate that the number of slightly different environments for the Eu^{3+} ions in the host lattice increase with Gd^{3+}-content (inhomogeneous broadening).

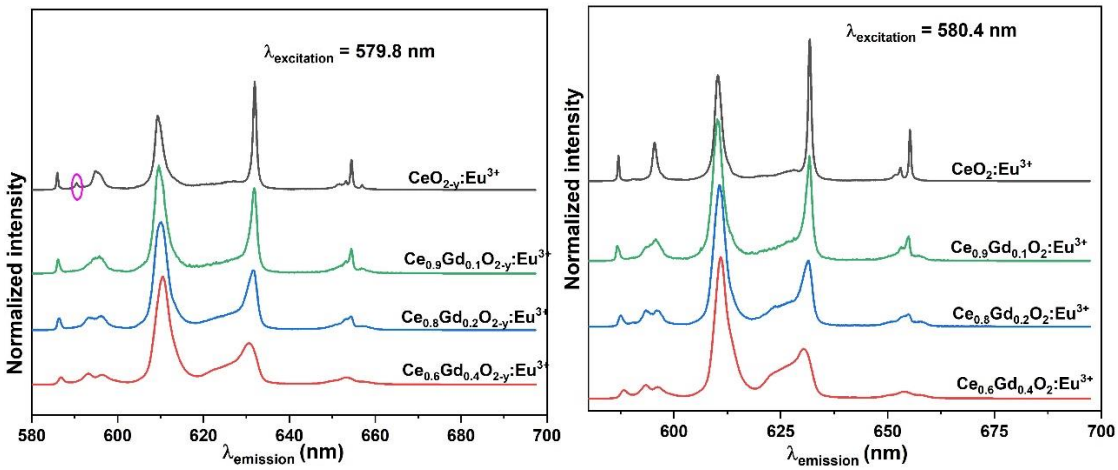

Figure 11. Emission spectra from site selective excitation of $Ce_{1-x}Gd_xO_{2-y}$: Eu^{3+} at $\lambda_{excitation}$ = 579.8 and 580.4 nm, respectively and T = 4 K). Delay after laser pulse was set at 1 µs and gate width at 2 ms.

As seen from Figure 11, the $^5D_0$-$^7F_2$ transition (in the spectral range of ~610 < $\lambda_{emission}$ < 640 nm) is dominant in all the samples, implying that the probed Eu^{3+} ions are not in the site with inversion symmetry[59,167]. Based on the stark splitting in the magnetic and electric dipole transitions ($^5D_0$-^7F_J, J = 1, 2) as well as the fact, that the luminescence was excited via $^5D_0$-$^7F_0$ transition, the symmetry at the location of the Eu^{3+} ions is low and most likely to be among the point groups C_{2v}, C_S, C_2 and C_1, which are part of the cubic symmetry group.

Interestingly, for the CeO_{2-y}: Eu^{3+} sample, a small emission peak at $\lambda_{emission}$ ~ 591 nm is still visible for $\lambda_{excitation}$ = 579.8 nm (see Figure 11, left, circled in Magenta). At RT under non-site-selective excitation conditions, this was a dominant emission peak and is attributed to Eu^{3+} ions in a high symmetric coordination environment. The fact that this transition is also seen under a site-selective excitation at 4 K via the $^5D_0$-$^7F_0$ transition (although the intensity was weak) could have two reasons: either that some minor distortions of the symmetry (e.g., very small difference in angles, bond length etc.) are present responsible for a relaxation of the selection rule rendering this transition strictly forbidden, or that energy is transferred to the high-symmetry sites from lower different sites. It is only visible in the CeO_{2-y}: Eu^{3+} for $\lambda_{excitation}$ = 579.8 nm and disappears for the Gd^{3+}-containing samples, along with the probability of having an undisturbed CeO_2 cubic dopant environment without vacancies.

In order to further evaluate the species distributions in the different samples, TLS (T = 4 K) were recorded at different initial delay times (Δt_1 = 10 µs, Δt_2 = 100 µs, and Δt_3 = 1000 µs, respectively) and processed in a PARAFAC analysis. In contrast to the RT data, in which the emission spectra and the luminescence decay kinetics were used, here the emission and excitation information was used to resolve the Eu^{3+} speciation in the samples. In Figure 12, the results of the PARAFAC analysis for the

samples are shown. In comparison to the PARAFAC analysis of the RT data (*vide supra*) now four Eu^{3+} species were identified (marked as S1 – S4 in CeO_{2-y}: Eu^{3+}, $Ce_{0.9}Gd_{0.1}O_{2-y}$: Eu^{3+} $Ce_{0.8}Gd_{0.2}O_{2-y}$: Eu^{3+} and Sp1-Sp4 in $Ce_{0.6}Gd_{0.4}O_{2-y}$: Eu^{3+}).

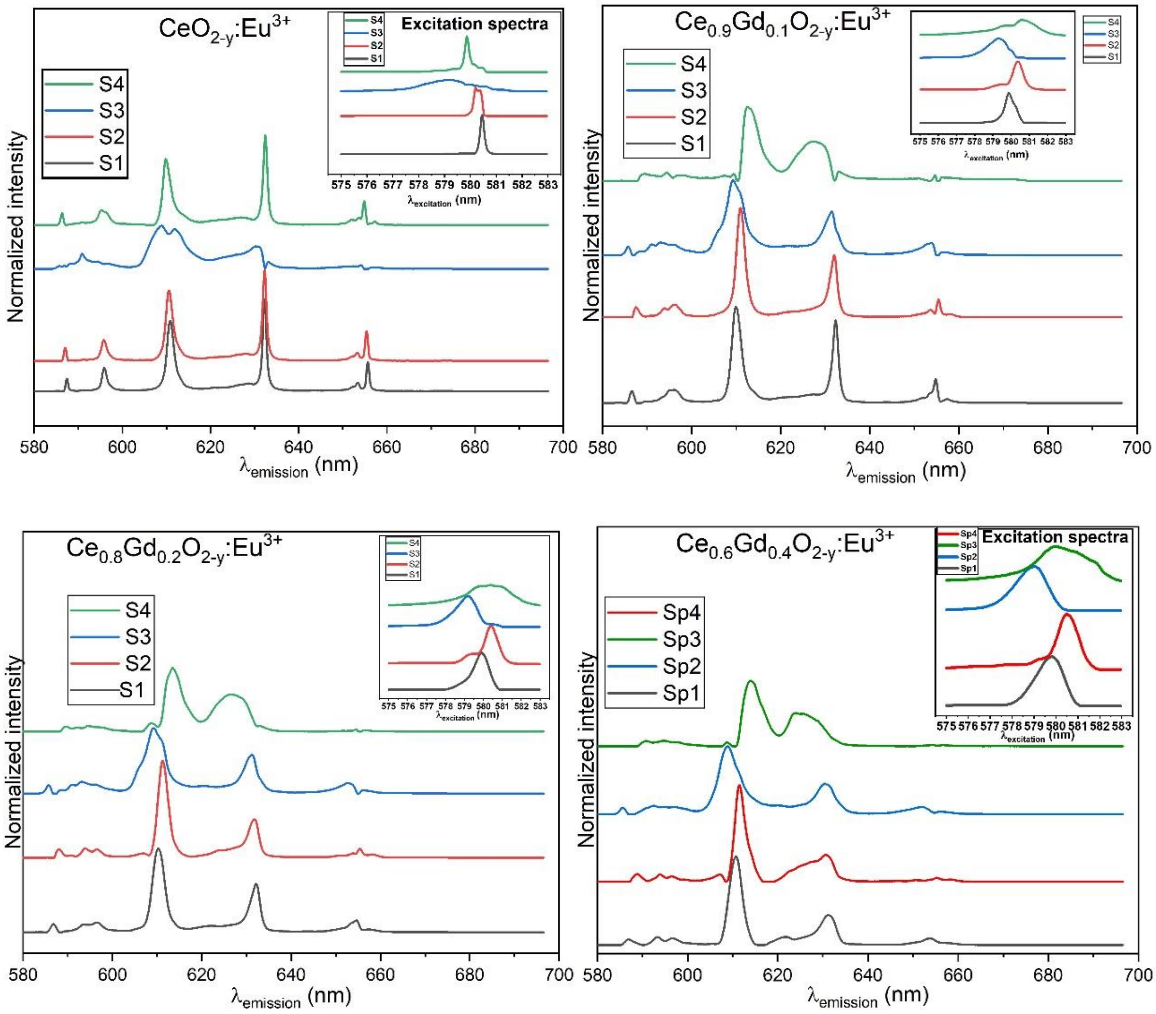

Figure 12. Results of the PARAFAC analysis based on the TLS data (initial delay Δt_1 = 10 µs, Δt_2 = 100 µs, and Δt_3 = 1000 µs, respectively; T = 4 K). Emission and excitation spectra (inset) for CeO_{2-y}: Eu^{3+} (top left). In the emission spectrum S3 a minor peak at $\lambda_{emission}$ ~ 591 nm attributed to a "high symmetry" Eu^{3+} species can be seen. Shown top right, bottom left and bottom right are the respective spectra for $Ce_{0.9}Gd_{0.1}O_{2-y}$: Eu^{3+}, $Ce_{0.8}Gd_{0.2}O_{2-y}$: Eu^{3+} and $Ce_{0.6}Gd_{0.4}O_{2-y}$: Eu^{3+}.

In Figure 12 (left, top) the deconvoluted emission and excitation spectra of the CeO_{2-y}: Eu^{3+} sample are shown. For this sample, three relatively sharp luminescence spectra were found: S1, S2 and S4, complemented by sharp bands in their respective excitation spectra. Due to their very similar spectral features, the deconvolution of S1 and S2 is incomplete, leading to a double peak in the excitation spectrum relating to S2 (see inset). This may also mean that the distributions of the species are different,

but are in the same environment, hence the broad excitation spectra resulting in the "similar" emission spectra.

For S4 a distinctly shifted $^5D_0$-$^7F_0$ transition (excitation spectrum) and a slightly different emission spectrum in the $^5D_0$-$^7F_1$ range was obtained. Significant differences are visible in S3, with a distinctly broadened $^5D_0$-$^7F_0$ excitation. The artifacts in the spectrum indicate that this is not a "pure" species, but a combination of contributions from different of sites (a characteristic peak from the high symmetry species at $\lambda_{emission} \sim 591$ nm and broad peaks in the $^5D_0$-$^7F_2$ emission range).

In the case of the Gd^{3+} mixed ceria samples the same principal spectra (S1-S4 and Sp1-Sp4) are found for all samples (see Figure 12), in each case the blue S3 and Sp3 are showing most similarity across all materials. Again, there seem to be four distinguishable sites that are favored for Eu^{3+} ions in the mixed oxide materials, but featuring more secondary variations, such as extrinsic NN and NNN oxygen vacancies caused by Gd^{3+}.

Deconvolution of the luminescence data measured at three delay times at 4 K yielded luminescence decay kinetics. As only three different delays were used in the experiment (due to time constraints), the error of the decay times is rather large (three data points for a two-parameter exponential). Figure 13 shows the decay curves of the species present in the samples. The respective decay times of the species S1, S2, S3 and S4 for CeO_{2-y}: Eu^{3+}, $Ce_{0.9}Gd_{0.1}O_{2-y}$: Eu^{3+} and $Ce_{0.6}Gd_{0.4}O_{2-y}$: Eu^{3+} are shown in Table 10.

Table 10. Decay times of the species S1, S2, S3 and S4 for CeO_{2-y}: Eu^{3+}, $Ce_{0.9}Gd_{0.1}O_{2-y}$: Eu^{3+} and $Ce_{0.6}Gd_{0.4}O_{2-y}$: Eu^{3+}.

Species	Sample decay times (μs)		
	CeO_{2-y}: Eu^{3+}	$Ce_{0.9}Gd_{0.1}O_{2-y}$: Eu^{3+}	$Ce_{0.6}Gd_{0.4}O_{2-y}$: Eu^{3+}
S1	970.4±120.7	1400.5±3.6	1105.6±100.4
S2	910.9±34.6	1397±14.3	1219.1±162.6
S3	482.2±13.9	1424.7±117.2	583.9±69.9
S4	980.7±107.4	841.9±125.8	983.6±64.9

There are similarities in the decay times (see Table 10) for the species in the samples (especially for S1 and S2 for each sample) which is in line with the "closeness" of the emission spectra (see Figure 13). This could be due to the fact that these species are in the same environment, that is similar sites, (although their distribution are different), but still are excited around the same wavelength and then portray similar decay kinetics.

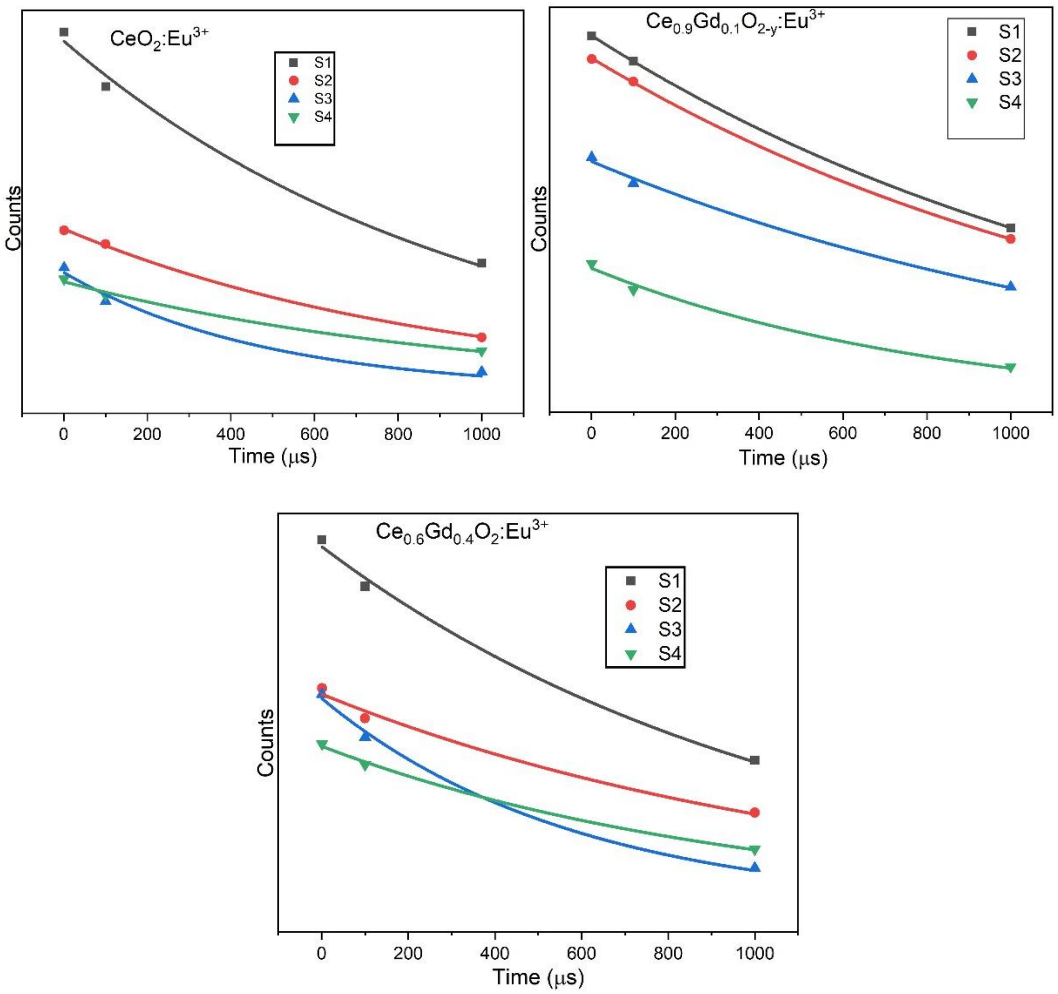

Figure 13. Decay curves for CeO_{2-y}: Eu^{3+} (top, left), $Ce_{0.9}Gd_{0.1}O_{2-y}$: Eu^{3+} (top, right) and $Ce_{0.6}Gd_{0.4}O_{2-y}$: Eu^{3+}, (bottom) species obtained from three delay times (1 µs, 100 µs and 1000 µs), at T=4K

4.2.2.3 The asymmetry ratio, R

As shown in Table 11, R (calculated using equation 4), slightly increase with Gd^{3+} ion concentration. In this case, it has a good correlation with the Judd-Ofelt parameters Ω_2 and Ω_4 (see Table 11). Deconvolution of spectra by PARAFAC gives a good idea about the number of Eu^{3+} species present in a sample and to get more information about the separated species, Judd-Ofelt analysis can be carried out.

4.2.2.4 Judd Ofelt parameters

The experimental dipole strength, Ω_2 parameter is sensitive to the local structure and configuration of the host material and can be correlated with the asymmetry and covalency of the lanthanide ion site through the nephelauxetic effect (short range effect) and Ω_4 is related to long-range effect[94,168].The larger the Ω_2, the stronger the covalence[168-170]. The results show that the covalence increases with the amount of Gd^{3+} ions. The insignificant difference in the Ω_2 and Ω_4 values of the CeO_{2-y}: Eu^{3+} sample

measured at 337 nm would point towards a centrosymmetric environment around the Eu^{3+} ions. This is also supported by the small R value. The Ω_2 and Ω_4 values of CeO_{2-y}: Eu^{3+}, high symmetry species are comparable to that of the species pertaining to the CeO_{2-y}: Eu^{3+} sample measured at 337nm.

Derived quantities from Judd-Ofelt theory shown in Table 11, radiative lifetime and intrinsic quantum yield (luminescence quantum efficiency), provide information that relates directly to the investigated material. The rate of depopulation of an excited state can be determined by the radiative lifetime $\tau_{R,}$ which is the inverse of the total radiative transition rates (A). For the CeO_{2-y}: Eu^{3+}, the high symmetry species has double the value of the radiative lifetime (23.9 ms) as compared to the low symmetry species (12.5 ms) of the same sample. For the 20 mol % Gd^{3+} sample, the radiative lifetimes for species 1 is 11 ms and that of species 2 is 9. 68 ms. Considering the sample with 40 mol % Gd^{3+}, the radiative lifetimes for species 1 is 9.48 ms and that of species 2 is 8.36 ms, thus with the increase in the Gd^{3+} doping level, the difference in the radiative lifetimes of the two species of individual samples become smaller and smaller. Also, incorporating 40 mol % Gd^{3+} into the Eu^{3+} doped ceria system results in a significant decrease in the value of τ_R. This could be attributed by the fact that, with incorporation of a high Gd^{3+} concentration, defects in the host matrix could open pathways to non-radiative losses[170].

Table 11-. Judd-Ofelt intensity parameters, radiative and non-radiative transition rates, quantum efficiencies and asymmetry ratios of deconvoluted RT Eu^{3+} emission from $Ce_{1-x}Gd_xO_{2-y}$: Eu^{3+} nanoparticles excited at a wavelength of 464 nm 337 nm (only for CeO_{2-y}: Eu^{3+}).

Sample, species	Ω_2 ($cm^2/10^{-20}$)	Ω_4 ($cm^2/10^{-20}$)	A (s^{-1})	A_{NR} (s^{-1})	η (%)	R
CeO_{2-y}: Eu^{3+}, low symmetry species	5.15	3.1	79.89	3145.92	2.6	3.34
CeO_{2-y}: Eu^{3+}, high symmetry species	2.22	1.14	41.82	329.92	12.8	1.44
CeO_{2-y}:Eu^{3+}, λ_{ex}= 337 nm	1.24	1.08	32.24	-	-	0.81
$Ce_{0.6}Gd_{0.4}O_{2-y}$: Eu^{3+}, Species 1	7.14	4.38	105.42	415.41	19.7	4.67
$Ce_{0.6}Gd_{0.4}O_{2-y}$: Eu^{3+}, Species 2	7.9	5.83	119.57	1732.28	6.2	5.12

4.3 Conclusion

$Ce_{1-x}Gd_xO_{2-y}$: Eu^{3+} ($0 \leq x \leq 0.4$) nanoparticles were synthesized using an industrial grade spray pyrolysis method. TEM data and XRD data reveal that the particles are nano-sized and of roughly cubic shape and crystal structure ($Fm\bar{3}m$). Raman data revealed four vibrational modes exhibited by Gd^{3+} containing samples whereas CeO_{2-y}: Eu^{3+} displays only two. The time-resolved emission spectra of Eu^{3+} recorded at $\lambda_{excitation}$ = 464 nm and RT showed that mixing with Gd^{3+} results in a significantly different emission spectra from pure ceria (with the very sharp distinct emission peak at $\lambda_{emission}$ = 591 nm in the case of pure ceria). PARAFAC analysis was performed to extract different Eu^{3+} spectra from the time-resolved

luminescence data collected at RT, and the deconvolution yielded luminescence decay kinetics as well as the associated luminescence spectra of two species for each of the samples.

For pure ceria, one of the species found is a high-symmetry site, that can also be excited selectively (CT at 337 nm) or measured with a delay of 10 ms (due to faster luminescence decay for lower symmetry species), underlining the usefulness of this approach to assign emission peaks to lattice sites and extract structural information. However, the deconvolution in single component spectra using PARAFAC on RT luminescence data did not fully resolve spectroscopically (and structurally) very similar sites assumed to be present in the samples. Previous studies using high-resolution spectroscopy revealed up to seven different dopant sites for Eu^{3+} dopants in small ceria nanomaterials. Thus, high-resolution luminescence data measured after excitation of the $^5D_0$-$^7F_0$ transition at T = 4 K was analyzed to resolve small spectroscopic differences between different sites further. Both non-degenerate states are not affected by the Stark splitting, but the crystal field "strength". The intensive high symmetry emission from the previous experiments is not visible even in pure ceria, supporting that this emission contribution comes from Eu^{3+}on the highest symmetry site, in which a $^5D_0$-$^7F_0$ transition is highly unlikely (forbidden).

From the shape and width of the observed distinct excitation maxima in the TLS of CeO_{2-y}: Eu^{3+} it can be concluded that the probed Eu^{3+} ions are located in three relatively homogenous, distinct coordination environments (three species), whereas in the $Ce_{1-x}Gd_xO_{2-y}$: Eu^{3+} more oxygen vacancies and more variations in structure are introduced. The three species in the TLS of pure ceria are probably related to the most stable configurations of the NN and NNN position of the O^{2-} vacancy, and the position of the ion responsible for charge compensation Ce^{3+}or Eu^{3+}. With rising Gd^{3+} concentration, an overall hypsochromic shift of the $^5D_0$-$^7F_0$ transition indicates that the average charge density around the Eu^{3+} ions is decreased, as more extrinsic vacancies are introduced into the ceria lattice. Furthermore, the broadened excitation spectra indicate that the probed Eu^{3+} ions are located in much less homogeneous environments compared to CeO_{2-y}: Eu^{3+}, while retaining the same general symmetry.

In order to further evaluate the data, the PARAFAC model was applied to the high-resolution TLS of all samples, but limiting the time component to only three points to retain good excitation resolution. CeO_{2-y}: Eu^{3+} yielded four spectra, with one of the species having a visible contribution by the emission from Eu^{3+} ions in the high symmetry coordination environment, superimposed on broader features. The other emission spectral signals appear rather similar and represent the previously identified three distinct species in pure ceria. For the Gd^{3+}-containing samples the PARAFAC analysis also yielded four different species, which are more clearly separated by in their excitation and emission spectra. Due to the presence of Gd^{3+}, the coordination environment for the Eu^{3+} ion in the host lattice is diversified.

Conclusively, the excitation of the species in the samples via the $^5D_0$-$^7F_0$ leads to a maximum $^7F_1$ splitting of three in most cases (except for the high symmetry species). For higher Gd^{3+} content samples, the $^5D_0$-$^7F_2$ transition had high intensity, indicating lower symmetry. These findings point towards a C-type symmetry at the location of the Eu^{3+} ions. It is most likely to be among the point groups C_{2v}, C_S, C_2 and C_1, which are part of the cubic symmetry group.

It is strongly believed that the presented PARAFAC algorithm is especially useful for the identification of Eu^{3+} species in challenging samples where many sites contribute to the overall emission. In pure ceria, room temperature, low resolution data accurately reproduced the high symmetry species and a second spectrum very similar to the superimposed, broadened high-resolution spectra gained with considerable effort at 4 K, using narrow-bandwidth, tunable laser source. This underlines the value of this approach, which gets amplified by good resolution along the dimensions of the algorithm, for Eu^{3+} spectroscopy that means in excitation and emission wavelength, and time.

Chapter 5: Monitoring structural changes induced by thermal subjection at two temperatures on Eu^{3+} doped ceria YSZ supported nanocomposites

5.1 Introduction

Impregnation is an established method in the formulation of heterogenous catalysts[75,76]. This is where a specific amount of precursor solution for formation of an active catalyst phase is introduced onto a solid support, which is repeatedly impregnated and dried to remove the imbibed solvent. Depending on the amount of precursor solution used, the phase composition is controlled. The impregnation technique has wide application in preparing supported nano-catalysts as it is easy to control and shows reliable reproducibility[77]. The dispersion of ceria or ceria-based materials onto the surface of support materials such as yttrium stabilized zirconia (YSZ) modifies physical and chemical properties of nanomaterials for specific applications. Ceria-based materials improve catalytic activities as a result of the OSC of ceria, which is associated with the formation of oxygen vacancies, as ceria cycles between its Ce^{4+}/Ce^{3+} states. Among notable applications of these ceria-based materials are as electrodes for SOFC and catalysts for reforming processes[45,171,172].

Cerium is the most abundant lanthanide element on earth[77]. However, with increasing demand a reduction in usage is desired for industrial applications, thus minimizing its use through ceria-based composite preparations[51] is a viable strategy. Also, due to the technological importance of ceria, with usage, possible supply problems are inevitable. Thus, optimization of cerium oxide-based catalysts is under study. Doping ceria with trivalent ions, e.g. Eu^{3+} and other lanthanide ions, introduces oxygen vacancies, which improve the mobility of oxygen ions in the ceria lattice. This is often used to tailor structural properties of a catalyst, and in turn the catalyst performance[173,174]. Notable measurements of the $Ce_xZr_{1-x}O_2$ mixed oxides revealed outstanding properties in temperature programmed reduction (TPR) measurements upon Eu^{3+} doping[175]. Similarly, literature reports that even very small structural changes in ceria and ceria mixed oxides systems can have a big impact on catalytic activity[176]. Also, doping with Eu^{3+} introduces interesting emission properties to the materials: the spectroscopic response of the Eu^{3+}-ions is strongly dependent on the dopants site symmetry in a host lattice[177]. Exploiting the full potential of Eu^{3+} as a structural probe using selective excitation in low-temperature high-resolution emission spectroscopy, and correlating spectroscopic results with the influence of Eu^{3+} dopants on the catalytic performance of ceria catalysts has shown promise[21].

Although a significant amount of knowledge on the important characteristics of single-phase ceria-based materials has already been attained[178,179], it is crucial to expand the characterization techniques for the understanding of structure-reactivity relationships in the developing class of nanocomposite catalyst materials. However, the presence of multiple phases in nanocomposites with very small crystallite sizes complicates structural investigations[34]. Thus, the application of high-resolution

emission spectroscopy, herein referred to as fluorescence line narrowing spectroscopy (FLNS), using Eu^{3+} as a structural probe, effectively complementing the results from X-ray diffraction (XRD) and high-resolution transmission electron microscopy (HRTEM) measurements and allowing a unique insight into this class of materials is essential. Targeted doping of specific domains with the spectroscopic probe allows for a spatial resolution, enabling the investigation of individual domains present in a nanocomposite sample.

Thus, the aim of this research is to fabricate Eu^{3+}-doped ceria-zirconia multiphase nanocomposites by incipient wetness impregnation procedure using different proportions of ceria and exploit the benefits of the combination of high-resolution spectroscopy under ultra-low temperature and Eu^{3+} ions in probing the samples and complement results from XRD and HRTEM for structural analysis. The results obtained from the high-resolution emission spectroscopy data is deconvoluted by PARAFAC analysis to facilitate the gathering of information on the Eu^{3+} sites in the nanocomposites.

5.2 Results and discussion

5.2.1 XRD results

X-ray diffraction analysis was performed to follow the crystal structural changes in between two calcination temperatures (773 K and 1273 K). The XRD patterns of 15% $Ce_xZr_{1-x}O_{2-y}$: Eu^{3+}|YSZ ($0 \leq x \leq 1$) nanocomposites and the YSZ support annealed at these two temperatures and are shown in Figure 14.

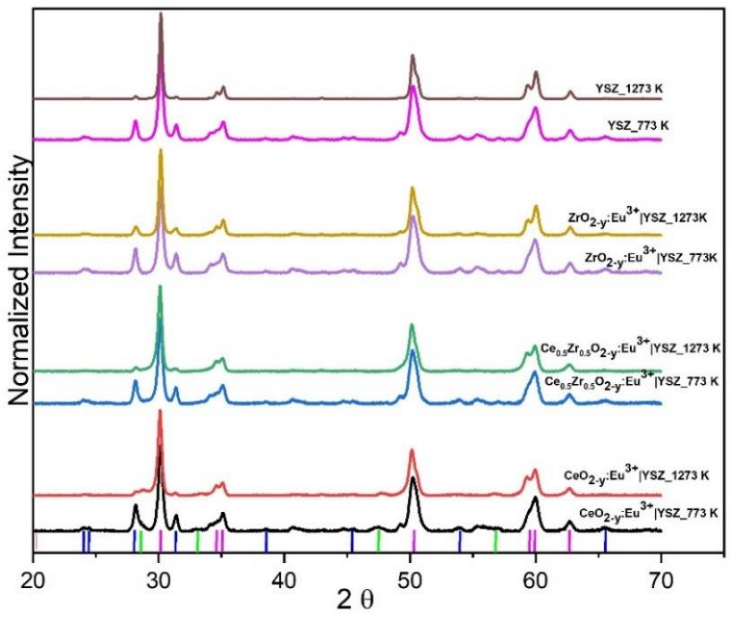

Figure 14. X-ray powder diffraction patterns of 15% CeO_{2-y}: Eu^{3+}|YSZ (NC-Ce100), 15% $Ce_{0.5}Zr_{0.5}O_{2-y}$: Eu^{3+}|YSZ (NC-Ce50), 15% ZrO_{2-y}: Eu^{3+}|YSZ (NC-Zr100) and YSZ support (calcined at 773K (bottom) and at 1273K (top) for each sample, for 2h; Cu-Kα radiation (λ= 1.54187). Monoclinic, tetragonal and cubic phases marked blue, pink and green respectively.

The diffraction patterns in all the samples heated at 773K for 2 h indicate mainly tetragonal phase (represented by pink) and this is expected as much of the material in the nanocomposite is the tetragonal phased YSZ support material (85 %), also shown in the graph. Monoclinic phases which is likely ZrO2 are also present (shown by blue in the diffractograms). Impregnating ceria onto the surface results in some peaks corresponding to the cubic phase detectable in the nanocomposites, although very faint (represented by green). The phases are compared with reference data (see the JCPDS file numbers presented in Table 12.

Table 12. Phases found in 15% $Ce_xZr_{1-x}O_{2-y}$: Eu^{3+}|YSZ nanocomposites and JCPDS file numbers from reference materials.

Sample	Phases	JCPDS file no.
NC-Ce100_773 K	monoclinic, tetragonal, cubic	98-009-4887, 98-008-9428, 00-043-1002
NC-Ce100_1273 K	tetragonal, cubic	98-008-9428, 98-002-8709
NC-Ce50 _773 K	monoclinic, tetragonal	98-006-0901, 98-008-9428,
NC-Ce50 _1273 K	monoclinic, tetragonal	98-006-0900, 98-008-9428, 98-015-5608
NC-Zr50_773 K	monoclinic, tetragonal	98-009-4886, 98-008-9428
NC-Zr50_1273 K	monoclinic, tetragonal	98-006-0900, 98-008-9428

Annealing the nanocomposites to 1273 K results in the disappearance and or reduced intensity in the monoclinic phase (blue) in the XRD patterns. This is because the monoclinic phase of zirconia is unstable above 1123 K [180]. Also, for NC-Ce100; faint peaks corresponding to a cubic phase (marked green) are still observed and they are weak as a result of small "particular" domains. This is supported by microscopy results (*vide infra*).

Figure 15 shows the XRD reflexes of 1273 K calcined NC-Ce100, NC-Ce50 and YSZ nanocomposites after subtracting the peaks due to the YSZ. The diffraction patterns from YSZ, although slightly shifted are still visible in cerium containing nanocomposites even after subtraction of peaks from YSZ. The implication is that the likelihood of phase mixing is high. The peaks corresponding to a cubic phase (marked green) in NC-Ce100 are clearly observable in the XRD pattern. However, there is no signal detectable from a potential cubic phase in NC-Ce50 which has a monolayer and is thus metastable in small particles. Microscopy shows this effect clearly especially for NC-Ce50.

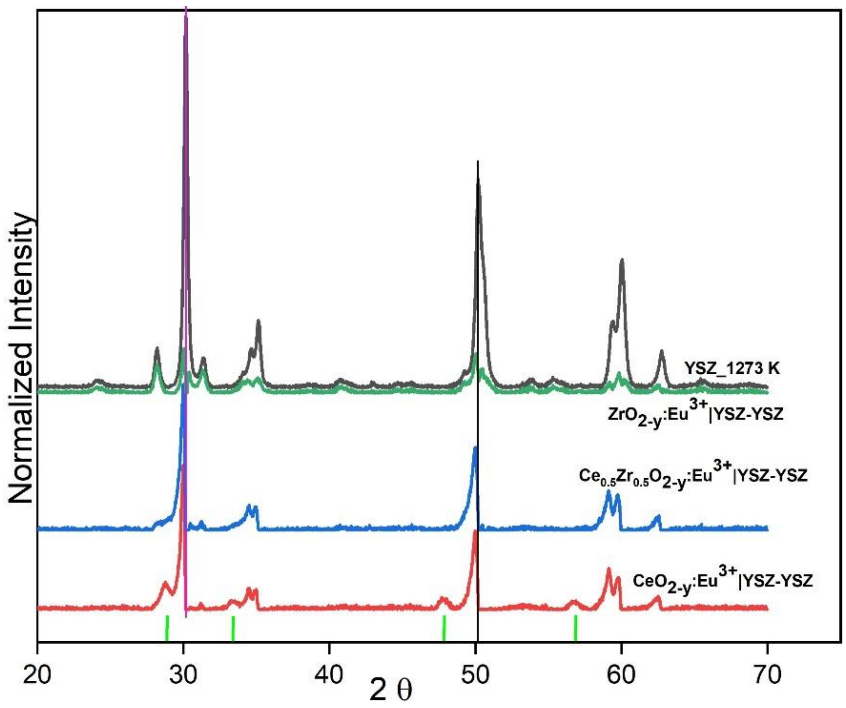

Figure 15. XRD reflexes of NC-Ce100, NC-Ce50, NC-Zr100 and YSZ nanocomposites after subtracting the peaks due to the YSZ, calcined at 1273 K.

5.2.2 Raman spectroscopy

The Raman spectra of the 15 % $Ce_xZr_{1-x}O_{2-y}$: Eu^{3+}|YSZ nanocomposites and that of YSZ|Eu^{3+} powder annealed at 773 K (bottom of each sample) and 1273 K (top of each sample) respectively for 2 h are shown in Figure 16. Raman spectroscopy was done to accurately identify the distortions of the sub-lattice oxygen and defects in the structure and also because the method is intensely sensitive for the oxygen atoms in the presence of heavy atoms (e.g. Ce and Zr).

After annealing at 773 K for 2h, the support material, YSZ| Eu^{3+} and the nanocomposites exhibit several Raman active modes because of the lower symmetry of tetragonal zirconia[85]. The Raman peaks are observed at approximately 260 (A_1g/B_1g symmetry), 380 (A_1g/B_1g symmetry), 471 (E_g symmetry) and two coupled Zr-O bending and stretching modes at around 322 cm^{-1} (B_{1g} symmetry) and at approximately 464 cm^{-1} (E_g symmetry) respectively. It is interesting to note that this mode around 464 cm^{-1} coincides with the Raman active F_2g mode of the CeO_2 fluorite structure that originates from the symmetrical breathing mode of oxygen ions around the Ce^{4+} ions, which is sensitive to disorder in the oxygen sub-lattice as a result of non-stoichiometry. This is evident for cerium containing nanocomposites that the intensities of this mode are higher. For NC-Ce100 only, a blue shift of this mode (from around 464 to approximately 470 cm^{-1}) is observed, whereas a red shift is observed for the other samples upon annealing at 1273 K.

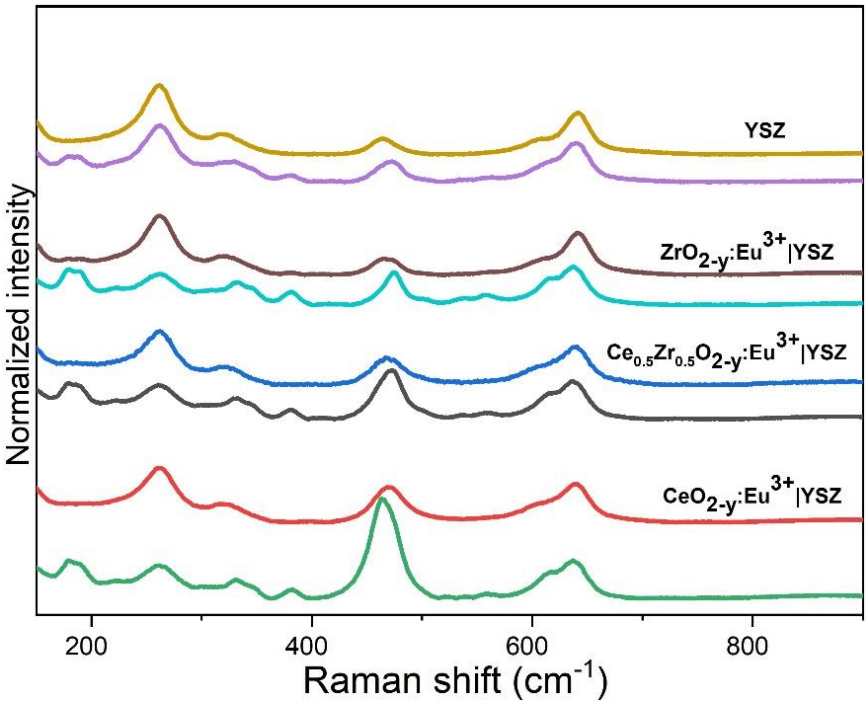

Figure 16. Raman spectra for 15% $Ce_{0.5}Zr_{0.5}O_{2-y}$: Eu^{3+}| YSZ (NC-Ce50), 15% CeO_{2-y}: Eu^{3+}|YSZ (NC-Ce100), 15% ZrO_{2-y}: Eu^{3+}|YSZ (NC-Zr100) and YSZ nanocomposites heated at 773 K for 2 h (bottom for each sample) and heated at 1273 K for 2 h (top for each sample); λ_{Laser} = 532 nm.

There is a potential formation of mixed oxide phases especially with NC-Ce50 as F_2g mode shifts to overlap with the peak in YSZ support. This may explain why the cubic signals from this nanocomposite is hardly detected by XRD. The Raman mode (frequency shoulder) at ~615 cm−1 (A_1g) and at and around 640 (E_g symmetry) cm^{-1} represents the asymmetric O-Zr-O stretching modes, which are the tetragonal phases of zirconia[181-184]. These peaks are observed, although slightly shifted, for nanocomposites and support after a calcination temperature of 1273 K which would point towards the fact that there is a conversion to a phase mixture of cubic and tetragonal zirconia. These results corroborate the results from XRD after subtracting the peaks from YSZ where there is supposed phase mixing. There is a disappearance or reduced intensity of the shoulder peak ~615 cm^{-1} upon annealing at a higher temperature which can signify an increase in the tetragonal phase fraction.

Generally, after 1273 K calcination temperature, the nanocomposites' XRD spectra "clean" up as in XRD. Also, the Raman modes are similar to those in the support material, although there are small changes in the positions. These results that line with the XRD results are possible as the YSZ support material exceed the amount of Ce/Zr impregnated on its surface.

5.2.3 Scanning transmission electron microscopy- energy dispersive X-ray spectroscopy (STEM-EDX)

The atomic scale structure of the nanocomposites was investigated by a combination of advanced STEM techniques. The EDX results for NC-Ce100 annealed at 773 K for 2 h and 1273 K for 2 h are shown in Figure 17.

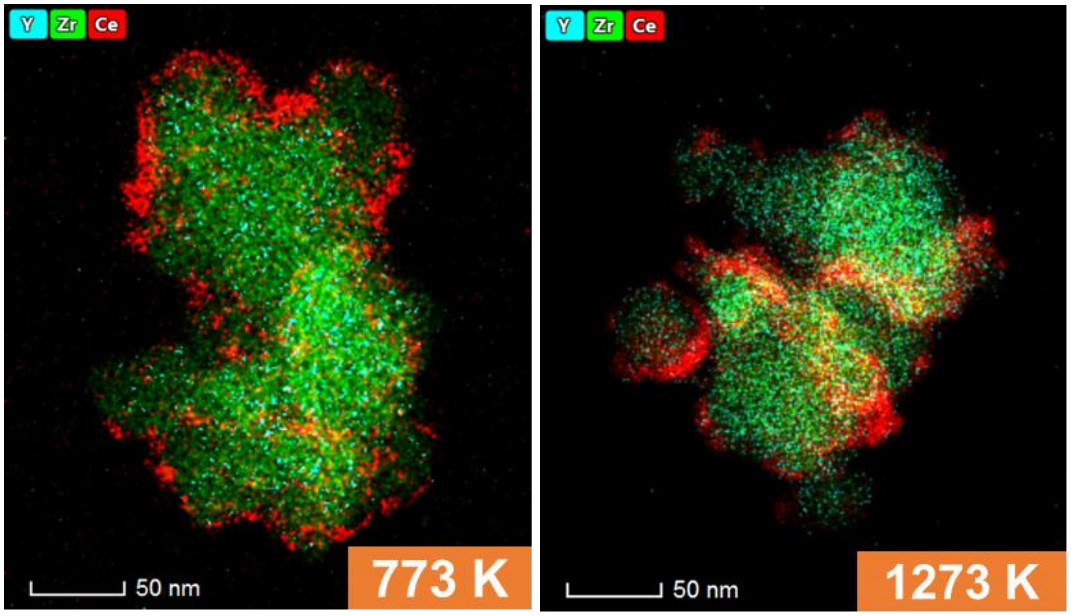

Figure 17. Energy dispersive X-Ray Spectroscopy images for NC-Ce100 heated at 773 K for 2 h (left) and 1273 K for 2 h (right).

The result for NC-Ce100 heated at 773 K show deposition of nanosized Eu^{3+} doped CeO_2 domains on the surface of the YSZ support**.** After annealing at 1273 K, there is still evidence of the CeO_2 nanoparticles on the YSZ surface (shown in Figure 17, right). The microscopy images show seemingly unchanging configuration, though crystal structure according to XRD, slightly changes. The high angle annular dark field (HAADF)-STEM for the same samples are shown in the appendix, Figure 48.

The EDX spectroscopy images for NC-Ce50 annealed at 1273 K for 2 h are shown in Figure 18. The images display cerium on the surface of YSZ after annealing the nanocomposite with 50:50 amount of Ce/Zr on the YSZ surface at 1273 K. Cerium is also homogeneously distributed over the YSZ surface, increasing the potential of mixing of phases, which is portrayed by XRD.

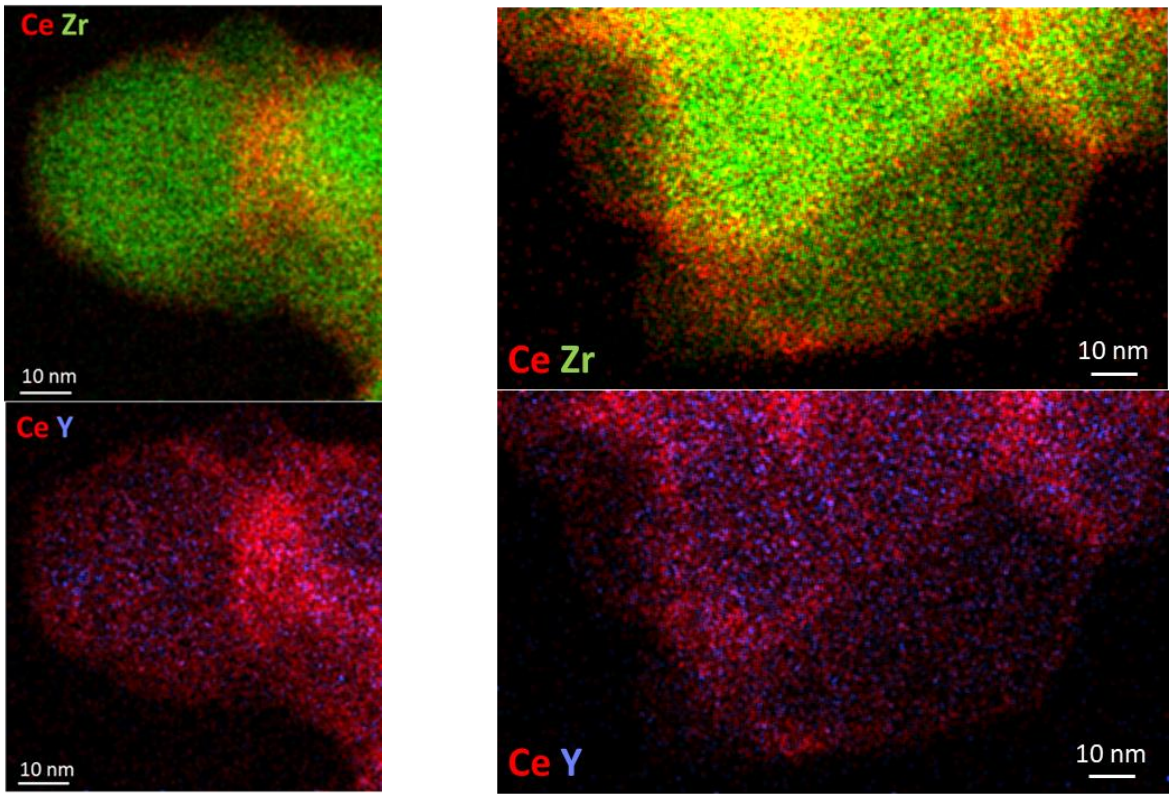

Figure 18. Energy dispersive X-Ray Spectroscopy images for 15 % $Ce_{0.5}Zr_{0.5}O_{2-y}$: Eu^{3+}|YSZ annealed at 1273 K for 2 h.

5.2.4 Fluorescence line narrowing spectroscopy (FLNS)

Figure 19 shows the total luminescence spectra of NC-Ce100, NC-Ce50, and NC-Zr100 nanocomposites annealed at 773 K for 2 h (left in each picture) and at 1273K for 2 h (right in each picture). The luminescence measurements were done under cryogenic conditions. The TLS for the 773 K annealed nanocomposites reveal one bright spot with a broadened excitation band, which signify one Eu^{3+} species in an inhomogenous environment. The excitation band has an intensity maximum shifted to lower excitation wavelengths, with increasing Zr^{4+} ions (579.0, 578.8 and 578.2 nm for NC-Ce100, NC-Ce50, and NC-Zr100 nanocomposites respectively). The orientation of the bright spot in NC-Ce50 changes and becomes brighter with the incorporation of Zr^{4+} ions. This could be as a result of a disturbance of the crystal lattice in the vicinity of the Eu^{3+} species upon introducing another different ion. This could corroborate with XRD and Raman where shifts are observed in comparison with ceria containing nanocomposite.

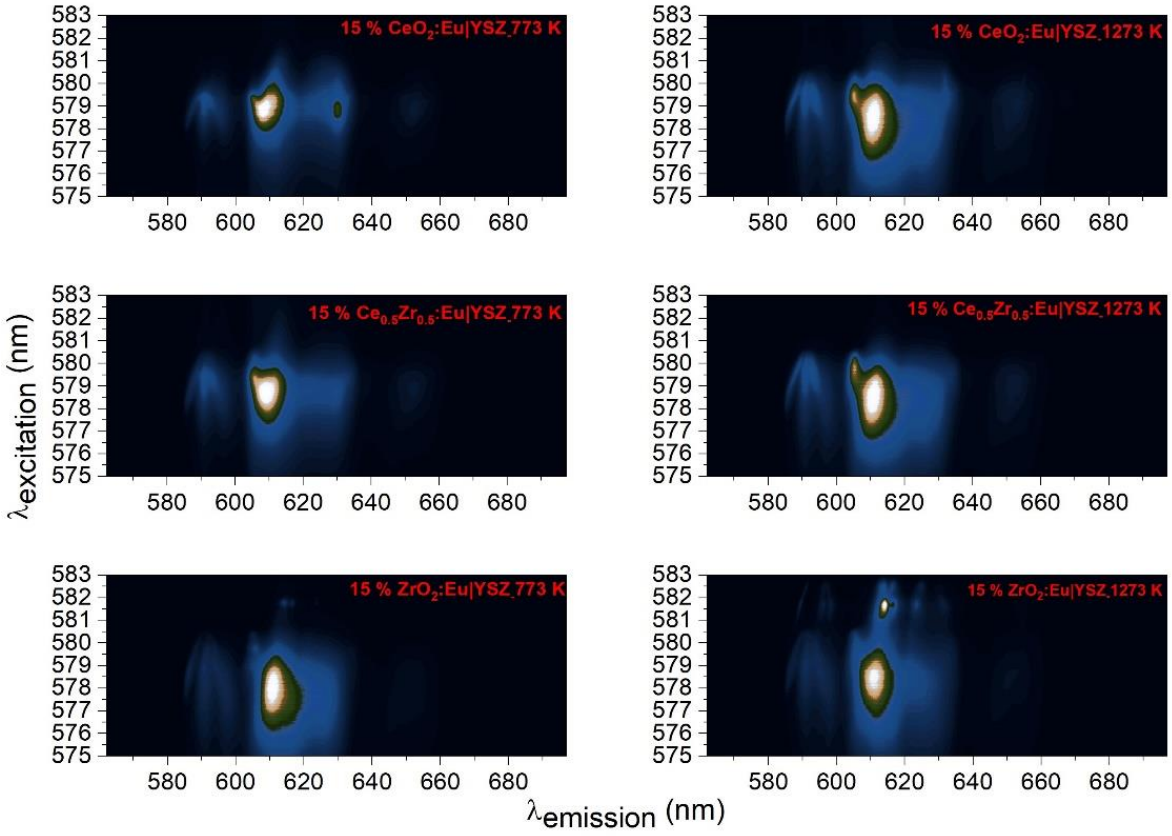

Figure 19. Total luminescence spectra (logarithmic intensity/color scale) of NC-Ce100, NC-Ce50, and NC-Zr100 nanocomposites annealed at 773 K for 2 h (left in each picture) and at 1273 K for 2 h (right in each picture). T = 4 K. Measurements were done after a delay after laser pulse of 500 ns and the gate width was 1 ms.

The TLS significantly changes after annealing the nanocomposites at 1273 K, where two distinct bright spots are observed, signifying two Eu^{3+} species. One Eu^{3+} species, represented by a sharp spot signifies Eu^{3+} species in homogenous environment, while the other spot that display Eu^{3+} species that is excited in a wide range of wavelengths, represent the Eu^{3+} species in an inhomogenous environment. The excitation wavelength maximum for the Eu^{3+} species represented by the sharp spots are at the wavelengths 579.4, 579.7 and 581.7 nm respectively with the increasing amount of Zr^{4+} ions in the nanocomposites. As the Eu^{3+} species in the NC-Ce100 nanocomposite is the most blue shifted, they are experiencing the weakest crystal field and might possibly be because of the removal of an O^{2-} ion from the NN position, resulting in probably the largest number of vacancies around the Eu^{3+}. The Eu^{3+} species from the NC-Zr100 sample' TLS with an excitation wavelength of 581.7 nm is the most red shifted, which suggests that it is experiencing the strongest crystal field in this sample. This may perhaps be attributed to smallest number of defects in the close vicinity of the Eu^{3+} ion in this sample.

5.2.4.1 Site selective excitation

The site selective emission spectra of the samples collected at four wavelengths for the nanocomposites annealed at 773 K and 1273 K (insets for each sample) for 2 h respectively, are displayed in Figure 20.

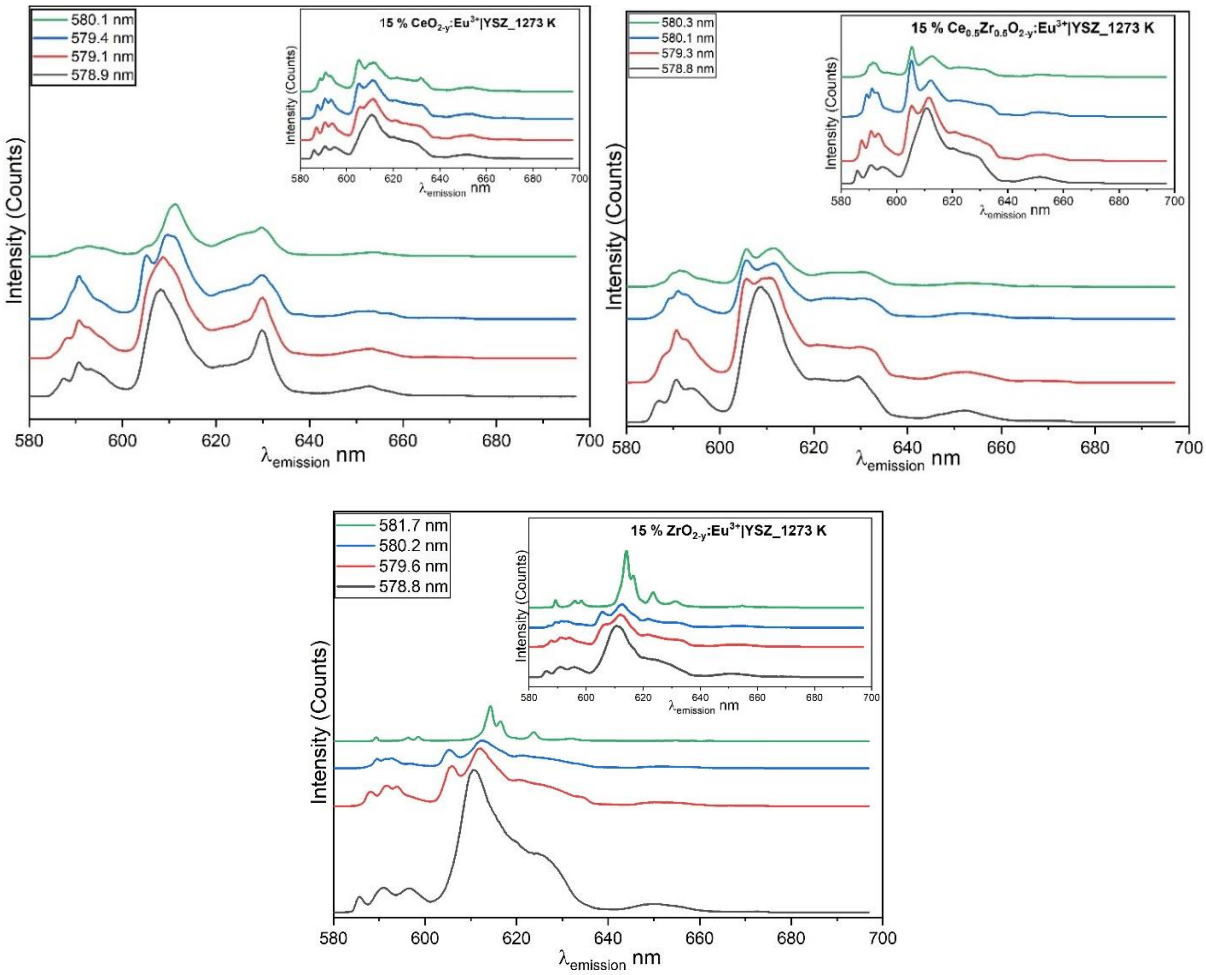

Figure 20. Emission spectra of NC-Ce100 (top left), NC-Ce50 (top right), NC-Zr100 (bottom left) and YSZ: Eu^{3+} (bottom right) annealed at 773 K after site selective excitation at the different wavelengths shown in figure. (T = 4 K). Spectra for 1273 K samples shown as insets.

The emission spectra collected at different excitation wavelength show only slight differences for each sample with respect to the Stark splitting, position and spectral width of the emission bands, despite the small differences in the excitation wavelengths. However, with 100 % zirconia in the nanocomposite, a more pronounced effect on the emission spectrum, pertaining to the wavelength of excitation of 581.7 nm is observed. Here, the emission peaks become sharper indicating that the Eu^{3+} ions are in a slightly different environments in the host lattice, with comparison to the others.

With the 773 K calcined nanocomposites, the $^5D_0$-$^7F_2$ transition ($\sim 601 < \lambda_{emission} < 635$ nm) dominates the spectra in all the three samples and the implication is that the probed Eu^{3+} ions are not in a site with

inversion symmetry symmetry[59,97]. Considering the Stark splitting in the magnetic and electric dipole transitions ($^5D_0$-^7F_J, J = 1, 2) as well as the fact, that the luminescence was excited via $^5D_0$-$^7F_0$ transition, the symmetry at the location of the Eu^{3+} ions is low and most likely to be among the point groups C_{2v}, C_S, C_2 and C_1, which are part of the cubic symmetry group. For the 1273 K heated nanocomposites, especially at low excitation wavelength (578.8 nm), peaks in the samples stay broad. As with the 773 K annealed nanocomposites, the $^5D_0$-$^7F_2$ transition dominates the spectra in the samples, which also suggest that the probed Eu^{3+} ions are not in a site with inversion symmetry [59,97].

In all the samples, the emission bands sharpen and the Stark splitting pattern becomes more resolved and pronounced, the higher the excitation wavelength (above 579 nm) to signify Eu^{3+} species in a more crystalline and homogenous environments. Also, as with the Eu^{3+} species in 1273 K annealed nanocomposite samples excited at low excitation wavelengths, they site in low symmetry location based on the Stark splitting in the magnetic and electric dipole transitions ($^5D_0$-^7F_J, J = 1, 2) and that the luminescence was excited via $^5D_0$-$^7F_0$ transition.

5.2.4.2 Longer delay after laser pulse TLS measurements

Measuring the emission and excitation of the Eu^{3+} ions in the nanocomposites at a longer delay of 5 ms after laser pulse (in comparison to measurement at a delay of 500ns in TLS (*vide supra*), results in the TLS shown in Figure 21. This information is useful to estimate the Eu^{3+} species that has the longest decay time.

As shown in the TLS, after 5 ms delay of laser pulse, only narrower and bright spots are observed and the implication is that the long lived Eu^{3+} species occupy more homogenous environments. They are maximally excited at 580.3, 580.6 and 581.8 nm with increasing the amount of Zr^{4+} ions in the nanocomposites.

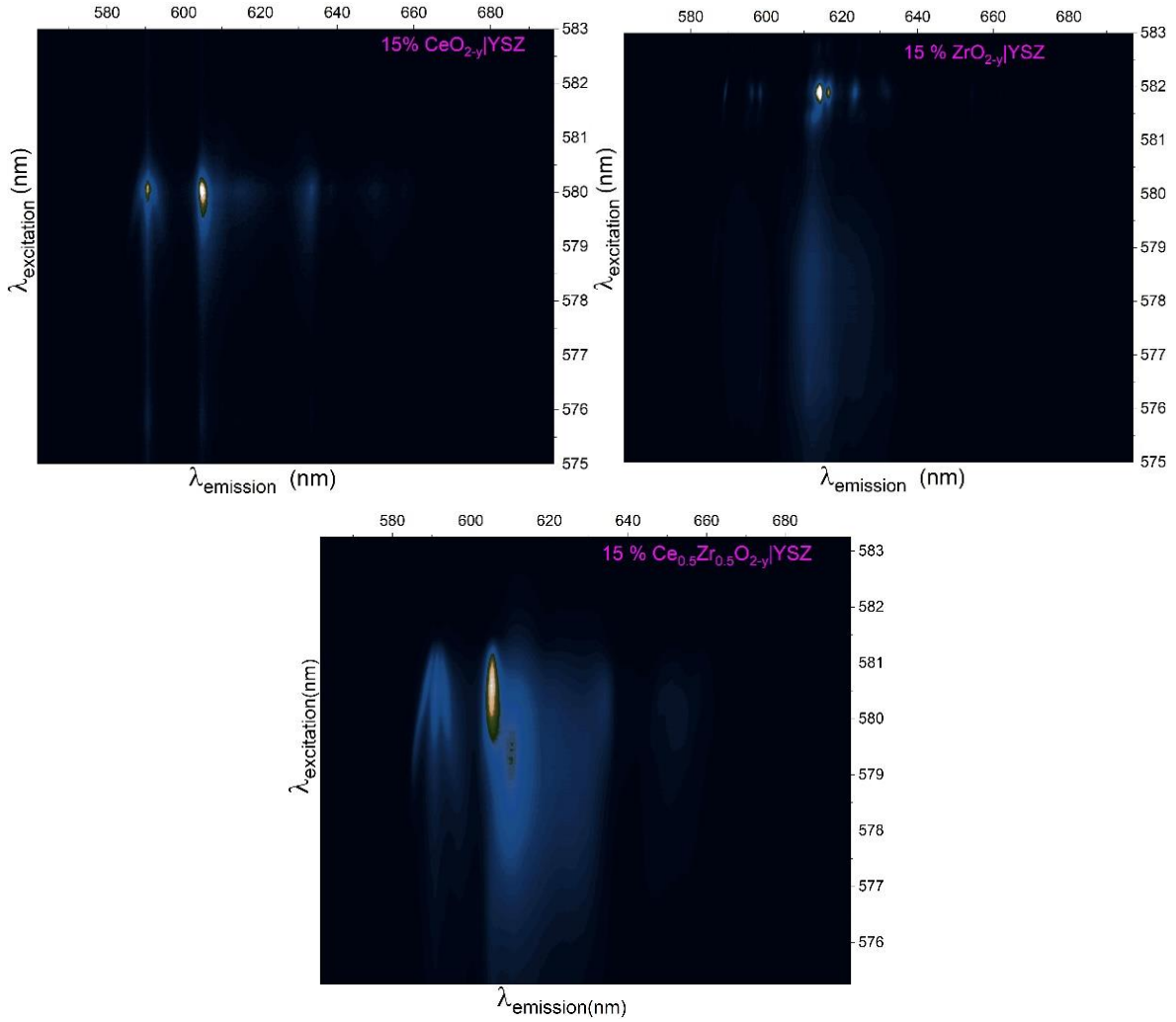

Figure 21. Total luminescence spectra (logarithmic intensity/color scale) of NC-Ce100 (top left), NC-Ce50 (bottom) and NC-Zr100 (top right) nanocomposites calcined at 1273 K for 2 h. The delay after laser pulse was 5 ms and T=4 K.

5.2.4.3 Time resolved measurements and PARAFAC Analysis

For a further evaluation of the species distributions in the nanocomposites, TLS at T = 4 K of 1273 K annealed NC-Ce100, NC-Ce50 and NC-Zr100 nanocomposites were recorded at four different initial delay times after the laser pulse (1 µs, 100 µs, 500 µs and 1000µs, respectively). A short gate width of 500 µs was used and the results processed in a PARAFAC analysis. The emission and excitation information were used to resolve the Eu^{3+} speciation in the samples as measuring the TLS after a longer delay of 5 ms did only yield information on the long-lived species in the samples.

In Figure 22, the results of the PARAFAC analysis for the three samples are shown. In comparison to species obtained after measuring the TLS at a delay of 5 ms and gate width of 1 ms (*vide supra*), more

Eu^{3+} species excited at different wavelengths were identified in the samples. On the right are the comparison site selective emission spectra from TLS before PARAFAC analysis was performed.

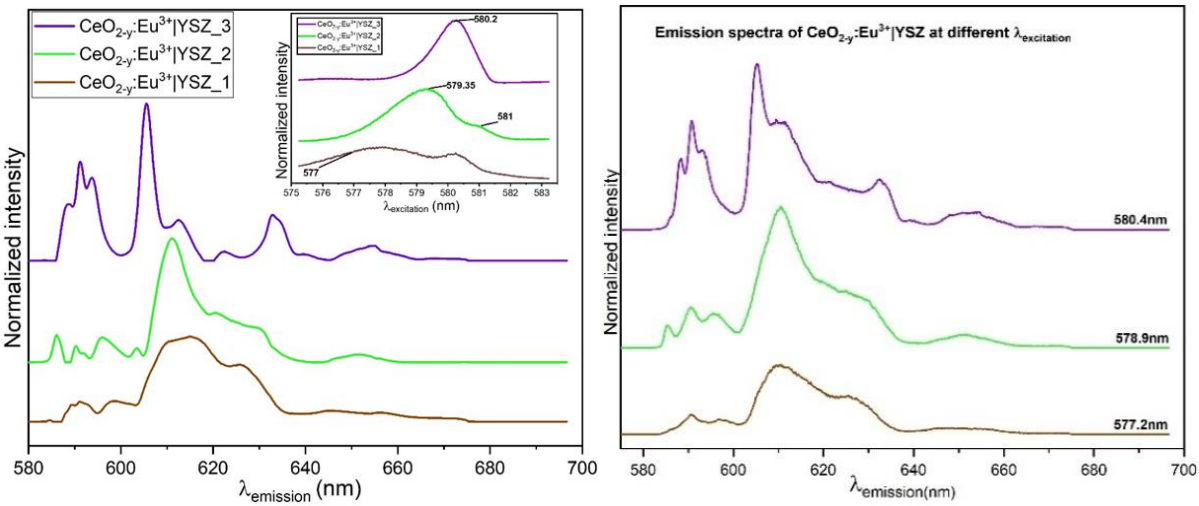

Figure 22. PARAFAC analysis emission and excitation spectra for NC-Ce100 as based on the TLS data (initial delay Δt_1 = 10 µs, Δt_2 = 100 µs, Δt_3 = 500 µs and Δt_4 = 1000 µs, respectively; T = 4 K) (left). Corresponding excitation spectra (inset) and site selective emission spectra from the TLS before PARAFAC analysis (right) are shown.

The results after PARAFAC analysis on NC-Ce100 spectroscopic data reveal three emission and excitation spectra to signify three Eu^{3+} species present in the sample. The emission spectrum in purple shows a "clean" Eu^{3+} signal, without contamination with additional signals from other Eu^{3+} species. The green and brown emission spectra are not fully deconvoluted as more than three peaks are visible in the $^7F_1$ transition, clearly showing "contamination". This is also supported by the fact that the green and brown excitation spectra have two peaks and that the brown spectrum is very broad. The possibility of the sample having more than three Eu^{3+} species is anticipated as it has been found that the TLS of a pure sample of CeO_{2-y}:Eu^{3+} nanoparticles annealed at 1273 K displayed up to seven Eu^{3+} species[21]. Figure 23 also supports the possibility of several species in a pure ceria nanocomposite sample.

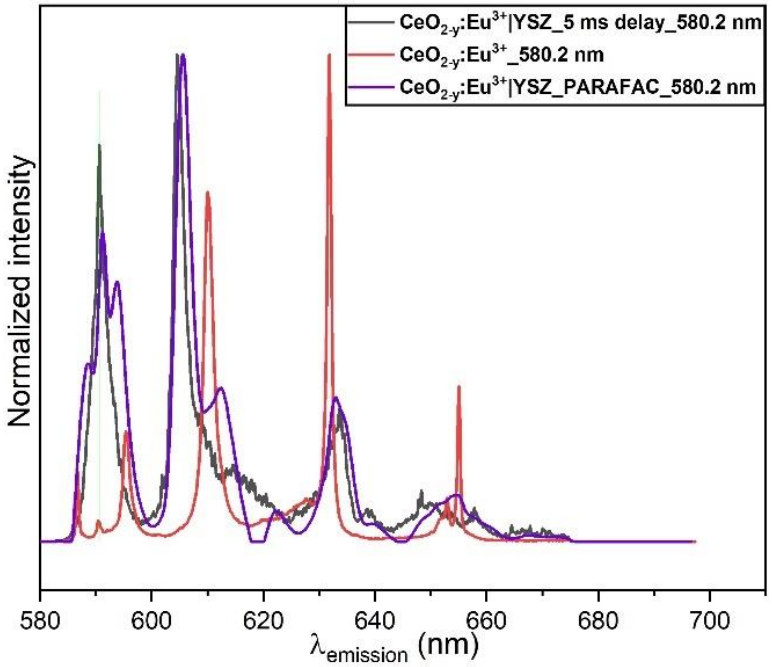

Figure 23. Emission spectra for NC-Ce100 after 5 ms delay of laser pulse, NC-Ce100 from PARAFAC analysis and that of YSZ unsupported CeO_{2-y}: Eu^{3+} taken at an excitation wavelength of 580.2 nm. Results based on TLS data at T = 4 K.

Figure 23 shows the comparison of the spectra of NC-Ce100 nanocomposite after 5 ms delay of laser pulse, YSZ unsupported CeO_{2-y}: Eu^{3+} nanoparticles and that of NC-Ce100 from PARAFAC analysis taken at an excitation wavelength of 580.2 nm. Although the $^5D_0$-$^7F_1$ splitting pattern in the three spectra is different, it is interesting to note that, the emission spectrum from NC-Ce100 nanocomposite recorded after a longer delay of laser pulse display what can be seen as "high" symmetry species (based on the peak at around 591 nm) as in unsupported CeO_{2-y}: Eu^{3+} nanoparticles. There is a possibility that the signals from this envisioned "high symmetry" species is contaminated by signals from other species and thus cannot be seen in the PARAFAC analysis result. The $^5D_0$-$^7F_2$ splitting pattern is similar, with the peaks slightly shifted in the three samples compared. The PARAFAC results for NC-Zr100 nanocomposite sample are shown in Figure 24.

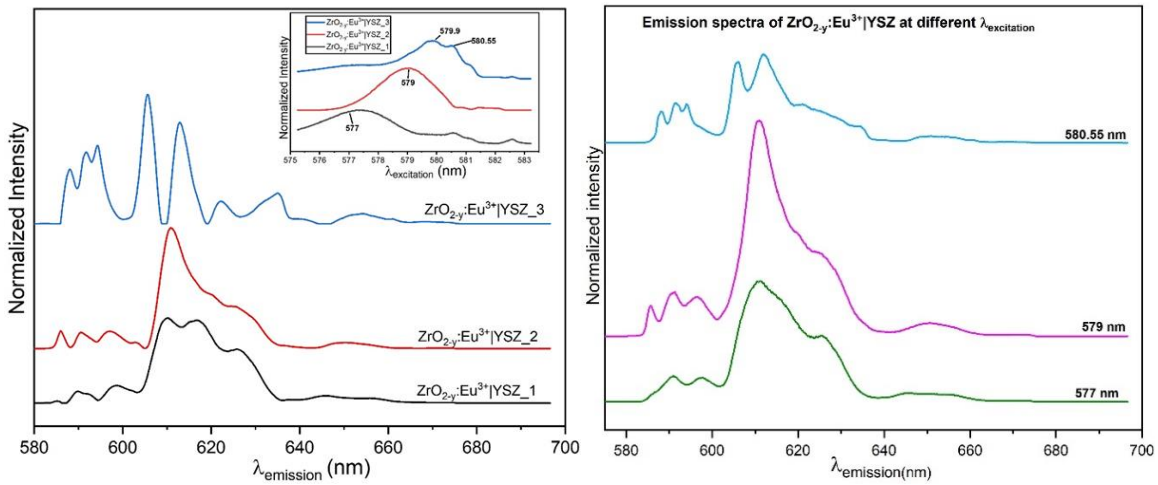

Figure 24. Emission and excitation spectra for NC-Zr100 as results of the PARAFAC analysis based on the TLS data (initial delay Δt_1 = 10 µs, Δt_2 = 100 µs, Δt_3 = 500 µs and Δt_4 = 1000 µs, respectively; T = 4 K). Corresponding excitation spectra (inset) and site selective emission spectra from the TLS before PARAFAC analysis (right) are shown.

As in NC-Ce100, there are the three emission and excitation spectra obtained after PARAFAC analysis of the NC-Zr100 sample. This implies the presence of three Eu^{3+} species, although there is a possibility of more than three Eu^{3+} species from the PARAFAC analysis. The excitation spectra support this fact (have several peaks in each spectrum). Finally, the spectra obtained from PARAFAC analysis of NC-Ce50 sample are shown in Figure 25. There are also three species obtained in this sample, though there could be more species as the scenario with the other samples. Similarly, to the NC-Ce100 sample, the red emission spectrum displays "clean" Eu^{3+} signal and the Stark splitting in the transitions shown are noticeable. The blue emission spectrum could be deconvoluted further, though the spectrum shows good $^5D_0$-$^7F_1$ splitting pattern. Also, the black spectrum is not fully deconvoluted as more than three peaks are visible in the $^5D_0$-$^7F_1$ transition and that the excitation spectra is very broad.

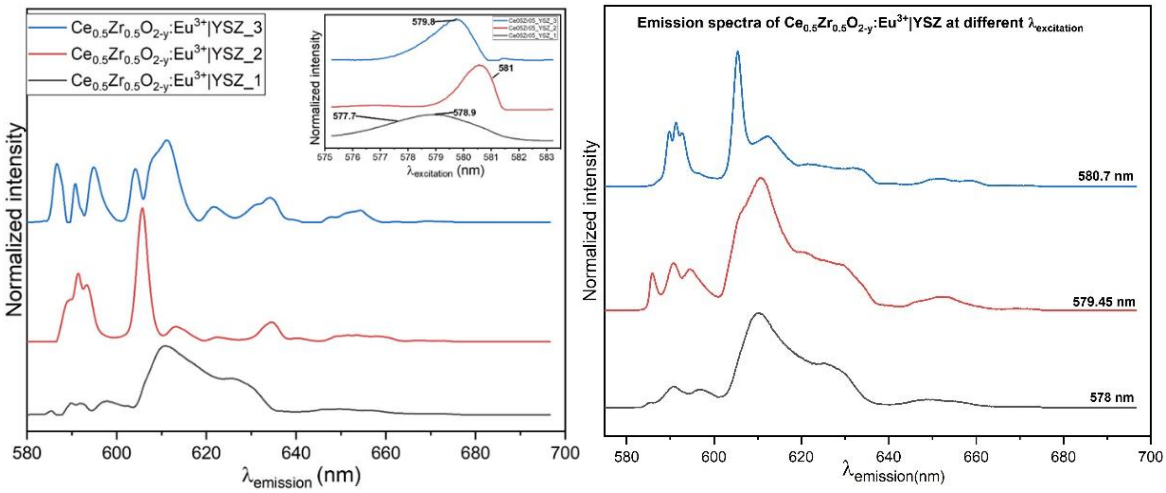

Figure 25. Emission and excitation spectra for NC-Ce50 as results of the PARAFAC analysis based on the TLS data (initial delayΔt_1 = 10 µs, Δt_2 = 100 µs, Δt_3 = 500 µs and Δt_4 = 1000 µs, respectively; T = 4 K). Corresponding excitation spectra (inset) and site selective emission spectra from the TLS before PARAFAC analysis are shown (right).

5.2.4.4 Second decay kinetics results

To further spectroscopically characterize the nanocomposites, more decay kinetic measurements were carried out and deconvolution of the data ensued. Time resolved measurements were done upon site selective excitation of the Eu^{3+} species at 4 K using a variable gate step; delay times used in the measurements were between 500 ns and 6 ms after laser pulse while a small gate width of 200 µs was maintained. A total of 200 time points was used. The wavelengths of excitation were obtained from excitation spectra from PARAFAC analysis (*vide supra*) where there was maximum excitation of one species and insignificant contribution from other species. Four excitation wavelengths for each sample were selected and used in the measurements. These results were deconvoluted by PARAFAC analysis to determine the decay times of the Eu^{3+} species in the nanocomposites excited at the wavelengths between 577 nm and 581 nm. Table 13 shows the excitation wavelengths used in the decay measurements.

Table 13: The excitation wavelengths used in the decay measurements of the NC-Ce100, NC-Zr100 and NC-Ce50 nanocomposite samples

Sample	Chosen $\lambda_{excitation}$ (nm)
15 % CeO_{2-y}: Eu^{3+}|YSZ	577, 579.35, 580.2, 581
15 % ZrO_{2-y}: Eu^{3+}|YSZ	577, 579, 579.9, 580.55
15 % $Ce_{0.5}Zr_{0.5}O_{2-y}$: Eu^{3+}|YSZ	577.7, 578.9, 579.8, 581

Deconvolution of the sample data in a PARAFAC analysis resulted in the emission spectra, decay curves (and decay times) and speciation diagrams. Figure 26 shows the decay curves (which were fit in a mono exponential function) for the Eu^{3+} species from PARAFAC analysis of NC-Ce100 (top left), NC-Zr100 (top right) and NC-Ce50 (bottom) nanocomposites respectively. The corresponding speciation diagrams (inset) are also shown.

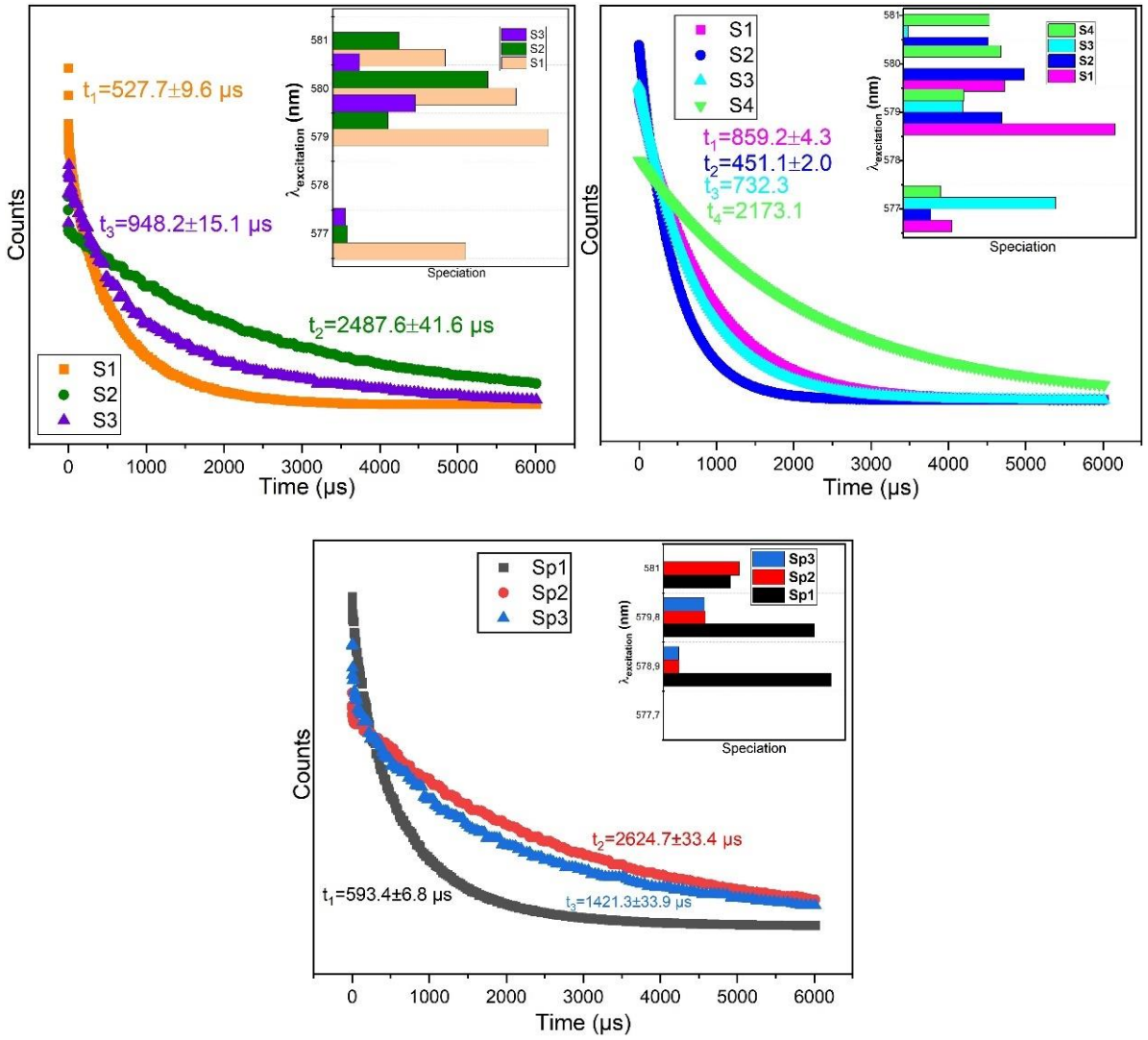

Figure 26. Decay curves (fit in a mono-exponential function) and speciation of the Eu^{3+} species found in 1273 K annealed NC-Ce100 (top left), NC-Zr100 (top right) and NC-Ce50 (bottom) samples. T= 4 K, $\lambda_{excitation}$ ranged from 577 nm, to 581 nm, variable delay from 500 ns to 6 ms, gate width = 200 µs.

For the nanocomposite NC-Ce100, PARAFAC results yielded three decay curves (Figure 26, top left) to show the presence of three Eu^{3+} species. From the speciation diagram, the species herein were maximally excited at 580.2 nm where there was also excitation of some species. This would result in the "contamination" of the emission signal from these species. This contamination is also an occurrence in the species excited at the other three different wavelengths. Regardless of the co- excitation of the

three Eu^{3+} species, which was inevitable, the average decay times of the species can be estimated as 530 μs, 950 μs and 2.5 ms.

The deconvolution results yielded four decay curves (Figure 26 top, right) to represent four Eu^{3+} species, for the NC-Zr100. The longest-lived species has a lifetime of ~ 2.1 ms, which is probably slightly exaggerated given that at an excitation wavelength of 580.55 nm, there is also excitation of the other species shown in the speciation diagram. The species represented by the Magenta decay curve is dominant at 579 nm according to the speciation diagram, where there is also excitation of the other Eu^{3+} species represented by the grey, blue and green. It is worth noting that although that the co-excitation of the different species was by no means unavoidable, sensible average decay times of the species were obtained.

Finally, Figure 26, bottom left shows three decay curves as the product after the decay kinetics and the deconvolution of the time resolved spectroscopy data for the NC-Ce50 sample, which means that there are three Eu^{3+} species. As has been observed with the other earlier nanocomposites, "contamination" with some additional signal from other Eu^{3+} species is inevitable, but despite these scenarios, average decay times for the three species were obtained which were 590 μs, 1.4 ms and 2.6 ms for the longest-lived species.

5.2.5 Temperature programmed reduction (TPR)

The extent of reducibility of the nanocomposites containing ceria was investigated since there is an existing relationship between redox properties and catalytic performance in ceria-based materials. Figure 27 shows the TPR results from the study of the YSZ supported oxides. Specifically, it reports the trace m/c =18, which corresponds to water.

Although the nanocomposites contain a high amount of zirconia, there was no reduction for pure ZrO_2 that was observed as no peak above 1273 K was observed, where the reduction of Zr^{4+} occurs[185]. The reduction of the mixed oxides in the nanocomposites showed low temperature peaks at ~ 583 K and at ~ 745 K and a high temperature peak at ~ 1013 K. Although they studied CeZr mixed oxides, Wang et al. attested to a low-temperature reduction peak which is in line with our results (~ 745 K) and they suggested that this would be due to highly dispersed ceria species[185].

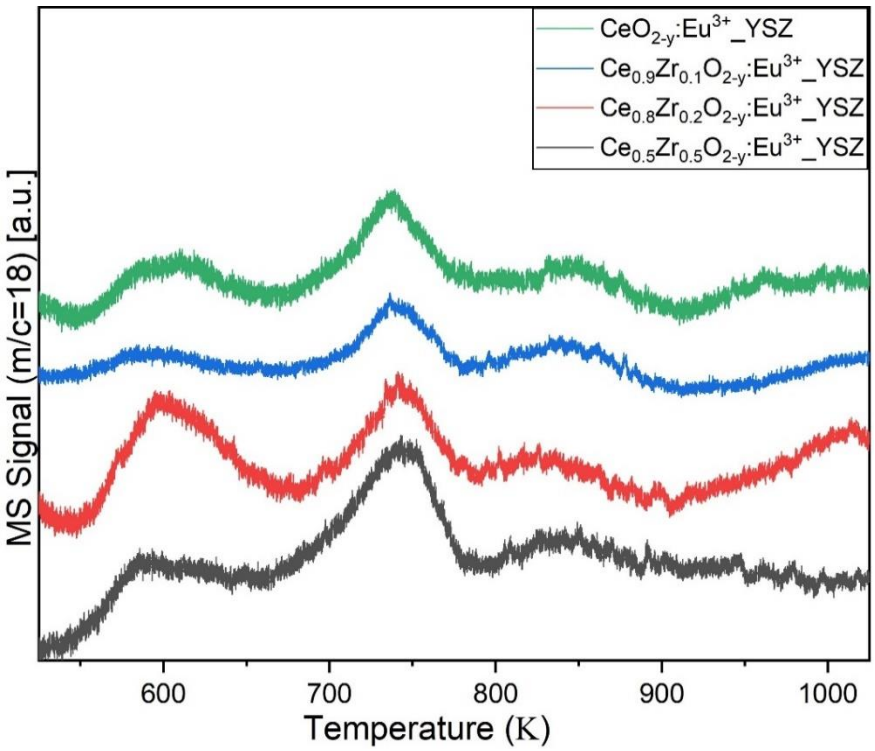

Figure 27. Traces for H_2O (m/c = 18) corresponding to the TPR-MS study of YSZ supported pure CeO_2 and CeZr mixed oxides.

The signal at around 843 K was attributed to the release of O^{2-} close to the surface[21,186], which would result in the formation of oxygen vacancies that can enhance ionic conductivity in CeO_2, while the high temperature band at around 1013 K would be due to a bulk reduction of ceria[20]. The nanocomposite with the 50/50 ratio of Ce/Zr impregnated on the surface of YSZ in the mixed oxide, NC-Ce50, has no reduction peak at high temperature (around 1013 K). Overall, there are slight shifts that are observed in the H_2-TPR reduction peaks and this is ascribed to the different amounts of ceria in the samples, which results in some slight changes in the crystal structure, and possibly the catalytic activities.

5.3 Conclusion

The nanocomposites; 15 % $Ce_xZr_{1-x}O_{2-y}$: Eu^{3+}|YSZ (X=0, 0.5 and 1) were synthesized by an incipient wetness impregnation method and thereafter annealed separately at 773 and 1273 K for 2 h. Some structural changes were determined by XRD, Raman and high-resolution STEM. Also, through spectroscopy measurements, the evolution of the emission patterns from specific Eu^{3+} lattice sites to indicate structural changes, thus effectively complementing the data obtained by the earlier techniques was observed. The nanocomposite samples annealed at 773 K displayed amorphous, unordered domains characterized by excitation of Eu^{3+} species in a broad range of excitation wavelengths.

The TLS of the 1273 K annealed nanocomposites reveal two distinct sites and the Eu^{3+} species from NC-Zr100 were excited at higher wavelengths than in the other two samples. Recording the

luminescence of the Eu^{3+} ions at a longer delay after laser pulse gave information regarding the longest-lived species. The results obtained from the high-resolution emission spectroscopy data were deconvoluted by PARAFAC analysis to facilitate the gathering of speciation information on the Eu^{3+} sites in the nanocomposites by identifying the amount and nature of lattice sites occupied by Eu^{3+} ions. However, due to the nature of the samples, it is a challenging task to separate the Eu^{3+} species completely as there is evolution of a variety of slightly different dopant sites which could be taken as contamination of Eu^{3+} ions signal from other different sites.

Overall, three different sites that can be occupied by Eu^{3+} ions in the crystal structure of the ceria containing nanocomposites and four for pure zirconia on the support, were observed and it can be concluded that temperature pretreatment before spectroscopy measurements play a crucial role in the distribution of trivalent europium over the different lattice sites. It is also a possibility that there are more sites occupied by the Eu^{3+} ions in the nanocomposite samples, which is reported for a pure ceria sample from literature. Thus, the combination of high-resolution emission spectroscopy and PARAFAC approach provides a framework for more detailed analysis for enhanced understanding of the effect of the amount of Eu^{3+} -doped ceria/zirconia on YSZ and the post temperature treatment after synthesis of supported novel nanocomposites on physical properties. Finally, the reducibility of the samples on a basis of the relationship existing between redox properties and catalytic behavior in ceria-based materials was investigated. The H_2-TPR results showed slight variations in the reduction peaks for the different amounts of ceria in the nanocomposites.

Chapter 6: Ceria nanomaterials containing ytterbium-low and high concentration - luminescence analyzed in the near infrared region

6.1 Introduction

CeO_2, is one of the most important materials in industrial applications; in solid oxide fuel cells, in biomedical applications and as heterogeneous catalysts[1,17,105,187]. Modifying the structure of pure CeO_2 through doping (or mixing) with lanthanide ions (Ln^{3+}) or tetravalent ions, increases its lattice oxygen mobility. This in turn increases the redox properties of the oxide[7,31]. CeO_2 can be easily altered by doping with other rare-earth ions for example Yb^{3+}, because of their comparable ionic radii. Yb^{3+} has an ionic radius of 0.0985 nm which is close to that of Ce^{3+} (0.0970 nm) and Ce^{4+} (0.1143 nm)[17,84]. During the modification process of the crystal lattice, the incorporation of the Yb^{3+} or other lanthanides ions results in the Ce^{4+} ions substitution[1]. The consequence is an introduction of one charge-compensating oxygen vacancy for every two trivalent dopants, resulting in multifaceted arrangements between Ce^{4+}, Ln^{3+}, O^{2-} and oxygen vacancies[19,30,31].

Yb^{3+} doped in nanomaterials find many applications such as sensitizer in up-conversion and also as luminescence probe showing near infra-red (NIR) emission. Like other Ln^{3+} ions, Yb^{3+} can exhibit sharp luminescence emissions via intra-4f or 4f-5d transitions[107]. Taking advantage of this noble property, Yb^{3+} doped nanomaterials are an integral part of many applications, for example in lasers[5,27,106,109]. With Yb^{3+} doping, highly desired imaging in NIR is enabled which is otherwise hardly possible with other materials[1]

The preferred oxidation state of ytterbium is +III (f^{13}), but the +II (f^{14}) can also be formed. Depending on its oxidation state f-f transitions or f-d-transitions can be observed. Yb^{3+} ions can be found in different symmetries, for example during formation of crystals, some of the Yb^{3+} ions substitute for the Ce ions and situate themselves in cubic (O_h), tetragonal (C_{4v}) and trigonal C_{3v} environments. These three sites can be accurately detected optically and only at very low dopant concentrations as there are no complex centers and defects in the lattices, which occur as a result of aggregates of Yb^{3+} ions when they are in high concentrations[26]. Thus, in high concentrations, an exclusive type of Yb^{3+} luminescent center is formed which dominate over all the sites.

Distinct Yb^{3+} ion has the electronic ground and excited states assigned to the $^2F_{7/2}$ and $^2F_{5/2}$ state, respectively[2,25]. Depending on the crystal field, these can be further split into Stark level multiplets. At a low C_S symmetry, the ground state $^2F_{7/2}$ can split into four and the excited state $^2F_{5/2}$ into three Kramer's doublets[2,4,26,109,110]. Thus, the transitions between the splitting levels are sensitive to the lattice site environment and also to the thermal vibration of crystal lattice occurring at room temperature and that thermal processes play a crucial part on the optical properties of the system.[2,5,108].

Trivalent rare-earth ions doped nanomaterials have a tendency to form clusters structure that contain at least two rare-earth ions in close environments and are luminescence quenching centers[26]. Also, an additional luminescence quenching process can occur as a result of internal defects inside a lanthanide oxide lattice, such as CeO_2, when Yb^{3+} are available in the lattice at high concentrations[1]. Yb^{3+} clusters can likewise act as trapping centers resulting in a fast-non-radiative decay from Yb^{3+} ion clusters[35,83]. Annealing nanoparticles containing Yb^{3+} ions results in improved crystalline structure and to a greater extent eliminates quenching centers resulting in intensification of high temperature annealed samples' NIR emission[27].

UC emission has been used to track Yb^{3+} distribution in a ceria lattice incorporated with other lanthanide ions and corroborate the data from XRD and Raman on the formation of homogenous solid solutions[35]. In these materials, the down conversion luminescence of Yb^{3+} is seldom examined. Only the luminescence of the activator ions (Er^{3+}, Tm^{3+} or Ho^{3+}) are detected. Nevertheless, in this work, the effect of Yb^{3+} ions in ceria-based $Ce_{1-x}Yb_xO_2$ mixed oxides clustering on its luminescence was investigated. In using Yb^{3+} concentration and annealing as "tools" to do this, firstly, the dependence of Yb^{3+} on the concentration of only Yb^{3+} ions in the host and secondly, the effect of annealing the nanomaterials at two different temperatures on the luminescence were examined. In addition, the effect of room temperature and 4 K (cryogenic conditions) modes of measurement on the luminescence properties of Yb^{3+} in samples were studied. The goal was the observation of possible changes in luminescence properties of the nanoparticles when the oxides are heated at elevated temperatures and measured at distinct temperatures.

6.2 Characterization of the Yb^{3+} containing ceria nanomaterials

6.2.1 TEM results for as synthesized $Ce_{1-x}Yb_xO_2$ (x=0.004, 0.01, 0.15 and 0.18) nanomaterials

The morphology of the as-synthesized nanomaterials was analyzed by TEM. TEM micrographs for CeO_2:Yb^{3+} are shown in Figure 28. The micrographs display nano-sized single particles, highly monodisperse, which are spherical in shape. With the increase of the Yb^{3+} concentration, the sizes of the nanoparticles as calculated using the ImageJ software, decrease only slightly. The TEM images for $Ce_{1-x}Yb_xO_2$ (x=0.03 and 0.05) are shown in the Appendix, Figure 50.

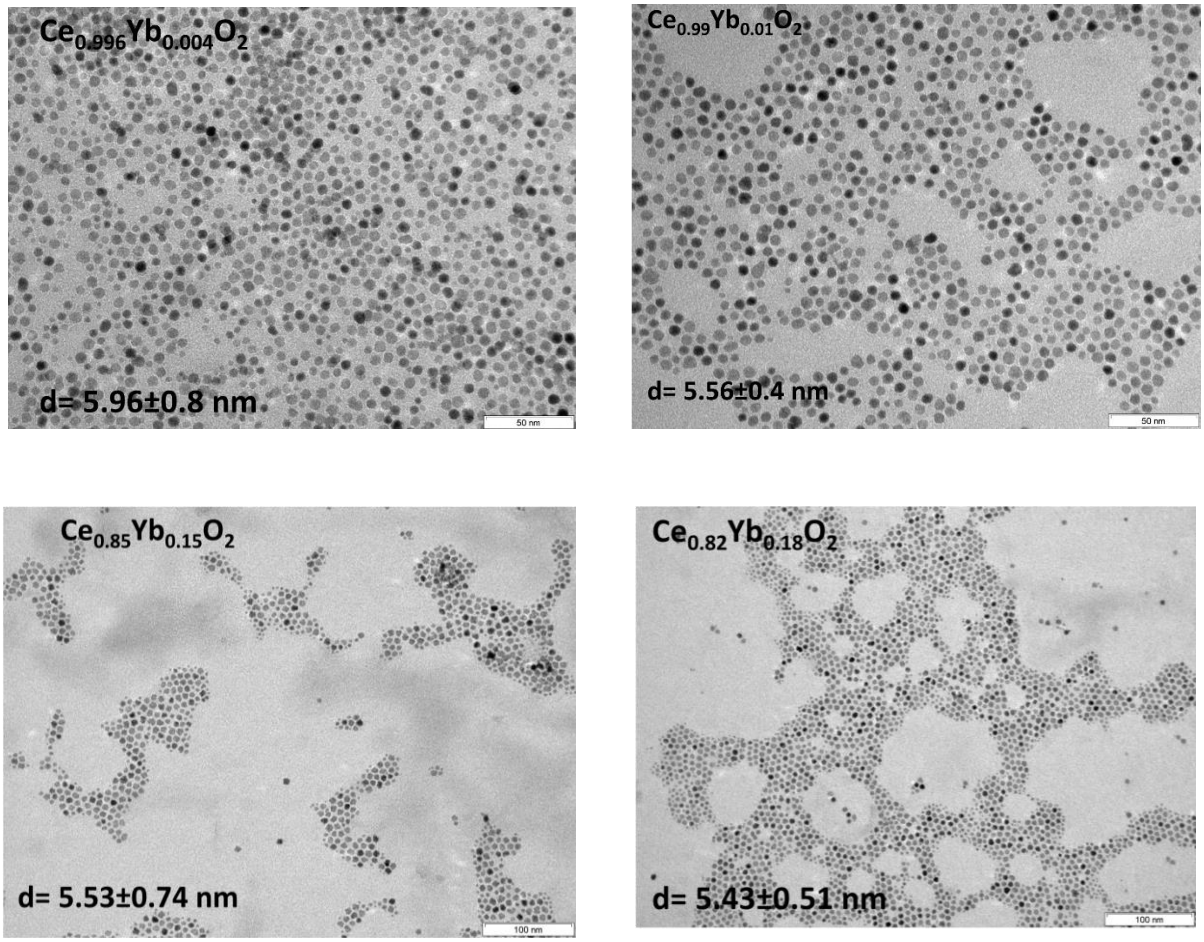

Figure 28. TEM micrographs for $Ce_{1-x}Yb_xO_2$ (x=0.004, 0.01, 0.15 and 0.18) nanomaterials.

6.2.2 XRD

Figure 29 shows the x-ray diffraction patterns of low concentration Yb^{3+}-ceria (set 1, left) and high concentration Yb^{3+}-ceria samples (set 2, right) annealed at T = 773 K and 1273 K, respectively. For all samples of set 1 and set 2 six diffraction peaks are observed. The results, obtained after calculation using the Debye Scherrer equation (equation 3) in Table 14, show that the crystallite size decreased inversely with the Yb^{3+} concentration in the samples. Additionally, a minor shift to lower 2θ values of the peak from 28.57º for $Ce_{0.996}Yb_{0.004}O_2$ sample with the increase in Yb^{3+} concentration is observed. For T =773 K, broader peaks are found indicating a small crystallite size in these samples. In contrast, the diffraction peaks at T = 1273 K annealed samples show much narrow and sharper peaks and this is due to an increase in crystallite size. As an example, for the lowest Yb^{3+}-ceria nanoparticles, the value of FWHM for the first peak decreased by a factor of five from 0.73 to 0.14 after annealing the powder from 773 K to 1273 K. Also, for the highest Yb^{3+} ions in the mixed oxide powders, the value for the FWHM decreased by a factor of four from 0.74 to 0.18 after the same heat treatment (see Table 14).

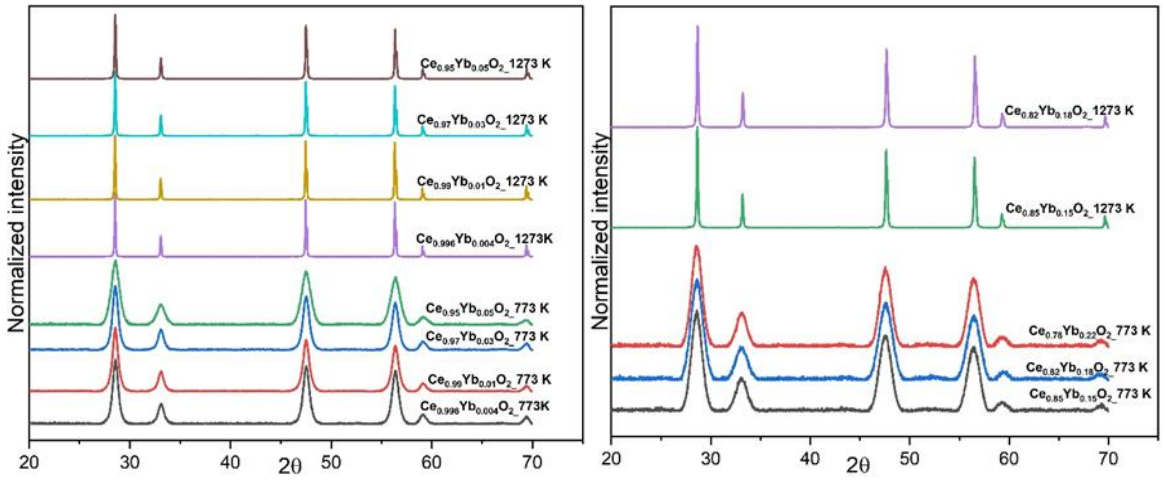

Figure 29. XRD patterns of the 773 K and 1273 K annealed $Ce_{1-x}Yb_xO_2$ (x=0.15, 0.18 and 0.22). Cu-K_α radiation (λ= 1.54187 Å).

Moreover, an increase in annealing temperature to 1273 K caused a substantial increase in crystallite size, suggesting a better atomic arrangement in the crystal lattice. Although all the powders annealed at 1273 K were well crystallized (Figure 29), there was no appearance of any peaks related to isolated Yb^{3+} phases. Diffraction peak positions of all samples match with standard diffraction positions of cubic fluorite CeO_2: Yb (standard card PDF 98-018-2971). Based on the Scherer equation, the crystallite size of the nanomaterials decreased by 33 % comparing nanomaterials with low and high Yb^{3+} concentration (as shown in Table 14). With the increase in calcination temperature to 1273 K, the diffraction patterns slightly moved toward the higher 2θ values, which is in accordance with reports on the same nanomaterials synthesized by Florea et al[30]**.**

The lattice parameter of the lowest Yb^{3+} concentration (0.4 mol %) was calculated to be 0.5416 nm, but it varied from 0.5417 nm (for 1 mol % Yb-ceria) to 0.5412 nm (for 5 mol % Yb-ceria), see Table 14. The difference in the lattice parameter shift can be directly related to the ionic radii of the dopant as compared to the host. The results are consistent with that observed by Babu et al. and supports that doping smaller trivalent ions e.g. Yb^{3+} (ionic radius 0.0985 nm) in ceria results in its lattice contraction, although the extent of the lattice parameter changes with the concentration of the trivalent dopant ion[80]. There is a slight decrease in lattice parameter by introducing more Yb^{3+} ions in the host ion. However, Matović et al. observed an increase in the lattice parameters from a Yb^{3+} ions doping concentration range of 5 % to 20 % [17].

Table 14. Crystallite size and lattice parameter of the CeO_2: Yb^{3+} nanomaterials at the two annealing temperatures with increasing Yb^{3+}concentration.

Sample	**Crystallite Size (nm)**		**Peak position (º)**		**FWHM (º)**		**Lattice parameter (nm)**
Annealing temperature	773K	1273 K	773 K	1273 K	773 K	1273 K	
$Ce_{0.996}Yb_{0.004}O_2$	12.4±0.2	78.7±2.3	28.57±1.2E-3	28.54±6.1E-4	0.73±0.0029	0.14±0.0015	0.5416±1.8E-4
$Ce_{0.99}Yb_{0.01}O_2$	12.5±0.2	71.6±1.8	28.60±2.0E-3	28.53±6.4E-4	1.42±0.0048	0.15±0.0015	0.5417±1.8E-4
$Ce_{0.97}Yb_{0.03}O_2$	12.4±0.2	40.5±1.0	28.56±9.5E-4	28.55±5.4E-4	0.73±0.0023	0.16±0.0013	0.5414±2.5E-4
$Ce_{0.95}Yb_{0.05}O_2$	9.4±0.2	36.7±0.7	28.56±1.4E-3	28.55±5.1E-4	1.02±0.0033	0.17±0.0012	0.5412±2.1E-4
$Ce_{0.85}Yb_{0.15}O_2$	8.0±0.3	40.7±0.6	28.58±1.7E-3	28.65±3.3E-4	1.29±0.0041	0.18±7.7E-4	
$Ce_{0.82}Yb_{0.18}O_2$	7.6±0.3	40.0±0.6	28.55±1.1E-3	28.67±3.1E-4	0.74±0.0026	0.18±7.4E-4	
$Ce_{0.78}Yb_{0.22}O_2$	8.0±0.2	-	28.59±1.6E-3	-	1.24±3.7E-3	-	

Expected trends are shown by the samples: amplified agglomeration of the crystallites due to annealing at higher temperature and also the crystallinity of the samples is increased. This is demonstrated by the increase in the crystallite size with annealing at 1273 K for 2 h and also corroborated by the morphology results from SEM examinations (*vide infra*). On the other hand, no (significant) differences between set 1 and set 2 are found in XRD patterns, which would indicate that no additional phase due to high Yb^{3+} ions content is formed. Based on XRD no indication of clustering can be seen.

6.2.3 Raman spectroscopy

Raman data to determine the anion ordering in the samples were also collected supplementary to XRD data. Figure 30 shows the Raman spectra of 773 K annealed ceria nanomaterials with increasing Yb^{3+} concentration from 0.4 to 22 mol %. Four vibrational modes are observed in the Raman spectra of Yb^{3+} containing samples. These are around 268, 464, 560, and 610 cm^{-1}. The prominent peak at 464 cm^{-1} corresponds to the triply degenerate F_2g Raman active mode of the fluorite structure. It is viewed as a symmetric breathing mode of the oxygen atoms around cerium ions[19]. This peak is slightly blue shifted and becomes progressively wider (see FWHM in Table 15) and asymmetric with an increase in Yb^{3+} concentration.

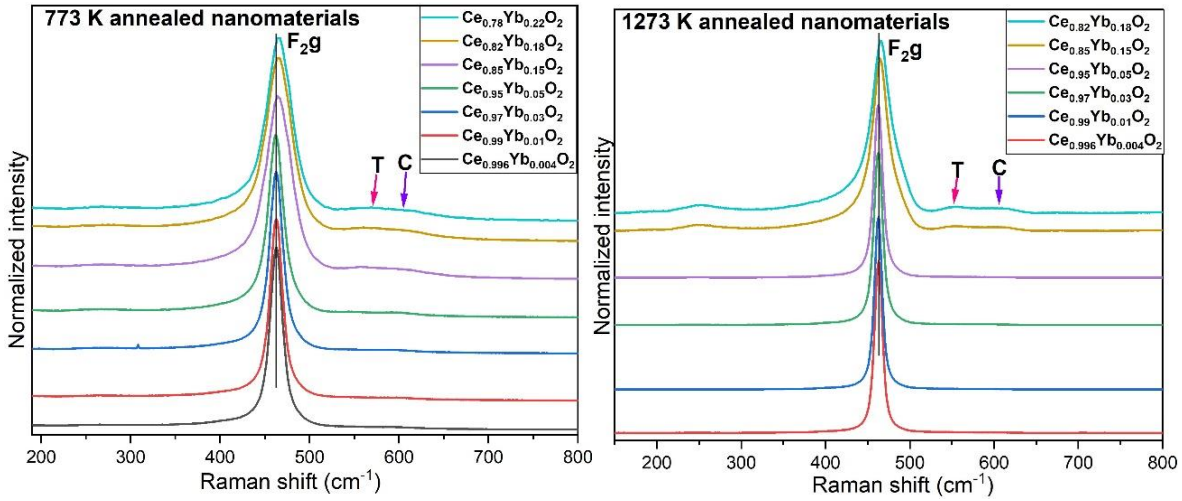

Figure 30. Raman spectra of ceria nanomaterials (annealed at 773 K- left and annealed at 1273 K- right) with increasing Yb^{3+} concentration from 0.04 to 22 mol %. (λ_{Laser} = 633 nm).

The intensity of two more modes that appear around 560 and 610 cm^{-1} (referred to as T and C respectively) intensify with Yb^{3+} amount in the samples. These defect modes are assigned to extrinsic vacancies induced by Yb^{3+} doping and Ce^{3+} (to loosening of symmetry rules), respectively[105]. Resulting from these defects, a substantial amount of oxygen vacancies via charge - compensation mechanism is introduced in the materials as the amount of Yb^{3+} increases as also reported by Florea et al[30] . A very weak Raman mode around 268 cm^{-1} can be seen for the sample with highest Yb^{3+} content (15, 18 and 22 mol %) heated at 773 K. Annealing at 1273 K intensifies this peak and result in the red shift of this mode to around 250 cm^{-1}.

As shown in Table 14, annealing the nanomaterials at 1273 K for 2 h promotes the increase in the crystalline size. This might also lead to the noticeable decrease in the FWHM of the F_2g peak of the Raman spectra with annealing temperature, as shown in Table 15. A slight blue shift in the F_{2g} peak is also observed with the increase in the annealing temperature.

Table 15. Yb^{3+} doping and annealing temperature effect on the F_2g Raman mode of CeO_2.

Sample	FWHM (cm^{-1})	
Annealing temperature	773K	1273 K
$Ce_{0.996}Yb_{0.004}O_2$	20.53± 0.19	12.77± 0.09
$Ce_{0.99}Yb_{0.01}O_2$	20.63± 0.20	12.42± 0.10
$Ce_{0.97}Yb_{0.03}O_2$	22.30± 0.22	14.40± 0.11
$Ce_{0.95}Yb_{0.05}O_2$	26.58± 0.30	14.40± 0.11
$Ce_{0.85}Yb_{0.15}O_2$	41.96± 0.58	31.95± 0.37
$Ce_{0.82}Yb_{0.18}O_2$	42.00± 1.2E-13	36.72± 0.43
$Ce_{0.78}Yb_{0.22}O_2$	41.20± 0.59	-

6.2.4 Scanning electron microscopy (SEM)

The topography of the nanomaterials was analyzed by SEM. In Figure 31, micrographs of $Ce_{1-x}Yb_xO_2$ powders calcined at two different temperatures are presented (773 K annealed (left column) and 1273 K annealed (right column). The SEM micrographs for 773 K annealed Yb^{3+} -ceria samples display that the nanomaterials have an irregular shape, has fissures and rough surface. The microstructural observation of the 1273 K annealed powder with low Yb^{3+} composition shows distinct agglomeration of individual crystals (especially seen with low Yb^{3+} ions containing samples where the resolution is higher in the images). The micrographs established in some parts that there is formation of clean grains with distinct grain boundaries, to demonstrate that the grains are roughly equiaxial and condensed (can be clearly seen in the 1273 K annealed $Ce_{0.996}Yb_{0.004}O_2$ sample. With higher Yb^{3+} concentration, the surface becomes smoother and the fissures becomes less distinct, especially with high annealing temperature.

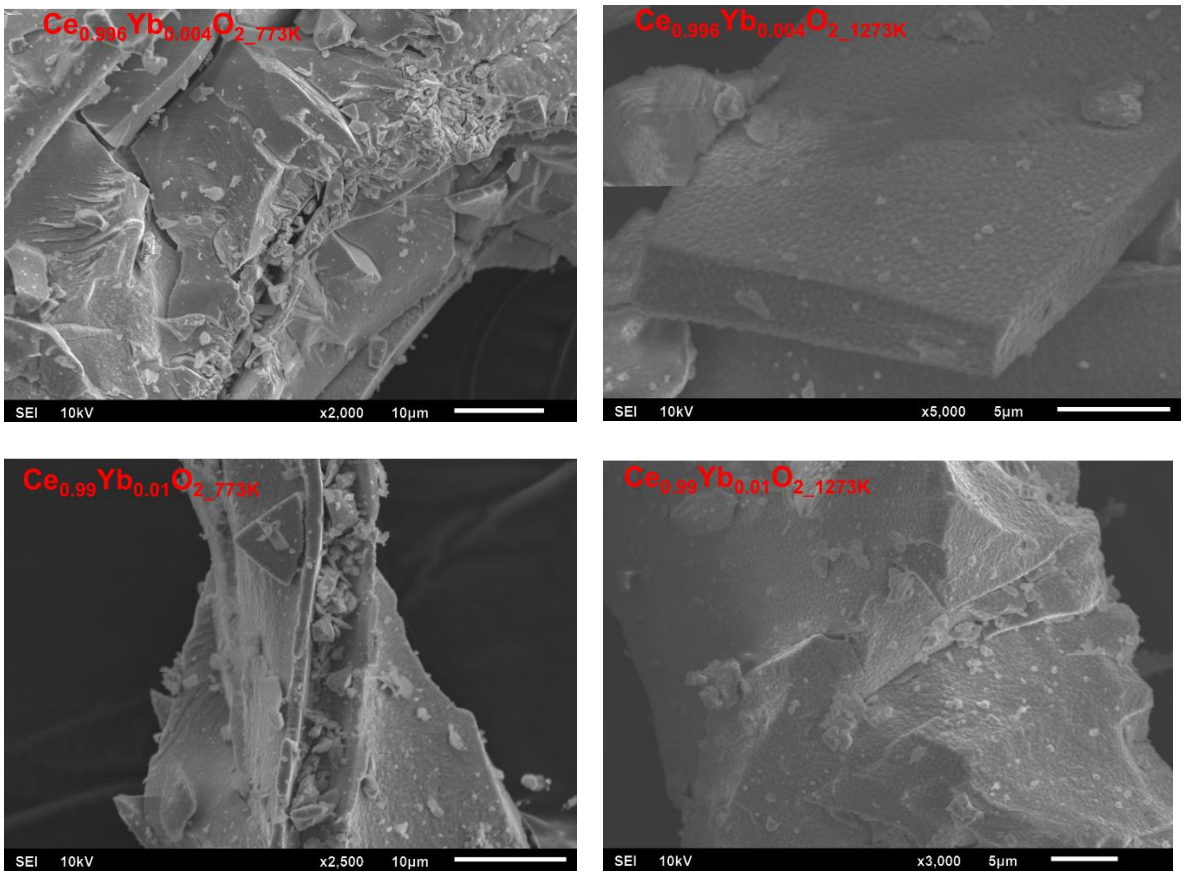

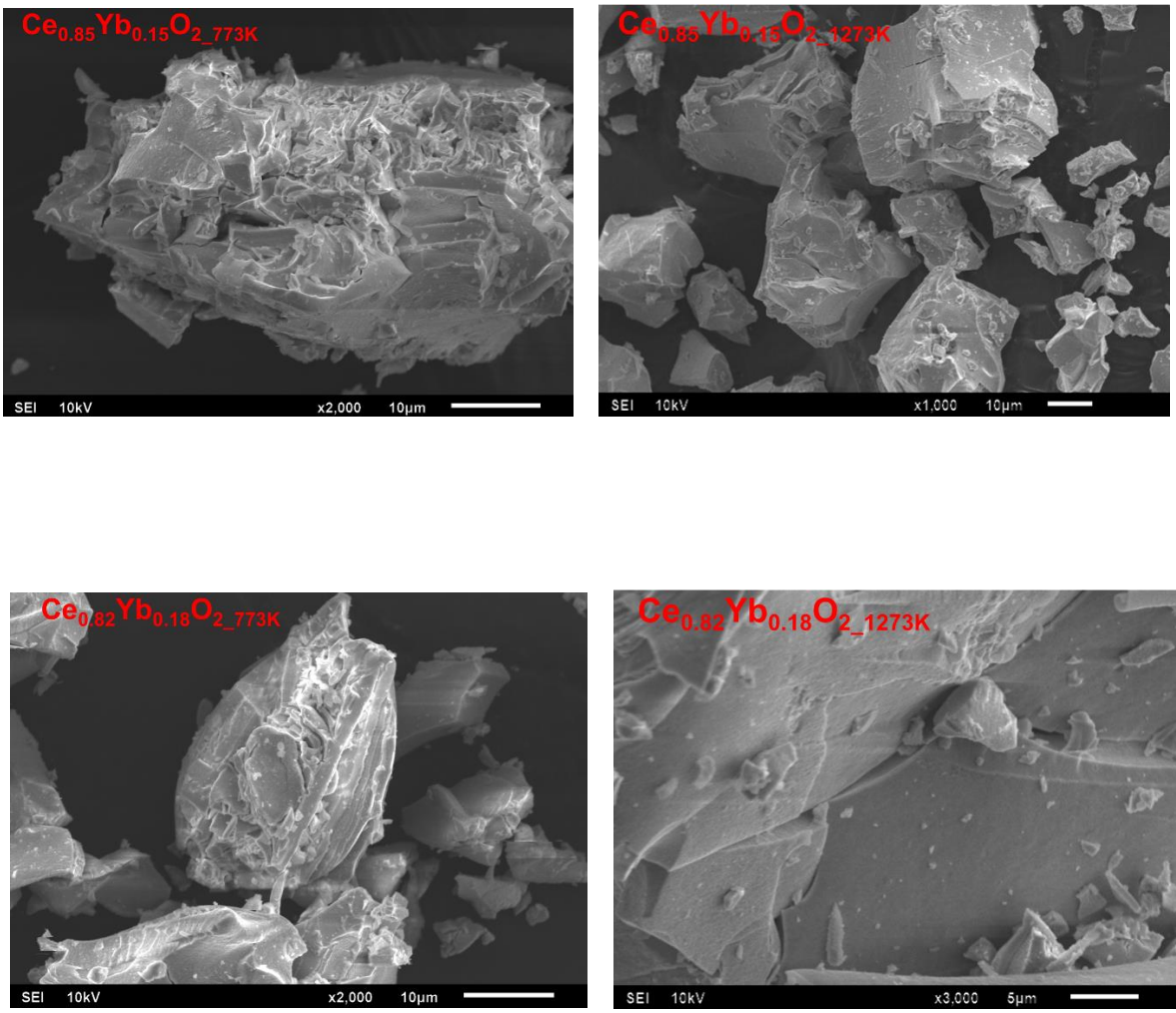

Figure 31. SEM micrographs of $Ce_{1-x}Yb_xO_2$ powders calcined at 773 K (left column) and 1273 K (right column).

6.2.5 Elemental analysis

Elemental analysis was done to approximately determine the compositions of the elements in the samples and the results are shown, for two of the samples annealed at 1273 K in Figure 32. The EDX spectrum obtained indicate the molar ratio between each element. The ratio is nearly consistent with the nominal composition. Only cerium, oxygen and the expected ytterbium dopant are detectable in the EDX spectra. No contaminants were observed in the EDX spectra.

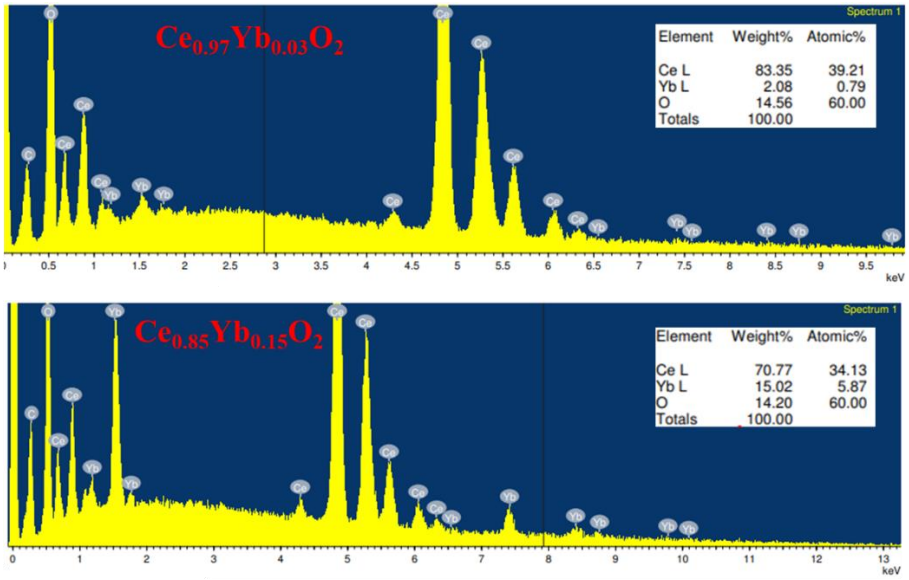

Figure 32. EDX spectrum and elemental composition chart for $Ce_{0.97}Yb_{0.03}O_2$ and $Ce_{0.85}Yb_{0.15}O_2$ annealed at 1273 K.

6.2.6 Elemental mapping

Figure 33 shows the elemental maps from the $Ce_{1-x}Yb_xO_2$ ($0.004<x<0.18$) nanomaterials. The maps display homogenous distribution of the ytterbium atoms in the ceria matrix in all the samples where Yb^{3+} is doped in ceria and heated at 773 K for 2 h.

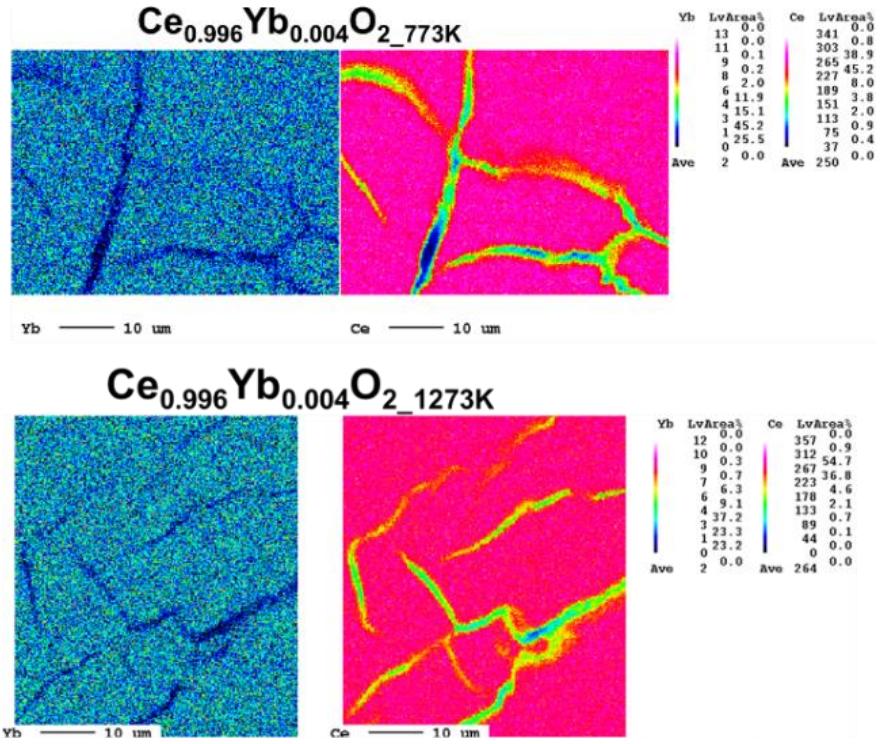

$Ce_{0.97}Yb_{0.03}O_{2\_773K}$

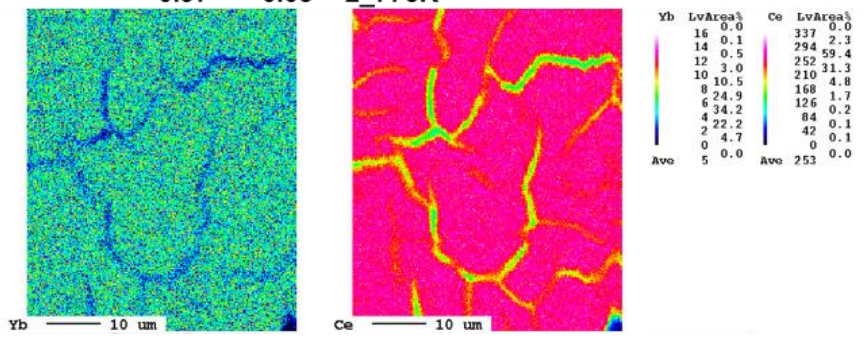

$Ce_{0.97}Yb_{0.03}O_{2\_1273K}$

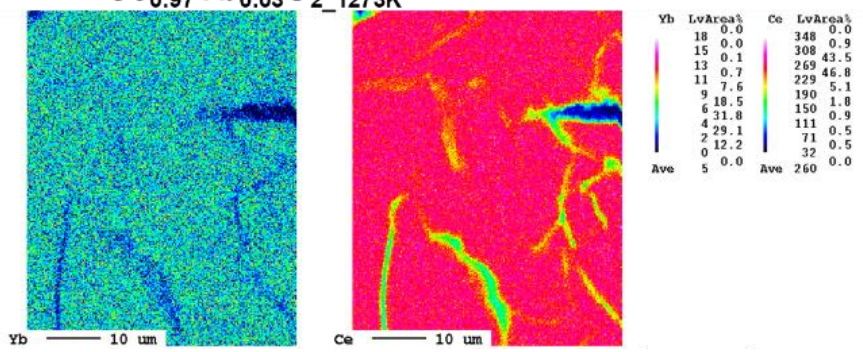

$Ce_{0.85}Yb_{0.15}O_{2\_773K}$

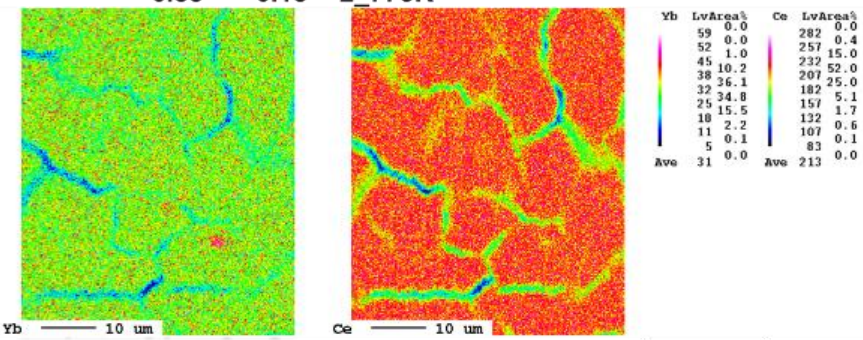

$Ce_{0.85}Yb_{0.15}O_{2\_1273K}$

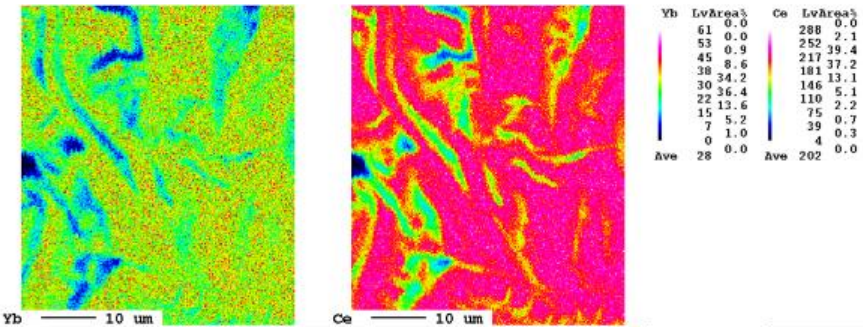

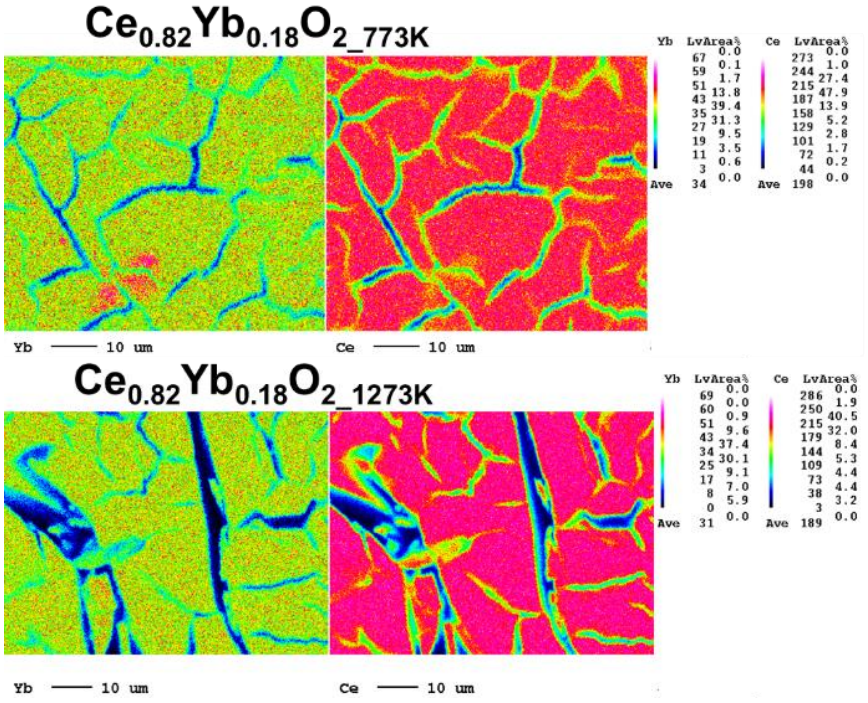

Figure 33. Elemental maps from the $Ce_{1-x}Yb_xO_2$ ($0.004<x<0.18$) nanomaterials.

However, with the increase of the dopant, especially from 15 mol % onwards, high concentration areas are observed in some parts of the maps, which confirm the clusters. The results obtained corroborate the spectroscopic results later discussed. It is interesting to note that when the samples are heated at 1273 K, the clusters are destroyed, which goes in line with the luminescence results (*vide infra*) and those obtained by Oliva et al[27].

6.2.7 Luminescence of low concentration Yb^{3+} ceria nanoparticles

6.2.7.1 Emission spectra

The emission spectra of these samples were collected at room temperature and at cryogenic conditions. Figure 34 shows the emission spectra of 773 K annealed nanomaterials. Nine broad peaks are observed at room temperature (left) in the Stark splitting pattern in the NIR region. The manifold corresponds to the $^2F_{5/2}$-$^2F_{7/2}$ transition of Yb^{3+} ions[4,5]. There are two dominant peaks, the 972 nm and that around 976 nm. Based on the position of the emission lines, it can be hypothesized that the Yb^{3+} ions are located in C_{3V} and C_{4V} symmetry environments in the samples. These findings have been found in CaF_2:Yb^{3+} materials [26,112,188]. These symmetries are possible in the matrix and may be due to defects sites or lattice distortions when the Yb^{3+} ions replace some of the cerium ions in the lattice.

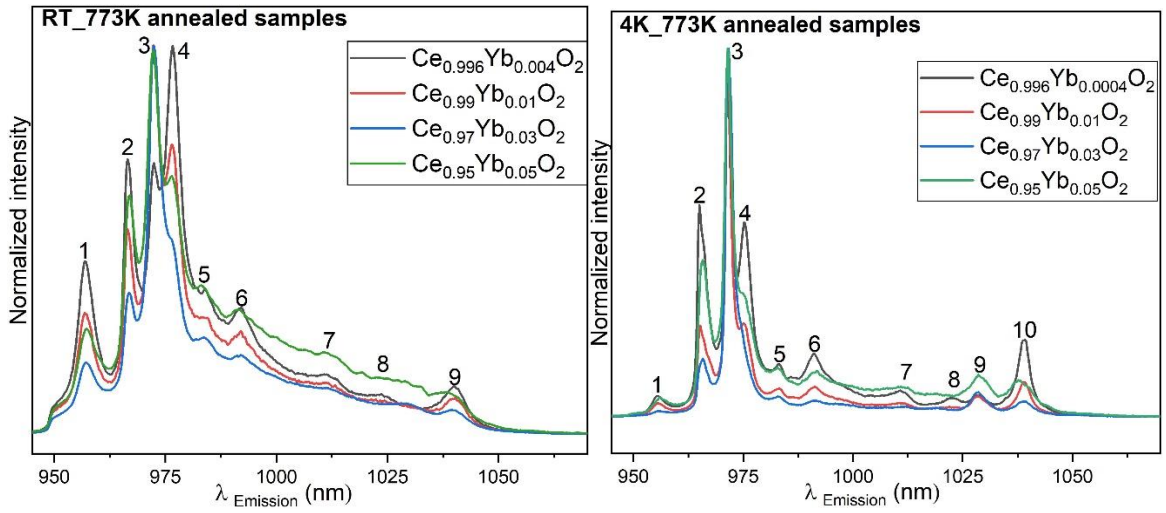

Figure 34. Emission spectra of 773 K annealed nanoparticles collected at room temperature (left) and 4 K (right). $\lambda_{excitation}$ = 915 nm. The delay after the laser pulse was 5 µs and the gate width used was 100 µs.

The intensity of the peak around 972 nm increases significantly as the concentration in Yb^{3+} increases from 1 to 5 mol %. The opposite happens with the intensity of the 976 nm peak. At room temperature, the homogeneous and inhomogeneous broadenings in the spectral emission are very strong, thus the transition between sub-levels is not totally resolved especially for peaks in the high NIR wavelengths. Changes in the concentration of Yb^{3+} ions induce shifts in the peaks, for example the 976 nm peak is red shifted with the increase in the Yb^{3+} ions (Figure 34). This can possibly be due to changes in the crystal site environments increase and also self-absorption.

Figure 34, right shows that at 4 K, the peaks in the emission spectra become sharper and better resolved than at room temperature as homogeneous and inhomogeneous broadenings in the spectral emission are effectively reduced. A total of ten peaks are observed in the Stark splitting pattern. The peaks at around 972 nm and around1028 nm become intense with cooling, especially for the lowest Yb^{3+} ions concentration containing sample. Also, the 976 nm peak intensity is effectively reduced as compared to the room temperature results. In comparison with the emission spectra at room temperature, the 972 nm is slightly red shifted and the 976 nm peak slightly blue shifted as a result of cooling the samples before measurement. This could be due to the fact that that as minor adjustments of the local environment around Yb^{3+} occur, polarizability of the ligands slightly change. Thus, these small shifts observed in the Stark splitting pattern are induced by the changes of the crystal field influenced by where the Yb^{3+} ions are located in the crystal lattices in the samples. These two peaks are lines of non-equivalent Yb^{3+} inside the different lattices. It can be speculated that the 976 nm and 972 nm peaks belong to the C_{3v} and C_{4v} symmetries respectively.

The emission spectra of $Ce_{1-x}Yb_xO_2$ nanocrystals after annealing in air at 1273 K for 2 h and collected at room temperature (left) and at 4 K (right) are illustrated in Figure 35.

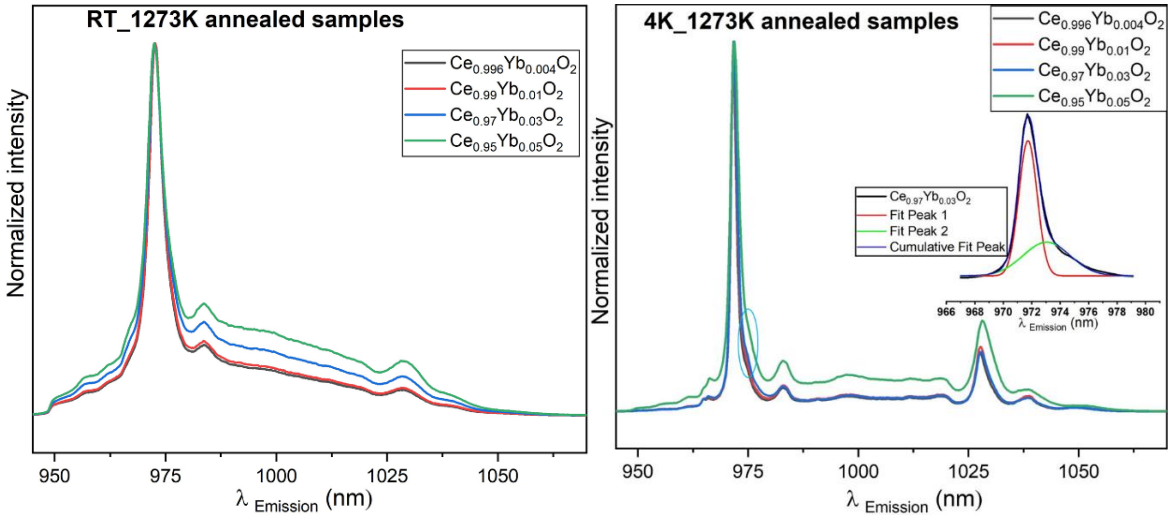

Figure 35. Emission spectra of 1273 K annealed $Ce_{1-x}Yb_xO_2$ nanomaterials measured at room temperature (left) and at 4 K (right). A shoulder on the emission spectra around 976 nm is circled. The Gauss deconvoluted fit for nanoparticles with 3 mol % Yb^{3+} is displayed as an inset showing that two sub-peaks (Fit peak 1 and 2) can be fitted in the dominant peak. $\lambda_{excitation}$ = 915 nm. The delay after the laser pulse was 5 µs and the gate width used was 100 µs.

The shape of the emission spectra changes with annealing temperature as the crystal structure changes. At room temperature, the 972 nm peak is most prevalent and is observed along with two broad peaks as well as shoulder peaks between 950 nm and 970 nm. The most dominant peak is blue shifted and the FWHM increases with the increase of the Yb^{3+} ions amount (see Table 16). Lattice distortion is removed as crystallite growth is promoted resulting in the enhancement of the emission. Due to the position of the emission peaks and the Stark splitting pattern it is likely that the Yb^{3+} ions are located in C_{4v} and C_{3v} symmetry environments like in the room temperature results, although the peak positions are slightly shifted[26]. The emission spectra of 1273 K annealed samples measured at 4 K show sharper and well resolved peaks compared to the spectra measured at room temperature. This is because the processes contributing to the spectral broadening of electronic transitions are reduced and the small differences in the electronic spectra of can be well resolved. The main feature in the emission spectra is the relatively sharp band around 972 nm. This peak is blue shifted with the increase in the Yb^{3+} ion concentration and red shifted with respect to the room temperature. Although the peaks are narrower than those from room temperature measurements, it is still observed that there is an increase in the FWHM, with an increase in the concentration of Yb^{3+} ions (*vide infra*). Also, the 1028 nm peak is red shifted as the concentration of the Yb^{3+} ions increase in the samples. This may be as a result of a mild modification of local environment around Yb^{3+} with concentration[189]. The peaks around 967 nm are well resolved, though

small, compared with room temperature measured samples, which only appear as shoulders. There appears to be a shoulder around 976 nm (circled) that is protruding especially for samples with 0.4, 1 and 3 mol % Yb^{3+} ions. The Gauss deconvoluted fit for one sample (with 3 mol % Yb^{3+}) displayed as an inset in Figure 36, right picture, show that two sub-peaks can be fitted in the original 972 nm peak. These curves have a maximum at 971.7 and 973 nm respectively.

Table 16. FWHM of the 976 nm peak of the Yb^{3+} doped ceria nanoparticles annealed at 1273 K and luminescence measured at RT and at 4 K

Sample	FWHM (nm)	
Annealing temperature	RT	4K
$Ce_{0.996}Yb_{0.004}O_2$	5.81±0.12	1.79±0.03
$Ce_{0.99}Yb_{0.01}O_2$	6.11±0.13	1.95±0.035
$Ce_{0.97}Yb_{0.03}O_2$	7.39±0.20	2.10±0.04
$Ce_{0.95}Yb_{0.05}O_2$	9.26±0.29	3.01±0.07

Kinetics of decay of the Yb^{3+} ions in the lattices were measured and the results deconvoluted by using a mathematical algorithm known as Parallel Factor Analysis (PARAFAC). The results of the deconvolution resulted in the separated emission spectra of the different species (Yb^{3+} ions in different crystal lattice sites) and the luminescence decay time of the respective Yb^{3+} species present in the samples.

6.2.8 PARAFAC analysis results of nanomaterials with low Yb-concentration

6.2.8.1 RT luminescence of 773 K annealed nanomaterials

Figure 36 shows the PARAFAC results of the emission spectra and mono-exponential decay curves and times of the species present (inset). The results show three different emission spectra and luminescence decay kinetics suggesting that there are three species present in the samples. The emission spectra are composed of broad peaks. The luminescence decay times for the species Sp2 and Sp3 are 583.2 μs and 1324.5 μs respectively. Species Sp1 has the least relative emission contribution and thus the determination of the respective decay time very inaccurate. Based on the emission peak pattern, Sp1 can be assigned to Yb^{3+} ions occupying a trigonal symmetry environment. On the other hand, for species Sp2 and Sp3 the C_{4v} and C_{3v} symmetries are assigned based on the location of emission peaks observed for CaF_2:Yb^{3+} ceramics[112,113,188,190].

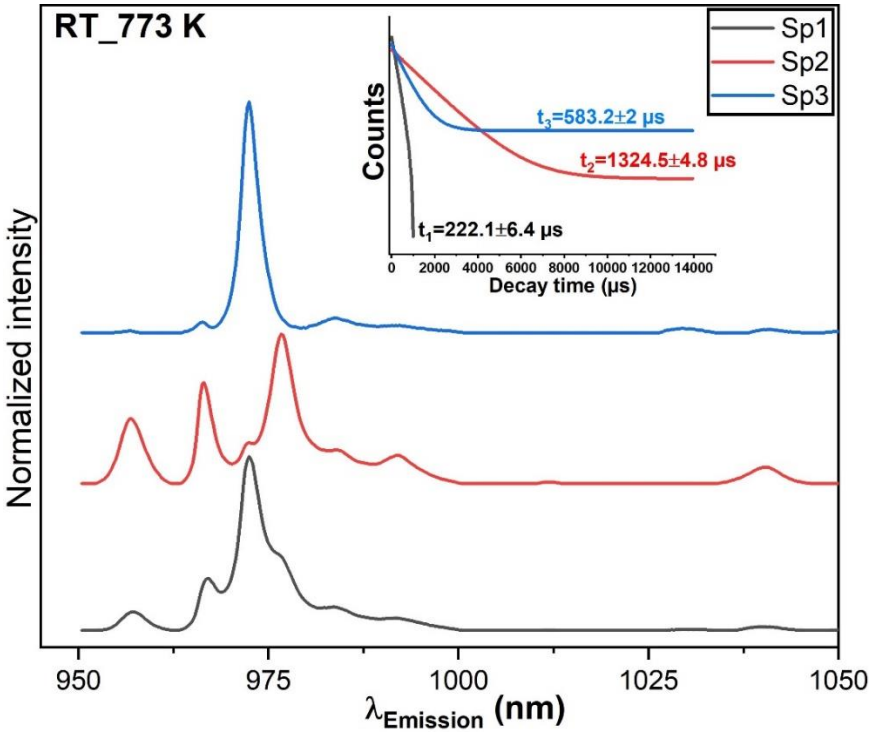

Figure 36. Emission spectra from room temperature -773 K annealed nanomaterials obtained from PARAFAC results. Decay curves together with their decay times shown in the inset. For the luminescence measurements, $\lambda_{excitation}$ = 915 nm. The delay after the laser pulse was 5 µs and the gate width used was 100 µs.

6.2.8.2 4 K luminescence of 773 K annealed nanomaterials

After luminescence measurement of the Yb^{3+} ions in the samples at 4K, the PARAFAC analysis (Figure 37) resulted into the emission spectra and mono-exponential decay curves of the species present (inset). Yb^{3+} ions in three different chemical environments are seen even after cooling the samples to 4 K. The spectra display sharper and more intense signals than from the results obtained from room temperature measurements. Moreover, the peaks also show a blue shift relative to PARAFAC results for room temperature data. Furthermore, the peaks are better resolved with cooling down the samples particularly the peaks around 972 nm and 983 nm. Species Sp1 has the shortest decay time and mostly found in the sample with the highest concentration of Yb^{3+} ions. The decay time of species Sp2 is longest, which indicates a slow rate of energy migration between the isolated Yb^{3+} ions[2]. As in the RT results, Yb^{3+} ions found in species Sp3 could be in C_{3V}, while in the other Yb^{3+} ions in species Sp2 and Sp1, the C_{4V} and C_{3V}[26,112] symmetry environments dominate. More research on the down conversion in ceria-based nanomaterials mixed with Yb^{3+} should be done so as to be able to confidently assign the emission peaks in these materials.

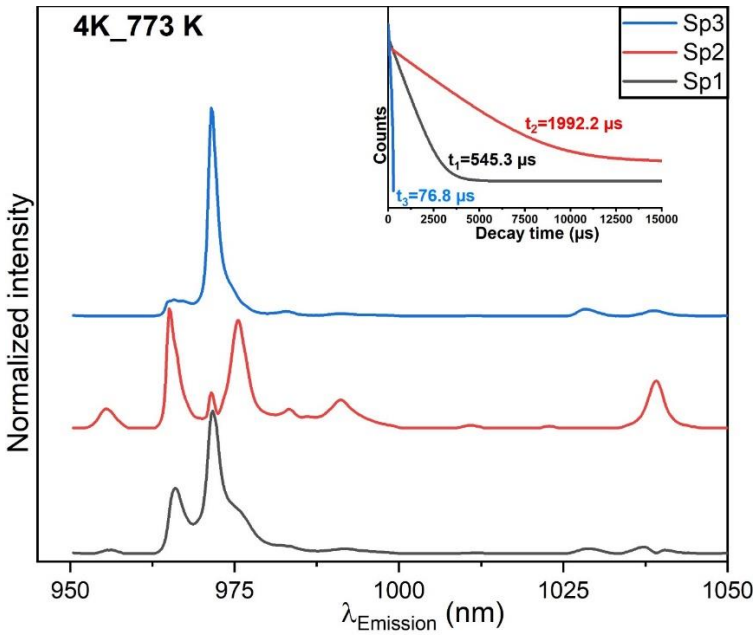

Figure 37. Emission spectra and decay curves with times (inset) of the luminescence of 773 K annealed nanomaterials measured at 4 K. In the TRFLS measurements, $\lambda_{excitation}$ = 915 nm. The delay after the laser pulse was 5 µs and the gate width used was 100 µs. The data was obtained after PARAFAC analysis.

6.2.8.3 RT and 4 K luminescence of 1273 K annealed nanomaterials

The emission spectra and decay times of room temperature and 4 K luminescence measurements of 1273 K annealed samples are shown in Figure 38.

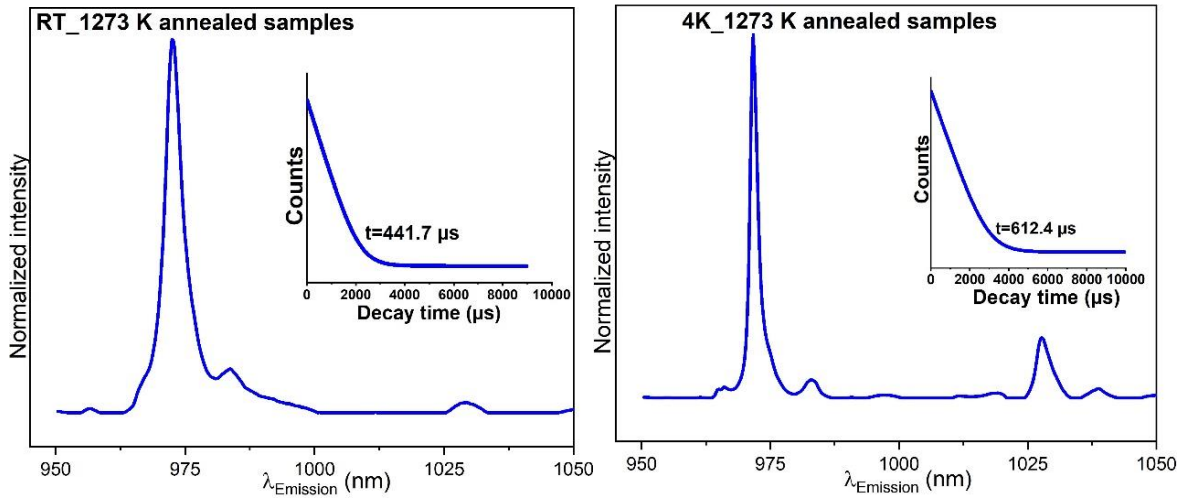

Figure 38. Emission spectra and decay kinetics (inset) of from room temperature and 4 K measured 1273 K annealed samples PARAFACed results. In the TRFLS measurements, $\lambda_{excitation}$ = 915 nm. The delay after the laser pulse was 5 µs and the gate width used was 100 µs.

Deconvoluted RT data shows one Yb^{3+} ions species present which portrays homogeneity and high crystallinity in the samples due to annealing at a higher temperature. A broad spectrum with a main peak centered at 972 nm is observed at room temperature together with a shoulder around 967 nm and three more small peaks. The peaks become sharper with cooling to cryogenic conditions and the shoulder (in room temperature result that is around 967 nm) is well separated into two peaks (although small) and the other peaks are also better resolved and more intense. The luminescence decay kinetics from the species slow at T = 4 K. Yb^{3+} ions are assumed to be in tetragonal and trigonal symmetry environments[112]. Species Sp3 (room temperature, Figure 36) and Sp3 (4 K, Figure 37) 773 K PARAFAC results have an emission profile which to some extent resembles that for which resembles that for single species found in the 1273 K annealed samples.

6.2.9 Luminescence results for ceria nanomaterials with high Yb^{3+} ion concentration

Figure 39 shows the emission spectra of 773 K and 1273 K annealed $Ce_{1-x}Yb_xO_2$ (x=0.15, 0.18 and 0.22) nanomaterials measured at room temperature and at cryogenic conditions. The $^2F_{5/2}$-$^2F_{7/2}$ transition is observed[191]. The spectra consist of two broad peaks with high background, with the 976 nm peak being the most prevalent. This is hypothesized as the average of many spectra from Yb^{3+} ions which are in the close vicinity of each other. Strong emission at 976 nm reveals self-absorption of Yb^{3+} ions in the nanomaterials[5,192]. Also, as Yb^{3+} concentration increases, there is a high chance that more Yb^{3+}-Yb^{3+} clusters are formed thereby reducing the emission of single Yb^{3+} ions [4]. Elemental mapping (Figure 33) where high Yb^{3+} concentration areas are observed corroborates this fact.

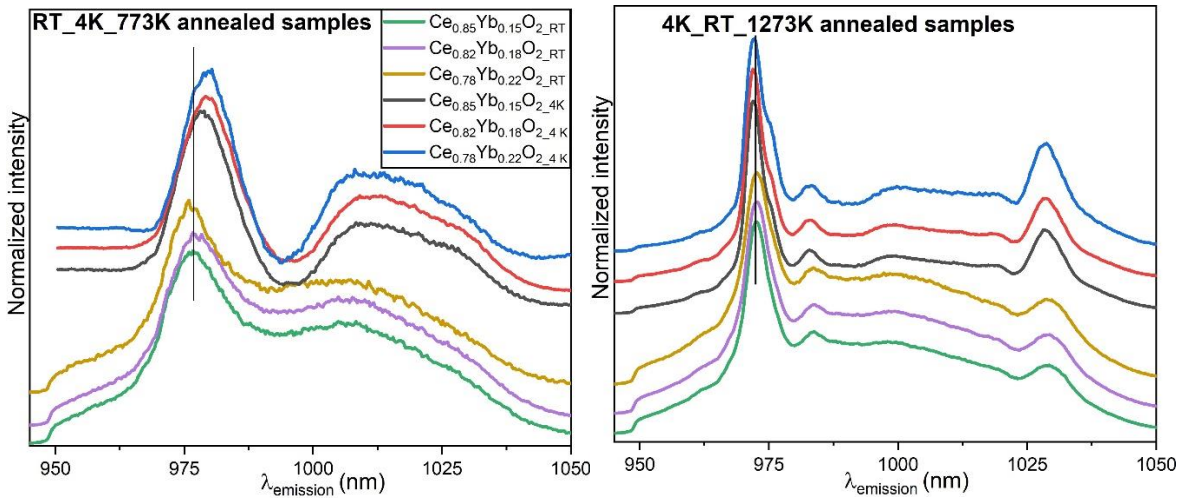

Figure 39. Emission spectra of 773 K (left) and 1273 K (right) annealed Yb^{3+} ion mixed ceria oxides nanomaterials ($Ce_{1-x}Yb_xO_2$ (x=0.15, 0.18 and 0.22)) collected at room temperature and at 4K. $\lambda_{excitation}$ = 915 nm. The delay after the laser pulse was 5 µs and the gate width used was 100 µs.

Contribution of the Yb^{3+} clusters increases and the peaks in the emission spectra broaden. As a result, the distinction between the purely electronic and vibronic transitions is not clear cut. A noticeably red

shifted (most dominant peak shifted from about 978 nm to 980 nm) is observed after cooling the samples down to 4 K before luminescence measurements. These peaks are also better separated compared to room temperature results. Figure 40 shows the FWHM of the dominant peak of the Yb^{3+} ceria mixed oxides. A decrease of the FWHM of the dominant peaks are observed after i) annealing the oxides at a higher temperature and ii) after cooling down the samples to 4 K before luminescence measurements.

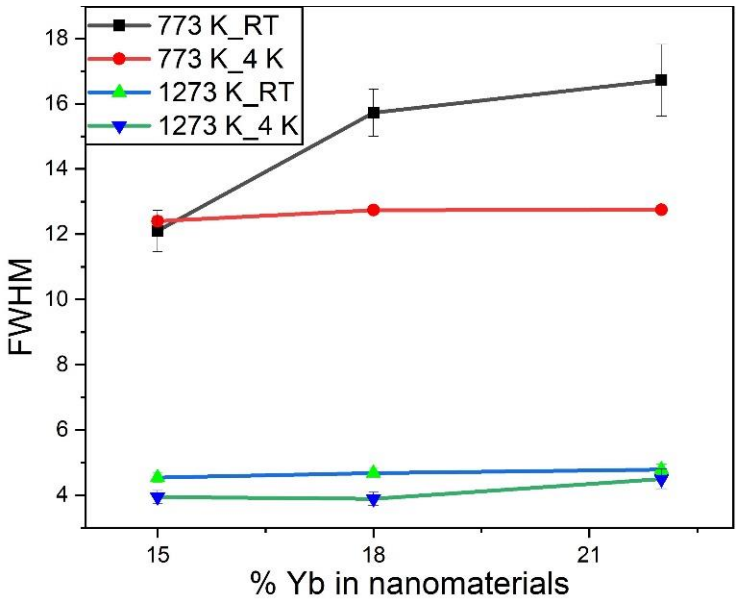

Figure 40. FWHM of the dominant peak of the Yb^{3+} ceria mixed oxides.

Annealing the nanomaterials at 1273 K for 2 h results in the spectral signature change as new peaks emerge (at 983 and 1028 nm), with the most prevalent peak around 972 nm, all becoming slightly sharper after cooling to cryogenic conditions (see FWHM, Figure 40). The peaks also become well separated and a shoulder peak around 976 nm is observed, which is also observed for low Yb^{3+} ions heated at 1273 K for 2 h where the emission is measured after cooling to 4 K (*vide supra*). Also, cooling to 4 K induces a blue shift on the dominant peak. Shoulder around 976 nm at emission profiles for room temperature measured samples. The Yb^{3+} ions with spectra obtained at room temperature and at 4 K are assumed to be in lower symmetry environments based on their emission lines.

6.2.10 Deconvoluted data for luminescence measured at RT and 4 K for 773 K annealed nanomaterials

The emission spectra and decay times based on room temperature and 4 K luminescence measurements of 773 K annealed samples obtained from PARAFAC analysis are shown in Figure 41.

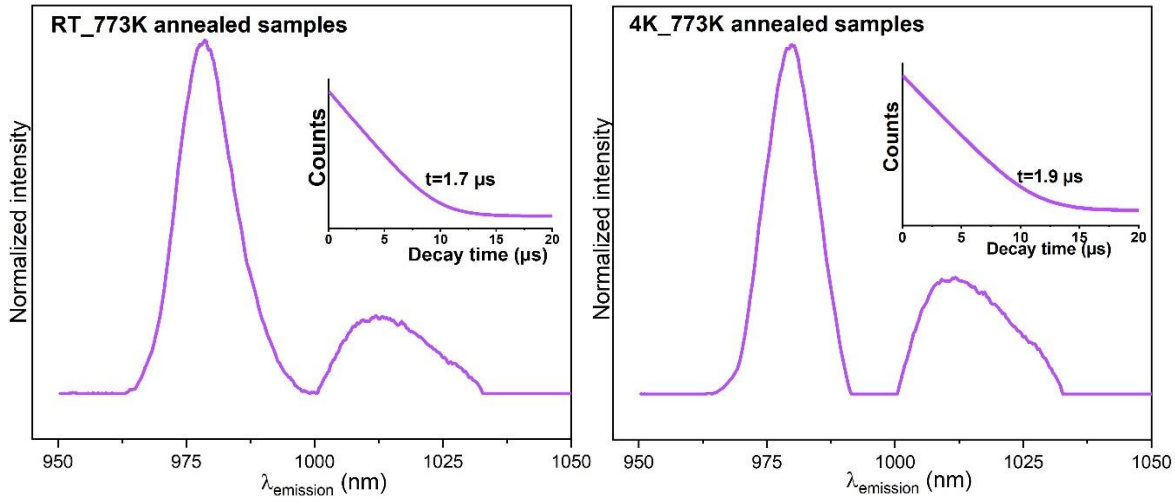

Figure 41. Emission spectra and decay kinetics (inset) of 773 K annealed $Ce_{1-x}Yb_xO_2$ (x=0.15, 0.18 and 0.22) oxides PARAFACed results of luminescence measurements done at room temperature (left) and at 4 K (right). In the TRES measurements, $\lambda_{excitation}$ = 915 nm. The delay after the laser pulse was 5 µs and the gate width used was 100 µs.

The deconvoluted data reveal one Yb^{3+} species present in the samples with the luminescence measured at room temperature and at 4 K. The emission spectra have a broad dominant 978 nm peak along with another broad smaller peak centered at around 1012 nm. The luminescence of this species is greatly quenched showing a luminescence decay time of only 2 µs. This is envisaged to be a result of cross-talk between excited Yb^{3+} in the close vicinity, thus there is enhanced energy migration among Yb^{3+} ions[193]. There is no significant change observed in the PARAFAC data for samples with luminescence measured at 4 K, except a slight red shift of the dominant peak. Thus, it is seen that when concentrations are elevated, as opposed to up to 5 mol %, samples show very small decay time values, signifying a turning point for Yb^{3+}, shifting from singly isolated state to a cluster[2]. Therefore, it is only sensible to reiterate the fact put out by Tamrakar et al. that as Yb^{3+} concentration increases, additional Yb^{3+}- Yb^{3+} pairs are formed, promoting cluster formation thus plummeting the emission of single Yb^{3+} ions[4].

Figure 42 show the emission spectra and decay kinetics (inset) of 1273 K annealed $Ce_{1-x}Yb_xO_2$ (x=0.15, 0.18 and 0.22) mixed oxides PARAFACed results of analyses done at room temperature (left) and at 4 K (right).

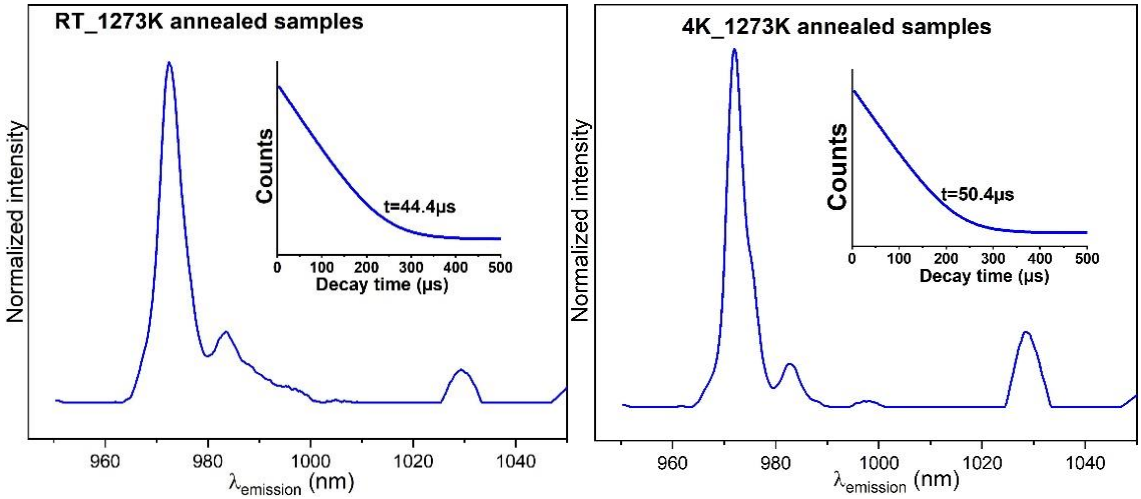

Figure 42. Emission spectra and decay kinetics (inset) of 1273 K annealed $Ce_{1-x}Yb_xO_2$ (x=0.15, 0.18 and 0.22) mixed oxides PARAFACed results of analyses done at room temperature (left) and at 4 K (right). In the TRFLS measurements, $\lambda_{excitation}$ = 915 nm. The delay after the laser pulse was 5 μs and the gate width used was 100 μs.

The deconvoluted data reveal one Yb^{3+} species as far as the 1273 K annealed samples with luminescence measurements at room temperature and 4 K are concerned (shown in Figure 41). The dominant peak in room temperature data is slightly blue shifted and also become sharper with cooling (FWHM= 6.0 nm at RT and 4.82 nm at 4 K). The shoulder peak found around 992 nm in the room temperature result is well resolved after cooling down the samples. Decreasing the temperatures when the TRES measurements are done increase the decay times of the samples by about 14 %.

It is however, interesting to note that, although the concentration of Yb^{3+} ions are significantly different in Yb^{3+} doped ceria and Yb^{3+} mixed ceria oxide nanomaterials, the room temperature and 4 K luminescence spectral signatures of 1273 K annealed nanomaterials (Figure 42) are similar to that from Figure 38. Based on the emission lines present in the spectra, the dopant ions are assumed to be sited in an octahedral or slightly octahedral distorted symmetry environment.

6.3 Conclusion

$Ce_{1-x}Yb_xO_{2-y}$: Eu^{3+} ($0.04 \leq x \leq 0.22$) nanomaterials were synthesized by a thermal decomposition method, with the molar quantities supported by EDX analysis. For the studied nanomaterials, the elemental maps clearly show that cluster formation occurs for 773 K annealed with high Yb^{3+} ion concentration from 15 mol % in the ceria lattice. These clusters are destroyed with annealing to 1273 K. The particle crystallites of the 773 K and 1273 K annealed nanostructure materials are nano-sized and have a cubic fluorite structure with four Raman vibrational modes as revealed by the XRD data and Raman spectroscopy data respectively. The emission spectra of the $Ce_{1-x}Yb_xO_{2-y}$: Eu^{3+} ($0.004 \leq x \leq 0.05$) nanoparticles observed for room temperature and 4 K show a manifold that corresponds to the

$^2F_{5/2}$-$^2F_{7/2}$ transition of Yb^{3+} ions. The peaks are not totally resolved as compared to sharper and better resolved peaks at 4 K. Small shifts are observed in the Stark levels with concentration changes. Based on the position of the emission lines, it can be hinted that the Yb^{3+} ions are located in O_h, C_{3V} and C_{4V} symmetry environments.

Different emission spectral signatures are observed for $Ce_{1-x}Yb_xO_{2-y}$: Eu^{3+} ($0.15 \leq x \leq 0.22$) nanomaterials, although the $^2F_{5/2}$-$^2F_{7/2}$ transition is still detected. The emission spectra comprise of two broad high background dominated peaks. Cooling the samples down to 4 K results in small shifts observed in the Stark splitting pattern. Annealing the nanomaterials at 1273 K for 2 h changes the spectral signature changes as new peaks emerge and all becoming slightly sharper and well resolved after cooling to cryogenic conditions. With the increase in the Yb^{3+} site in lower symmetry environments based on their emission lines.

PARAFAC analysis was executed to extract different Yb^{3+} spectra from the time-resolved luminescence data collected at RT and 4 K for both low Yb^{3+} and high concentration Yb^{3+} ceria nanomaterials. The deconvolution yielded luminescence decay kinetics as well as the associated luminescence spectra of three species for each of the low Yb^{3+} doped ceria samples annealed at 773 K and one species for the 1273 K annealed samples. The decay times for the species for 773 K annealed samples at RT were 222 µs, 583 µs and the longest decaying species had a decay time of about 1325 µs. Decay kinetics after cooling the samples to 4 K resulted in species with the decay times of 76.8 µs, 545.3 µs and 1992 µs. Annealing the nanomaterials at 1273 K and measuring the decay kinetics of the species resulted in species with decay time of 441.7 µs and 612.4 µs at RT and 4 K respectively.

However, the high concentration Yb^{3+} ceria samples annealed at the two temperatures yielded one species with lower decay times as compared to the low Yb^{3+} ions doped ceria samples after PARAFAC analysis. As supported by elemental mapping analysis, increasing Yb^{3+} concentration in the ceria oxides, from 15 mol % upwards, enhances some cluster formation, thus reducing the emission of single Yb^{3+} ions. A notable increase (from 2 µs to 50 µs) in the decay times for these oxides when luminescence kinetics are recorded for 1273 K confirm that with a higher annealing temperature, clusters are removed to a greater extent.

On a balance of probabilities, with good data processing, the presented results on Yb^{3+} could be an adaptable and sensitive structural probe that can be used to probe samples in the NIR region that is effective in technical materials. Also, in conjunction with the PARAFAC algorithm, valuable deconvolution of the data observed in room temperature measurements and overall high-resolution data from 4 K measurements especially provide a distinction on the number of Yb^{3+} species in low and high concentration Yb^{3+} ceria samples, where many sites can contribute to the overall emission.

Chapter 7: Eu^{3+} -doped ceria in biological applications

7.1 Introduction

Cerium oxide or ceria is a rare earth oxide that has found numerous applications in industrial applications and in biomedical applications[53,194]. Nanosized ceria nanoparticles (nanoceria) has notable enzyme-like activity [37,118] which makes them a candidate for many bio-catalytic functions such as peroxidase, catalase, superoxide dismutase activities[37,38,119,120]. These catalytic properties are a result of ceria's ability to reversibly cycle between its ionic states (Ce^{4+} and Ce^{3+}), high stability and high oxygen storage capacity[52,54,121]. One or more of the cerium atoms can be substituted with di- or trivalent atoms, especially lanthanides (e.g. (Eu^{3+})) to modify ceria's oxygen vacancy defect concentration [52 53,54]. With Eu^{3+} ion doping, extensive solubility within the ceria lattice is promoted as its ionic radius is comparable to that of the cerium ions[53]. By doing so, there is the enhancement of catalytic properties as active sites for oxidative species to undergo catalytic reaction for execution of antioxidant activity in medical applications are increased[58]. Also, it may be used as a powerful luminescence probe to characterize the host material on a molecular level.

The urgent need to obtain nano-therapeutic agents with the ability to treat specific diseases at the tissue and cell level resulted in the fabrication of nanoparticles. Reactive oxygen species (ROS), superoxide and peroxynitrite are normal by-products of cellular metabolic reactions, but they cause diseases like sepsis, cancer and schizophrenia in abnormal amounts[52,57]. Nanosized ceria (nanoceria) has attracted special interest since it scavenges ROS[121,124]. One barrier for ceria nanoparticle success past clinical trials is the formation of the protein bio-corona when administered in the body. This results in inflammation and removal of the nanoparticles from blood circulation before they can take effect[133]. Thus, functionalization is done to alleviate this effect. To date, there is increased research on functionalizing nanoceria with DNA, owing to its many advantages[37,141]. Binding single stranded (ss) DNA with nanoceria is easy as it is a single step process involving electrostatic interactions between the particles and the phosphate backbone[120]. Furthermore, ssDNA would stabilize nanoceria in solution, thereby enhancing its surface reactivity[39].

It is possible to display ligands, allowing the precise patterning of multiple proteins, nanoparticles or other elements[142,151,152] using DNA origami. It is a technique for creating arbitrary shapes and patterns on an approximately 100 nm scale[143,144] and is well suited to study distance-dependent reactivities of a ROS source and sink (scavenger)[153]. It is important to understand the effect of distance and orientation of the two variables on nano-enzymatic activity to allow for the tailored design of an effective biological antioxidant and if possible, an effective theranostic. Atomic force microscopy is the technique that is used to easily detect the DNA coated nanoparticles hybridized on top of the DNA origami. In this thesis,

sub 10 nm Eu^{3+} doped ceria nanoparticles have been functionalized by ssDNA and hybridized on DNA origami triangles.

7.2 Characterization techniques

7.2.1 Screening for the optimal sequence for ceria DNA adsorption results

In order to determine the ssDNA sequence for the nanoparticle (NP) functionalization which would give optimum results, ssDNA containing three different bases, that is (Poly Adenine; polyA $(AAA)_{12}$, poly Thymine; PolyT $(TTT)_{12}$ and poly Cytosine; PolyC $(CCC)_{12}$), were screened for ssDNA adsorption. The hydrodynamic size and ζ-potential of the NPs in the aqueous environment were measured. Figure 43 shows the TEM results for the commercial NPs (top left), hydrodynamic size (top right) and the ζ-potential (bottom picture) of the NPs before and after adsorption with different sequence containing ssDNA.

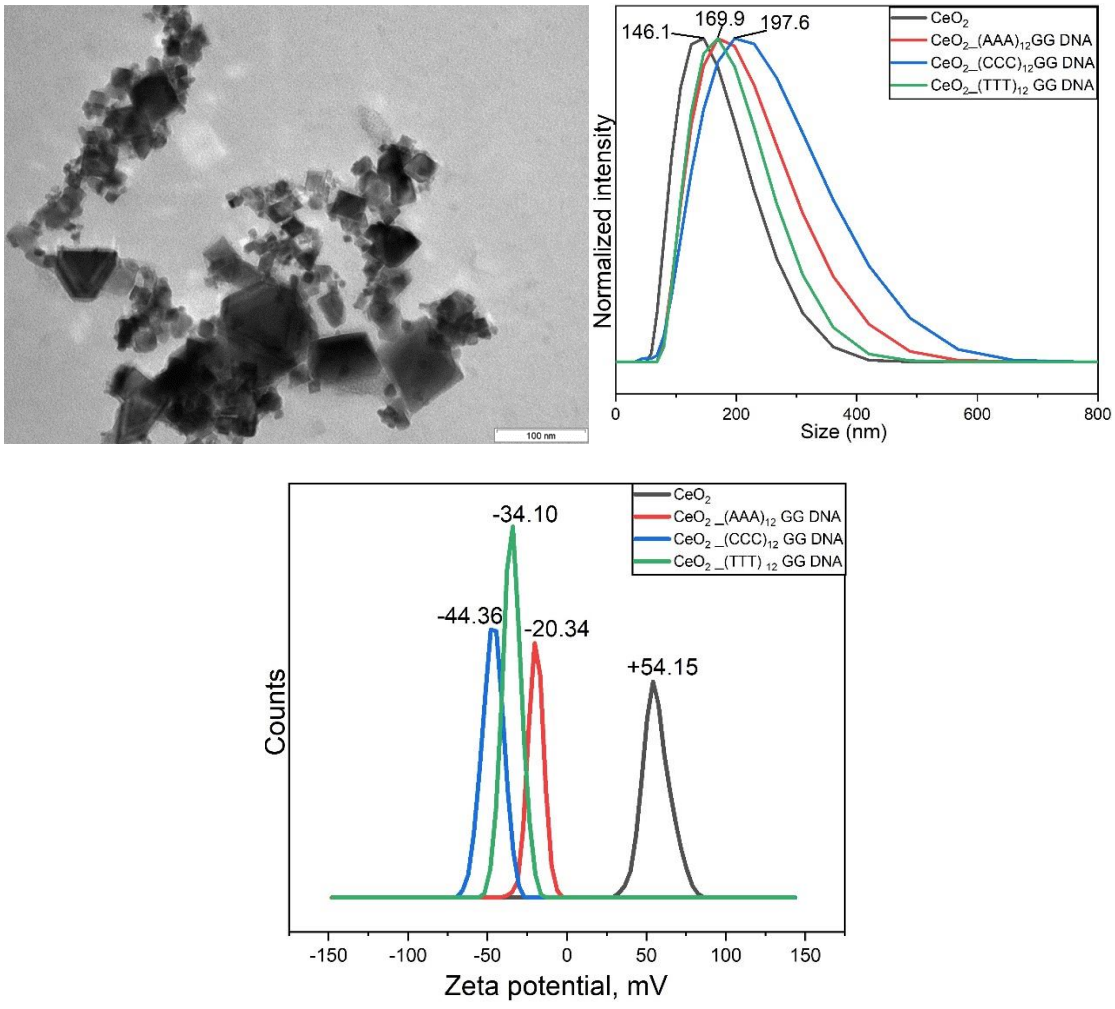

Figure 43. TEM for the commercial NPs (top left), hydrodynamic size (top right) and the ζ-potential (bottom picture) of the NPs before and after adsorption with different sequence containing ssDNA.

The TEM result show that the uncapped nanoparticles are cuboidal in shape, with a size range from approximately 8-25 nm with some substantial agglomeration. The hydrodynamic sizes display size increase with each ssDNA sequence after functionalization, which is shown by a shift of the peak originally at 146.1 nm before the adsorption. This depicts the success of the functionalization. Slight size increase in the agglomerates was noticed with ssDNA with the polyT sequence. Highest agglomeration was noticed with the poly A sequence. With the ζ-potential, a shift in the negative potential (from +55 mV) was observed for all the three sequences, also showing that the adsorption was successful. The NPs proved to be stable, based on the high negative ζ-potential. However, for the next steps, the PolyT sequence was chosen for the functionalization of the NPs by microemulsion as the extent of agglomeration is limited and the nanoparticle stability observed was at the middle point.

7.2.2 TEM results for Eu^{3+} doped ceria nanoparticles

The TEM images of Eu^{3+} doped ceria nanoparticles dispersed in toluene (top) and also dispersed in water (bottom) are displayed in Figure 44. Microscopy images from nanoparticles dispersed in toluene show highly monodisperse and near spherical nanoparticles of size 4.98±0.96 nm. After functionalization with DNA, the morphology of the nanoparticles was also analysed and the TEM image are shown (size is 5.26±0.6 nm).

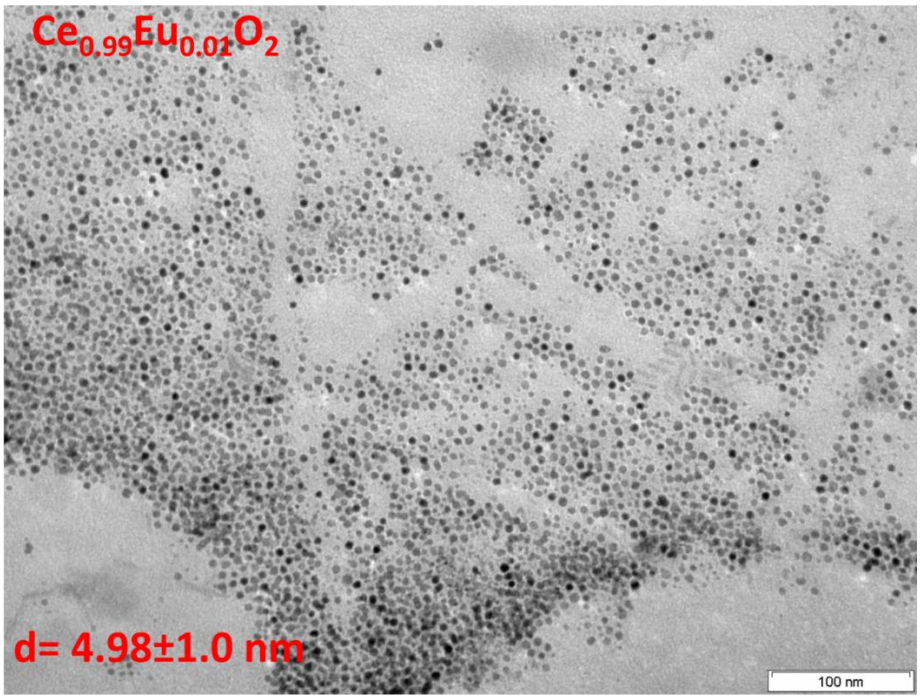

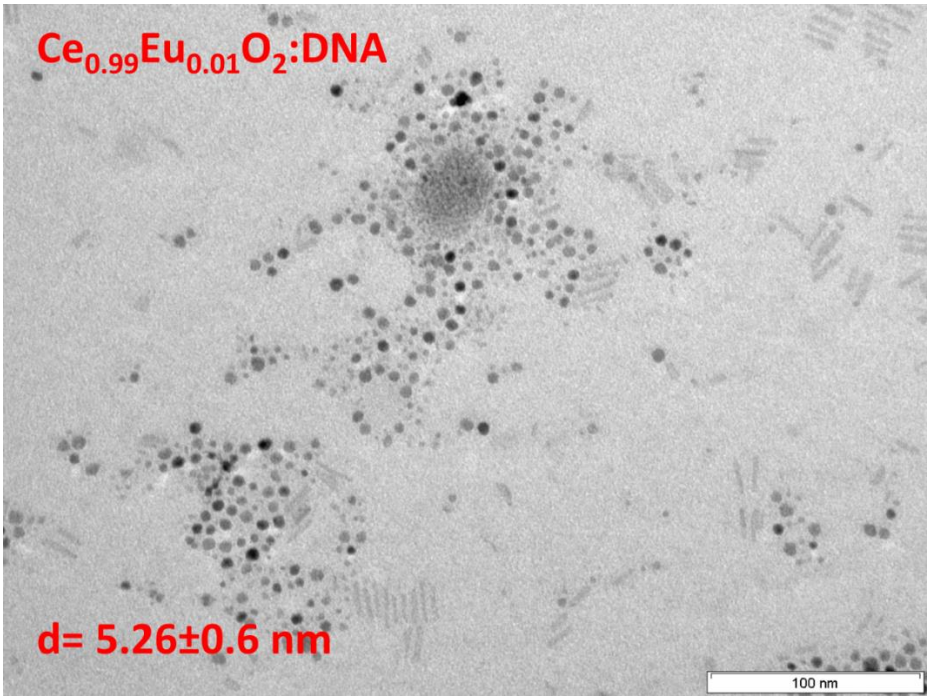

Figure 44. TEM images of Eu^{3+} doped ceria nanoparticles dispersed in toluene (top) and also dispersed in water (bottom).

7.2.3 Luminescence results of the nanoparticles

As the nanoparticles were doped with a luminescence probe, 1 mol % of Eu^{3+}, luminescence measurements were done. The room temperature measurements were done at an excitation wavelength of 396 nm. Figure 45 shows the emission spectra of nanoparticles dispersed in toluene and in water after DNA functionalization.

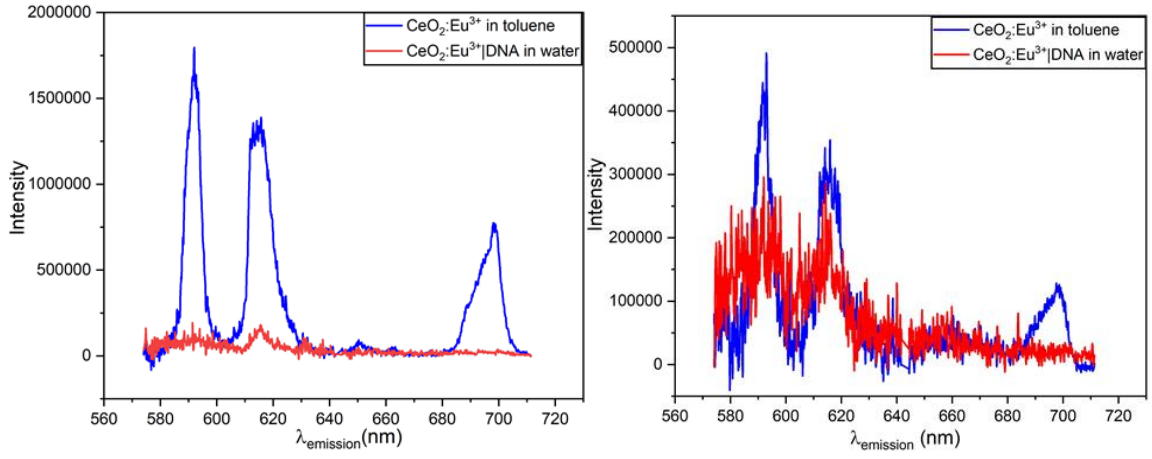

Figure 45. Emission spectra of nanoparticles dispersed in toluene (blue curve) and in water after DNA functionalization (red curve). $\lambda_{excitation}$=396 nm

The Eu^{3+} spectra for the nanoparticles dispersed in toluene and in water are slightly different. The intensity of the $^5D_0$–$^7F_1$ transition > $^5D_0$–$^7F_2$ transition for the nanoparticles dispersed in toluene. However, there is a change in the spectral intensities of the two transitions upon transferring the nanoparticles to water phase using DNA. As can be seen from the spectra, there is Eu^{3+} spectral intensity decrease after phase transfer. This could be due to these reasons: i) possibly to low nanoparticle concentration in water compared to those in toluene after transfer as there are losses incurred during the washing processes after functionalization with DNA ii) Also quenching by the water molecules cannot be ruled out to cause the decrease in the intensity of the nanoparticles dispersed in water.

Analysis of the decay curves and the emission spectra of Eu^{3+} after excitation at $\lambda_{excitation}$ = 396 nm at room temperature revealed one spectrum and decay curve for each of the samples which means that there is one emitting species (lattice site). It is important to note that it is difficult to separate luminescence signals originating from different Eu^{3+} sites due to spectral broadening when using conventional emission spectroscopy, but it was possible to determine the species present using PARAFAC analysis. Figure 46 shows the decay kinetics Eu^{3+} ions in the two samples.

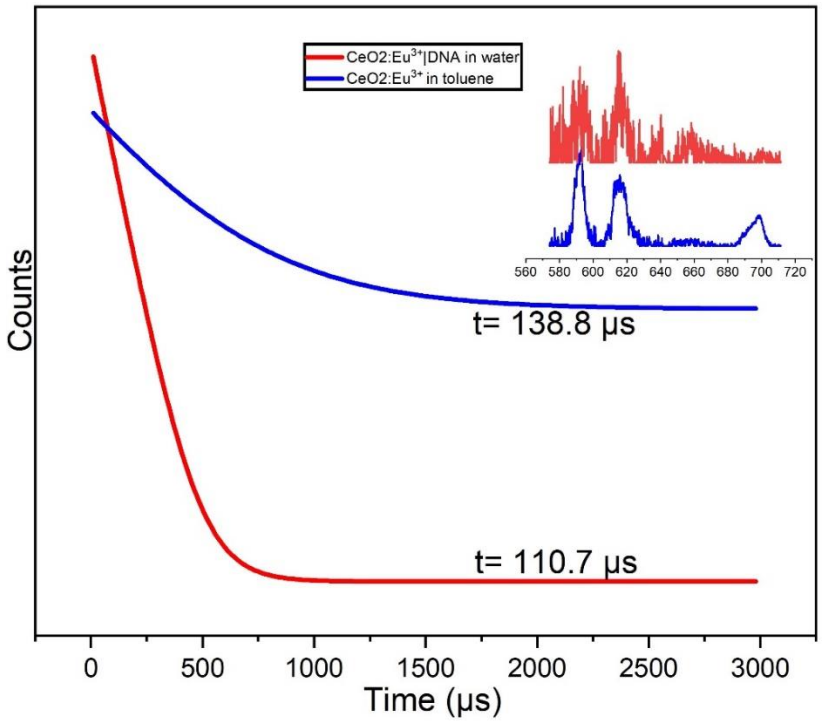

Figure 46. Decay kinetics Eu^{3+} ions in the nanoparticles dispersed in toluene and in water.

As expected, the decay time for the Eu^{3+} in nanoparticles dispersed water was lower than for the nanoparticles in toluene. This can confirm that there is some considerable amount of quenching that happens in water. Also, this could be as a result of the high surface-to-volume ratio as probably most Eu^{3+} are located in or at surface of the nanoparticles with the surface at least partly capped by DNA. From these results,

it is also interesting to note that functionalizing the nanoparticles with DNA results in a change in the spectral configuration; the $^5D_0$–$^7F_2$ transition > $^5D_0$–$^7F_1$ transition.

7.2.4 AFM results for nanoparticles hybridized on DNA origami

One of the images taken using AFM of poly T (T_{24}) DNA functionalized Eu^{3+} doped ceria nanoparticles hybridized on poly A (A_{24}) DNA modified origami triangles is shown in Figure 47.

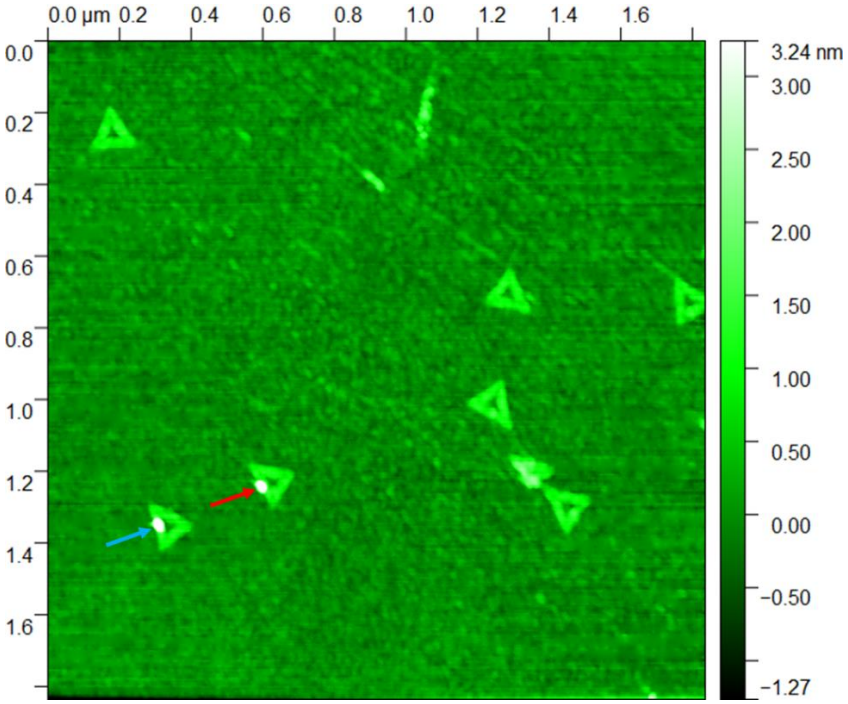

Figure 47. AFM images showing T_{24} DNA functionalized Eu^{3+} doped ceria nanoparticles hybridized on A_{24} DNA modified origami triangles.

The white dots shown by arrows on top of the origami triangles in the images show some hybridized T_{24} DNA-functionalized Eu^{3+} doped ceria nanoparticles. As shown by the images, the height of the nanoparticles is 4.5 nm (pointed by blue arrow) and 5.2 nm (pointed by red arrow). These results are in line with the obtained TEM results. One hypothesis for the lower binding yields of T_{24} DNA functionalized Eu^{3+} doped ceria is that excess T_{24} DNA strands used in the nanoparticle functionalization were not completely removed by micro centrifuge filtration. Thus, they could compete for binding to the A_{24} -modified DNA origami triangles. Another possibility is that the T_{24} DNA strands coating the Eu^{3+} doped ceria nanoparticles form stronger hydrogen bonds with the A_{24} modified DNA origami triangles, hence the electrostatic interactions holding the nanoparticles and the T_{24} DNA coating strands break. More AFM images are shown in the Appendix, Figure 49.

7.3 Conclusion and insights

The T_{24} DNA sequence was chosen for Eu^{3+} doped ceria nanoparticle functionalization based on the zeta potential and size measurements results. Sub 10 nm sized Eu^{3+} doped ceria nanoparticles were

synthesized by a micro-emulsion method. Luminescence measured before and after the nanoparticle functionalization with the T_{24} DNA sequence show that there is surface change and also change of spectral signatures moving from AOT to DNA capping. An attempt to hybridize the nanoparticles on origami triangle was successful, though the yield was low.

As the yields were low, optimization of the functionalization protocol so as to observe an increase on the number of NPs that are hybridized on the origami is the next objective. Alendronate will be tested as a functionalization agent 'bridging' the nanoparticles and ssDNA that would allow hybridization to origami triangles. The final goal in this study would be determining the protective ability of ssDNA functionalized lanthanide doped ceria nanoparticles on ssDNA attached onto DNA origami template, against hydroxyl radicals, a model ROS, produced in the bulk medium. ssDNA functionalized alendronate lanthanide-doped ceria will be placed onto triangular DNA origami and also ssDNA strands will be placed on the DNA origami done at various distances from the nanoparticles. The ROS scavenging property of ceria will be evaluated on the nanoscale to develop a distance activity relationship, thereby determining the extent in which ceria can protect the ssDNA from hydroxyl radical damage. This will be assessed based on the level of damage observed on the ssDNA strands placed at various distances from the ceria nanoparticles, if any. AFM images before and after the production of the hydroxyl radicals will be taken so as to determine the possible 'damage' on the DNA linkers and the DNA origami. With the success of the research, the developed idea will be formalized for use in biomedical applications.

Chapter 8: Summary, Conclusions and Outlook

8.1 Summary and Conclusions

The studies mainly focused on the synthesis of four types of ceria-based tailored nanomaterials for specific applications, structural analysis of ceria-based nanomaterials and the use of PARAFAC analysis in the deconvolution of the spectroscopic data.

Initially, small $Ce_{1-x}Gd_xO_{2-y}$: Eu^{3+} ($0 \leq x \leq 0.4$) nanoparticles were obtained by using a spray pyrolysis technique. Despite the concentrations of Gd^{3+} ions in the nanoparticles, TEM data and XRD data reveal that the particles are nano-sized and of roughly cubic shape and crystal structure ($Fm\bar{3}m$) respectively. The results from the RT time-resolved emission spectra of Eu^{3+} measured at an excitation wavelength of 464 nm showed that mixing with Gd^{3+} results in significantly different emission spectra when compared to pure ceria. The deconvolution of the time-resolved luminescence data produced two Eu^{3+} species for each of the samples. However, one of the species was found for pure ceria site in a high-symmetry environment that can also be selectively excited at 337 nm. Thus, with this method structural information about a lattice site is extracted using Eu^{3+} emission data to assign the lattice sites.

The deconvolution using PARAFAC of RT emission data did not fully resolve very similar sites postulated to be in the samples thus, further analyses were done to obtain high-resolution luminescence data after excitation of the $^5D_0$-$^7F_0$ transition under cryogenic conditions to resolve the minor spectroscopic differences between the different sites. Sites with Eu^{3+} situated in high symmetry environment from the previous experiments were not discernable even in pure ceria, proving that this emission contribution comes from Eu^{3+} on the highest symmetry site, in which a $^5D_0$-$^7F_0$ transition is forbidden. The TLS of CeO_{2-y}: Eu^{3+} reveals three Eu^{3+} species located in three homogenous and distinct coordination environments. The other samples with Gd^{3+} revealed one Eu^{3+} species due to more oxygen vacancies and variations in structure as the Gd^{3+} ions are introduced.

Deconvoluting the TLS data of the CeO_{2-y}: Eu^{3+} sample yielded four species, with one of the species having a visible contribution of the emission from Eu^{3+} ions in the high symmetry coordination environment, superimposed on broader features. The other emission spectral profiles seem rather similar representing the previously three distinct species identified in pure ceria. Deconvolution of the TLS data for the Gd^{3+}-containing samples by PARAFAC yielded four different species, which are more clearly separated in their excitation and emission spectra.

The nanocomposites; 15 % $Ce_xZr_{1-x}O_{2-y}$: Eu^{3+}|YSZ (X=0, 0.5 and 1) were synthesized in the second part of the study by an incipient wetness impregnation method, thereafter annealed at 773 and 1273 K separately for 2 h. Some structural changes were observed by conventional techniques. To complement the results from these techniques, by FLNS, the evolution of the emission patterns from specific Eu^{3+} lattice sites indicating structural changes was tracked. 773 K annealed samples displayed amorphous,

unordered domains characterized by excitation of Eu^{3+} species in a broad range of excitation wavelengths. The TLS of the 1273 K nanocomposites revealed two distinct Eu^{3+} species. The nature of the samples presented a challenging task in the deconvolution using PARAFAC analysis to separate the Eu^{3+} species completely. Overall, there are three different symmetry environments that can be occupied by Eu^{3+} ions in the crystal structure of the Ce/Zr nanocomposites, whereas four are obtained for the nanocomposite without ceria. Also, temperature pretreatment plays a crucial role in the distribution of Eu^{3+} ions over the different lattice sites. Finally, the reducibility of the samples on a basis of the connection between redox properties and catalytic behavior in ceria-based materials was investigated. The H_2-TPR results showed slight variations in the reduction peaks.

$Ce_{1-x}Yb_xO_{2-y}$: Eu^{3+} ($0.04 \leq x \leq 0.22$) nanomaterials were also synthesized by a thermal decomposition method. The concentrations of the elements were verified by EDX analysis. Elemental mapping shows clusters in the 773 K annealed samples with Yb^{3+} concentration from 15 mol %. These clusters are destroyed upon annealing the samples at 1273 K. Based on the XRD data, the particles are nano-sized and have a cubic fluorite structure. The time-resolved spectroscopy of Yb^{3+} was recorded at a wavelength of excitation of 915 nm. The emission spectra observed have a manifold that corresponds to the $^2F_{5/2}$-$^2F_{7/2}$ transition of Yb^{3+} ions. At room temperature, the peaks in the emission spectra are broad and not fully resolved. Nevertheless, at 4 K, the peaks in the emission spectra become sharper and better resolved. Slight shifts are observed in the Stark splitting pattern induced by the variations of the crystal field.

For low concentration Yb^{3+} -doped ceria samples, nine broad peaks are observed at RT in the Stark splitting pattern, while more peaks that are sharper and better resolved are observed for samples measured at 4 K. Based on the position of the emission lines, the Yb^{3+} ions are hypothesized to be located in O_h, C_{3V} and C_{4V} symmetry environments. The $^2F_{5/2}$-$^2F_{7/2}$ transition is also observed in the Stark splitting pattern of Yb^{3+} ceria nanomaterials with high concentration of Yb^{3+} heated at 773 K. The spectra contain two broad high background dominated peaks. Cooling the samples down to 4 K results in small shifts observed in the Stark splitting pattern. Also, annealing the nanomaterials at 1273 K for 2 h changes the spectral profiles changes as new, slightly sharper and better resolved peaks emerge after cooling to cryogenic conditions. With the increase in the Yb^{3+} concentration in the ceria lattice, the Yb^{3+} ions with spectra obtained at room temperature and at 4 K site in lower symmetry environments based on their emission lines. The deconvolution of the time resolved spectroscopy data resulted in three Yb^{3+} ions species for 773 K heated samples at RT and also at 4 K. Only one species was obtained after annealing the nanomaterials at 773 K and 1273 K for 2 h. The species had drastically lower decay times in comparison with the low Yb^{3+} ion doped ceria samples after PARAFAC analysis.

Finally, hydrophobic sub 10 nm Eu^{3+} doped ceria nanoparticles were synthesized and made water dispersible by using ssDNA. The surface change on the nanoparticles was observable as the spectral signature changed after transfer into water phase. After hybridization to DNA Origami, the functionalized nanoparticles were visualized to have attached to the overhangs on the DNA origami by AFM, where bright spots were seen on top of the triangles.

In this thesis, the 'union' of high-resolution emission spectroscopy done using a narrow-bandwidth and tunable laser source especially under cryogenic conditions and the presented PARAFAC algorithm is especially useful for the identification of Eu^{3+} and Yb^{3+} species in challenging samples where there is superimposition of different emitting species by nature of their location thereby contributing to the overall emission. Thus, with good data processing, Eu^{3+} and Yb^{3+} ions are very versatile, robust and sensitive structural probes where invaluable information can be obtained providing a distinction on the number of species and sites available in different lattices in technical materials that change over time – such as high temperature ceramics and catalysts and also for biological specimens.

8.2 Outlook and Perspectives

Research is never complete without pondering on the future work that needs to be concluded so as to achieve a deeper understanding of the system studied and possibly offer solutions to the challenges of today, especially in the face of climate change. Ce/Zr mixed oxides doped with 1 mol % Eu^{3+} and supported on YSZ, as potential catalysts, were successfully synthesized and structural changes monitored after thermal subjection at two different temperatures. The redox behaviour as determined using H_2-TPR experiments showed a good response. However, a good catalyst has good attributes when it is potentially stable against deactivation during redox cycling at high temperatures, for example, when used in three-way catalysts[50]. In this regard, the nanocomposites that were synthesized in this study will be tested for their stability under harsh environments, for example under repeated severe oxidation mild conditions (SRMO). Characterization of the nanocomposites, as done in the study, after each redox cycle, will be done to correlate the redox response with structure of the nanocomposites.

As the protective ability of Eu^{3+} doped ceria nanoparticles against generated reactive oxygen species will be the final objective in the development towards a viable theranostic, to reach the decisive goal, other variables will have to be considered. Since the Ce^{3+}/Ce^{4+} ratio is an important aspect for the enhancement of the catalytic properties when the fraction of Ce^{3+} ions increases, different composition of dopants, (Zr^{4+}, Gd^{3+}, Ti, V or other lanthanide ions) doped individually or co-doped with Eu^{3+} will be used to control the Ce^{3+}/Ce^{4+} ratio. After targeted doping on the ceria nanoparticles, structural and catalytic characterization will be performed to evaluate the effect of doping on the structural and catalytic properties of the nanoparticles.

Chapter 9: Appendix

9.1 Abbreviations

AFM	Atomic force microscopy
C_3V	Trigonal
C_4V	Tetragonal
CT	Charge transfer
DC	Down conversion
DLS	Dynamic light scattering
EDX	Energy dispersive X Ray Spectroscopy
EMCCD	Electron multiplying charge coupled device
FLNS	Fluorescence line narrowing spectroscopy
FWHM	Full width at half maximum
GDC	Gadolinium doped ceria
HAADF	STEM High angle annular dark field
HRTEM	High resolution transmission electron microscopy
HS	High symmetry
LS	Low symmetry
NIR	Near infrared
NIR	Near infra-red
NN	Nearest neighbor
NNN	Next nearest neighbor
NPs	nanoparticles
N_v Parameter	Crystal field splitting parameter
O_h	Octahedral
OSC	Oxygen storage capacity
PARAFAC	Parallel factor analysis
R	Asymmetry ratio
ROS	Reactive oxygen species
RT	Room temperature
SDC	Samarium doped ceria
SEM	Scanning electron microscopy
SOFC	Solid oxide fuel cells
ssDNA	Single strand DNA
TEM	Transmission electron microscopy
TLS	Total luminescence spectra
TPR-MS	Temperature programmed reduction mass spectroscopy
TRS	Time resolved spectroscopy
UC	upconversion

UCNPs	Upconversion nanoparticles
UV-Vis	Ultraviolet visible
XRD	X ray diffraction
YSZ	Yttrium stabilized zirconia

9.2 Supporting information

The high angle annular dark field (HAADF)-STEM for 15 % CeO_{2-y}:Eu^{3+}|YSZ heated at 773 K for 2 h and 1273 K for 2 h are shown in Figure 48.

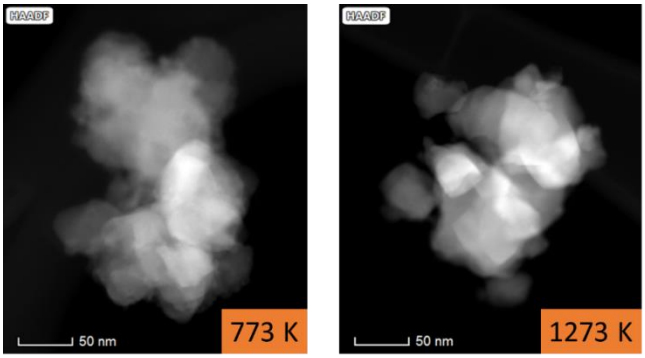

Figure 48. High angle annular dark field (HAADF)-STEM for CeO_{2-y}: Eu^{3+}|YSZ heated at 773 K for 2 h (top) and 1273 K for 2 h (bottom).

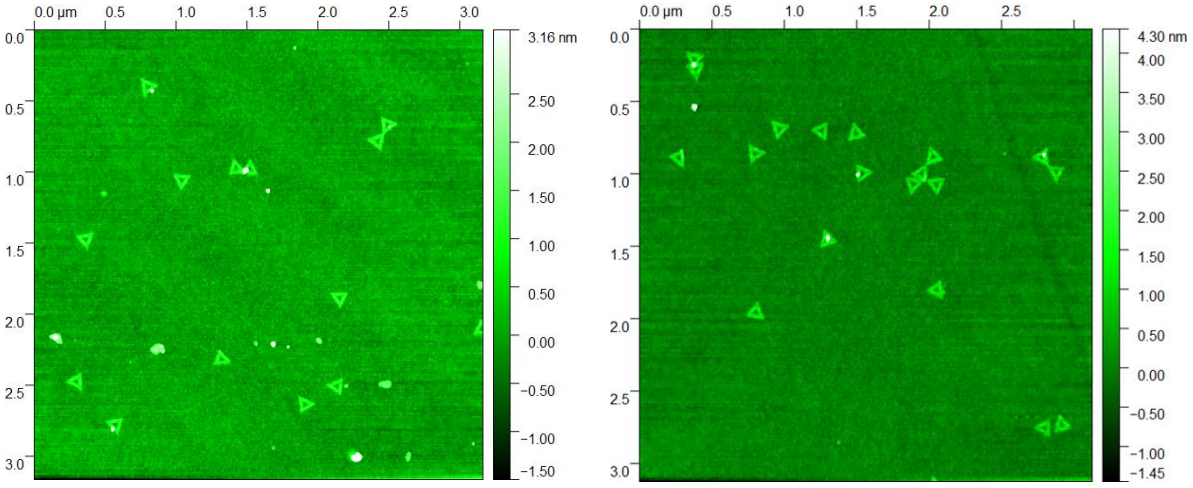

Figure 49. AFM images showing T_{24} DNA functionalized Eu^{3+} doped ceria nanoparticles hybridized on A_{24} DNA modified origami triangles.

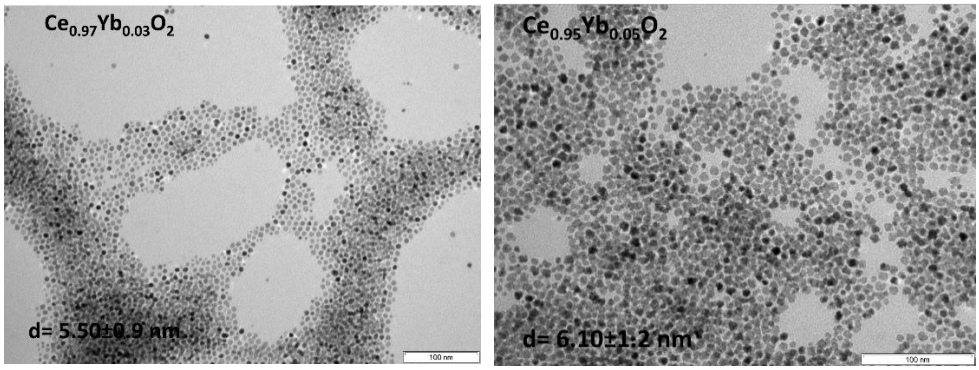

Figure 50. TEM micrographs for $Ce_{1-x}Yb_xO_2$ (x=0.03 and 0.05) nanomaterials.

Chapter 10: Bibliography

1 D'Achille, A. E. *et al.* Rare-earth-doped cerium oxide nanocubes for biomedical near-infrared and magnetic resonance imaging. *ACS Biomaterials Science & Engineering* **6**, 6971-6980 (2020).

2 Mei, S. *et al.* Networking state of ytterbium ions probing the origin of luminescence quenching and activation in nanocrystals. *Advanced Science* **8**, 2003325 (2021).

3 Alowakennu, M., Adams, L. A. & Abdulwahab, K. O. Synthesis of Ceria (CeO2) Nanoparticles and Their Application in Colorimetric Probes for the Determination of Ascorbic Acid. *ChemistrySelect* **7**, e202103463 (2022).

4 Tamrakar, R. K., Bisen, D., Upadhyay, K., Sahu, I. P. & Brahme, N. Effect of synthesis annealing temperature & Yb 3+ concentration on photoluminescence properties of monoclinic Gd 2 O 3 phosphor. *Journal of Optics* **44**, 337-345 (2015).

5 Zou, Z. *et al.* Photoluminescence property and laser performance in Yb-doped Sr 1-x Gd x F 2+ x single crystals. *Optical Materials Express* **8**, 1747-1753 (2018).

6 Zhang, D.-Y. *et al.* Ceria nanozymes with preferential renal uptake for acute kidney injury alleviation. *ACS Applied Materials & Interfaces* **12**, 56830-56838 (2020).

7 Li, Y., Li, Y., Wang, H. & Liu, R. Yb3+, Er3+ codoped cerium oxide upconversion nanoparticles enhanced the enzymelike catalytic activity and antioxidative activity for Parkinson's disease treatment. *ACS Applied Materials & Interfaces* **13**, 13968-13977 (2021).

8 Ozawa, M., Takahashi-Morita, M., Kobayashi, K. & Haneda, M. Core-shell type ceria zirconia support for platinum and rhodium three way catalysts. *Catalysis Today* **281**, 482-489 (2017).

9 Qiao, Z. A., Wu, Z. & Dai, S. Shape-Controlled Ceria-based Nanostructures for Catalysis Applications. *ChemSusChem* **6**, 1821-1833 (2013).

10 Rood, S., Eslava, S., Manigrasso, A. & Bannister, C. Recent advances in gasoline three-way catalyst formulation: A review. *Proceedings of the Institution of Mechanical Engineers, Part D: Journal of Automobile Engineering* **234**, 936-949 (2020).

11 Wang, Y. *et al.* Alleviation of nitrogen stress in rice (Oryza sativa) by ceria nanoparticles. *Environmental Science: Nano* **7**, 2930-2940 (2020).

12 Zhou, X. *et al.* Alendronate-modified nanoceria with multiantioxidant enzyme-mimetic activity for reactive oxygen species/reactive nitrogen species scavenging from cigarette smoke. *ACS applied materials & interfaces* **13**, 47394-47406 (2021).

13 Li, F. *et al.* Decreasing Crystallinity is Beneficial to the Superoxide Dismutase-like Activity of Ceria Nanoparticles. *ChemNanoMat* **8**, e202100466 (2022).

14 Tang, S. *et al.* Ceria nanoparticles promoted the cytotoxic activity of CD8+ T cells by activating NF-κB signaling. *Biomaterials science* **7**, 2533-2544 (2019).

15 Soren, S., Jena, S. R., Samanta, L. & Parhi, P. Antioxidant potential and toxicity study of the cerium oxide nanoparticles synthesized by microwave-mediated synthesis. *Applied biochemistry and biotechnology* **177**, 148-161 (2015).

16 Baldim, V., Bedioui, F., Mignet, N., Margaill, I. & Berret, J.-F. The enzyme-like catalytic activity of cerium oxide nanoparticles and its dependency on Ce 3+ surface area concentration. *Nanoscale* **10**, 6971-6980 (2018).

17 Matović, B. *et al.* Electrical and microstructural properties of Yb-doped CeO2. *Journal of Asian Ceramic Societies* **2**, 117-122 (2014).

18 Chen, A., Zhou, Y., Ta, N., Li, Y. & Shen, W. Redox properties and catalytic performance of ceria–zirconia nanorods. *Catalysis Science & Technology* **5**, 4184-4192 (2015).

19 Chemura, S. *et al.* Europium-Doped Ceria–Gadolinium Mixed Oxides: PARAFAC Analysis and High-Resolution Emission Spectroscopy under Cryogenic Conditions for Structural Analysis. *The Journal of Physical Chemistry A* **124**, 4972-4983 (2020).

20 Primus, P.-A., Menski, A., Yeste, M. P., Cauqui, M. A. & Kumke, M. U. Fluorescence Line-Narrowing Spectroscopy as a Tool to Monitor Phase Transitions and Phase Separation in Efficient Nanocrystalline Ce x Zr1–x O2: Eu3+ Catalyst Materials. *The Journal of Physical Chemistry C* **119**, 10682-10692 (2015).
21 Primus, P.-A. *et al.* High-resolution spectroscopy of europium-doped ceria as a tool to correlate structure and catalytic activity. *The Journal of Physical Chemistry C* **118**, 23349-23360 (2014).
22 Boulon, G. Why so deep research on Yb3+-doped optical inorganic materials? *Journal of Alloys and Compounds* **451**, 1-11 (2008).
23 Liu, L., Xing, J., Shang, F. & Chen, G. Structure and up-conversion luminescence of Yb3+/Ho3+ co-doped fluoroborate glasses. *Optics Communications* **490**, 126944 (2021).
24 Bünzli, J.-C. G. in *Handbook on the Physics and Chemistry of Rare Earths* Vol. 50 141-176 (Elsevier, 2016).
25 Qin, W.-P. *et al.* Multi-ion cooperative processes in Yb3+ clusters. *Light: Science & Applications* **3**, e193-e193 (2014).
26 Petit, V., Camy, P., Doualan, J.-L., Portier, X. & Moncorgé, R. Spectroscopy of Yb 3+: CaF 2: From isolated centers to clusters. *Physical Review B* **78**, 085131 (2008).
27 Oliva, J., De la Rosa, E., Diaz-Torres, L., Salas, P. & Ángeles-Chavez, C. Annealing effect on the luminescence properties of BaZrO 3: Yb 3+ microcrystals. *Journal of Applied Physics* **104**, 023505 (2008).
28 Kearney, J., Hernández-Reta, J. & Baker, R. Redox and catalytic properties of Ce–Zr mixed oxide nanopowders for fuel cell applications. *Catalysis today* **180**, 139-147 (2012).
29 Kuchibhatla, S. V. *et al.* An unexpected phase transformation of ceria nanoparticles in aqueous media. *Journal of materials research* **34**, 465-473 (2019).
30 Florea, M., Avram, D., Maraloiu, V. A., Cojocaru, B. & Tiseanu, C. Heavy doping of ceria by wet impregnation: a viable alternative to bulk doping approaches. *Nanoscale* **10**, 18043-18054 (2018).
31 Małecka, M. A. Characterization and thermal stability of Yb-doped ceria prepared by methods enabling control of the crystal morphology. *CrystEngComm* **19**, 6199-6207 (2017).
32 Thorat, A. V., Ghoshal, T., Carolan, P., Holmes, J. D. & Morris, M. A. J. T. J. o. P. C. C. Defect chemistry and vacancy concentration of luminescent europium doped ceria nanoparticles by the solvothermal method. **118**, 10700-10710 (2014).
33 Anjaneya, K., Singh, M. P. J. J. o. A. & Compounds. Synthesis and properties of gadolinium doped ceria electrolyte for IT-SOFCs by EDTA-citrate complexing method. **695**, 871-876 (2017).
34 Yeste, M. P. *et al.* Low-Temperature Growth of Reactive Pyrochlore Nanostructures on Zirconia-Supported Ceria: Implications for Improved Catalytic Behavior. *ACS Applied Nano Materials* **5**, 6316-6326 (2022).
35 Chen, Z. *et al.* Preparation and upconversion luminescence of Er3+/Yb3+ codoped Y2Ti2O7 nanocrystals. *Materials Letters* **68**, 137-139 (2012).
36 Yang, Z.-Y. *et al.* Photosensitizer-loaded branched polyethylenimine-PEGylated ceria nanoparticles for imaging-guided synchronous photochemotherapy. *ACS Applied Materials & Interfaces* **7**, 24218-24228 (2015).
37 Pautler, R. *et al.* Attaching DNA to nanoceria: regulating oxidase activity and fluorescence quenching. *ACS applied materials & interfaces* **5**, 6820-6825 (2013).
38 Zeng, C. *et al.* Engineering Nanozymes Using DNA for Catalytic Regulation. *ACS applied materials & interfaces* **11**, 1790-1799 (2018).
39 Bülbül, G., Hayat, A. & Andreescu, S. ssDNA-Functionalized Nanoceria: A Redox-Active Aptaswitch for Biomolecular Recognition. *Advanced healthcare materials* **5**, 822-828 (2016).

40 Maurya, R., Gupta, A., Omar, S. & Balani, K. Effect of sintering on mechanical properties of ceria reinforced yttria stabilized zirconia. *Ceramics International* **42**, 11393-11403 (2016).
41 Artini, C. *et al.* Structural features of Sm-and Gd-doped ceria studied by synchrotron X-ray diffraction and μ-Raman spectroscopy. **54**, 4126-4137 (2015).
42 Andersson, D. A., Simak, S. I., Skorodumova, N. V., Abrikosov, I. A. & Johansson, B. J. P. o. t. N. A. o. S. Optimization of ionic conductivity in doped ceria. **103**, 3518-3521 (2006).
43 Dholabhai, P. P., Adams, J. B., Crozier, P. & Sharma, R. J. P. C. C. P. A density functional study of defect migration in gadolinium doped ceria. **12**, 7904-7910 (2010).
44 Lucid, A. K., Keating, P. R., Allen, J. P. & Watson, G. W. J. T. J. o. P. C. C. Structure and reducibility of CeO2 doped with trivalent cations. **120**, 23430-23440 (2016).
45 Florea, M. *et al.* Influence of Gd and Pr doping on the properties of ceria: texture, structure, redox behaviour and reactivity in CH 4/H 2 O reactions in the presence of H 2 S. **8**, 1333-1348 (2018).
46 Goulart, C. & Djurado, E. J. J. o. t. E. C. S. Synthesis and sintering of Gd-doped CeO2 nanopowders prepared by ultrasonic spray pyrolysis. **33**, 769-778 (2013).
47 Liu, J. *et al.* High performance low-temperature solid oxide fuel cells based on nanostructured ceria-based electrolyte. *Nanomaterials* **11**, 2231 (2021).
48 Reddy, B. M., Saikia, P., Bharali, P., Katta, L. & Thrimurthulu, G. Highly dispersed ceria and ceria–zirconia nanocomposites over silica surface for catalytic applications. *Catalysis Today* **141**, 109-114 (2009).
49 Chen, H., Ye, Z., Cui, X., Shi, J. & Yan, D. A novel mesostructured alumina–ceria–zirconia tri-component nanocomposite with high thermal stability and its three-way catalysis. *Microporous and mesoporous materials* **143**, 368-374 (2011).
50 Arias-Duque, C. *et al.* Improving the redox response stability of ceria-zirconia nanocatalysts under harsh temperature conditions. *Chemistry of Materials* **29**, 9340-9350 (2017).
51 Yeste, M. P. *et al.* Rational design of nanostructured, noble metal free, ceria–zirconia catalysts with outstanding low temperature oxygen storage capacity. *Journal of Materials Chemistry A* **1**, 4836-4844 (2013).
52 Othman, A., Hayat, A. & Andreescu, S. Eu-Doped Ceria Nanocrystals as Nanoenzyme Fluorescent Probes for Biosensing. *ACS Applied Nano Materials* **1**, 5722-5735 (2018).
53 Kumar, A., Babu, S., Karakoti, A. S., Schulte, A. & Seal, S. Luminescence properties of europium-doped cerium oxide nanoparticles: role of vacancy and oxidation states. *Langmuir* **25**, 10998-11007 (2009).
54 Reed, K. *et al.* Exploring the properties and applications of nanoceria: is there still plenty of room at the bottom? *Environmental Science: Nano* **1**, 390-405 (2014).
55 Acharya, S., Gaikwad, V., Sathe, V. & Kulkarni, S. J. A. P. L. Influence of gadolinium doping on the structure and defects of ceria under fuel cell operating temperature. **104**, 113508 (2014).
56 Biesuz, M., Dell'Agli, G., Spiridigliozzi, L., Ferone, C. & Sglavo, V. J. C. I. Conventional and field-assisted sintering of nanosized Gd-doped ceria synthesized by co-precipitation. **42**, 11766-11771 (2016).
57 Hernández-Castillo, Y. *et al.* Antioxidant activity of cerium oxide as a function of europium doped content. *Ceramics International* **45**, 2303-2308 (2019).
58 Chen, B.-H. & Stephen Inbaraj, B. Various physicochemical and surface properties controlling the bioactivity of cerium oxide nanoparticles. *Critical reviews in biotechnology* **38**, 1003-1024 (2018).
59 Raj, A. K., Rao, P. P., Sreena, T. & Thara, T. A. J. P. C. C. P. Influence of local structure on photoluminescence properties of Eu 3+ doped CeO 2 red phosphors through induced oxygen vacancies by contrasting rare earth substitutions. **19**, 20110-20120 (2017).

60 Sorbello, C., Barja, B. C. & Jobbagy, M. J. J. o. M. C. C. Monodispersed Ce (IV)–Gd (III)–Eu (III) oxide phosphors for enhanced red emission under visible excitation. **2**, 1010-1017 (2014).
61 Avram, D. *et al.* Heavily impregnated ceria nanoparticles with europium oxide: spectroscopic evidences for homogenous solid solutions and intrinsic structure of Eu 3+-oxygen environments. **49**, 2117-2126 (2014).
62 Das, D., Gupta, S. K., Mohapatra, M. & Sudarshan, K. Defect engineering in trivalent ion doped ceria through vanadium assisted charge compensation: insight using photoluminescence, positron annihilation and electron spin resonance spectroscopy. *Dalton Transactions* **50**, 17378-17389 (2021).
63 Ofelt, G. J. T. j. o. c. p. Intensities of crystal spectra of rare-earth ions. **37**, 511-520 (1962).
64 Judd, B. R. J. P. r. Optical absorption intensities of rare-earth ions. **127**, 750 (1962).
65 Rabouw, F. T. *et al.* Quenching pathways in NaYF4: Er3+, Yb3+ upconversion nanocrystals. *Acs nano* **12**, 4812-4823 (2018).
66 Pavitra, E. *et al.* Evolution of Highly Biocompatible and Thermally Stable YVO4: Er3+/Yb3+ Upconversion Mesoporous Hollow Nanospheriods as Drug Carriers for Therapeutic Applications. *Nanomaterials* **12**, 2520 (2022).
67 Godinho, M. *et al.* Room temperature co-precipitation of nanocrystalline CeO2 and Ce0. 8Gd0. 2O1. 9− δ powder. **61**, 1904-1907 (2007).
68 Dell'Agli, G. *et al.* Effect of the mineralizer solution in the hydrothermal synthesis of gadolinium-doped (10% mol Gd) ceria nanopowders. **14**, 189-196 (2016).
69 Zarkov, A. *et al.* Synthesis of nanocrystalline gadolinium doped ceria via sol–gel combustion and sol–gel synthesis routes. **42**, 3972-3988 (2016).
70 Teoh, W. Y., Amal, R. & Mädler, L. Flame spray pyrolysis: An enabling technology for nanoparticles design and fabrication. *Nanoscale* **2**, 1324-1347 (2010).
71 Hartati, Y. W., Topkaya, S. N., Gaffar, S., Bahti, H. H. & Cetin, A. E. Synthesis and characterization of nanoceria for electrochemical sensing applications. *RSC advances* **11**, 16216-16235 (2021).
72 Lee, S. S. *et al.* Antioxidant properties of cerium oxide nanocrystals as a function of nanocrystal diameter and surface coating. *ACS nano* **7**, 9693-9703 (2013).
73 Song, W. *et al.* Ceria nanoparticles stabilized by organic surface coatings activate the lysosome-autophagy system and enhance autophagic clearance. *ACS nano* **8**, 10328-10342 (2014).
74 He, J. *et al.* Modulation of surface structure and catalytic properties of cerium oxide nanoparticles by thermal and microwave synthesis techniques. *Applied Surface Science* **402**, 469-477 (2017).
75 Campanati, M., Fornasari, G. & Vaccari, A. Fundamentals in the preparation of heterogeneous catalysts. *Catalysis Today* **77**, 299-314 (2003).
76 Pinna, F. Supported metal catalysts preparation. *Catalysis Today* **41**, 129-137 (1998).
77 Wu, K., Sun, L. D. & Yan, C. H. Recent Progress in Well-Controlled Synthesis of Ceria-Based Nanocatalysts towards Enhanced Catalytic Performance. *Advanced Energy Materials* **6**, 1600501 (2016).
78 Chandradass, J., Nam, B. & Kim, K. H. Fine tuning of gadolinium doped ceria electrolyte nanoparticles via reverse microemulsion process. *Colloids and Surfaces A: Physicochemical and Engineering Aspects* **348**, 130-136 (2009).
79 Das, M. *et al.* Auto-catalytic ceria nanoparticles offer neuroprotection to adult rat spinal cord neurons. *Biomaterials* **28**, 1918-1925 (2007).
80 Babu, S. *et al.* Dopant-mediated oxygen vacancy tuning in ceria nanoparticles. *Nanotechnology* **20**, 085713 (2009).
81 Alaydrus, M. *et al.* A first-principles study on defect association and oxygen ion migration of Sm3+ and Gd3+ co-doped ceria. *Journal of Physics: Condensed Matter* **25**, 225401 (2013).

82 Giannici, F. *et al.* Structure and oxide ion conductivity: local order, defect interactions and grain boundary effects in acceptor-doped ceria. *Chemistry of Materials* **26**, 5994-6006 (2014).
83 Cho, J.-H. *et al.* Up conversion luminescence of Yb3+–Er3+ codoped CeO2 nanocrystals with imaging applications. *Journal of luminescence* **132**, 743-749 (2012).
84 Han, D., Yang, Y., Gu, F. & Wang, Z. Tuning the morphology and upconversion fluorescence of CeO2: Er/Yb nano-octahedra. *Journal of Alloys and Compounds* **656**, 524-529 (2016).
85 Heiroth, S., Ghisleni, R., Lippert, T., Michler, J. & Wokaun, A. Optical and mechanical properties of amorphous and crystalline yttria-stabilized zirconia thin films prepared by pulsed laser deposition. *Acta Materialia* **59**, 2330-2340 (2011).
86 Tiseanu, C. *et al.* Surface versus volume effects in luminescent ceria nanocrystals synthesized by an oil-in-water microemulsion method. *Physical Chemistry Chemical Physics* **13**, 17135-17145 (2011).
87 Tran, T. N. L., Chiasera, A., Lukowiak, A. & Ferrari, M. Eu3+ as a Powerful Structural and Spectroscopic Tool for Glass Photonics. *Materials* **15**, 1847 (2022).
88 Fernandes, M. M. *et al.* Site-selective time-resolved laser fluorescence spectroscopy of Eu3+ in calcite. *Journal of colloid and interface science* **321**, 323-331 (2008).
89 Wang, Y. *et al.* Luminescence investigation of red-emitting Sr2MgMoO6: Eu3+ phosphor for visualization of latent fingerprint. *Journal of Colloid and Interface Science* **583**, 89-99 (2021).
90 Yang, N. *et al.* Delayed concentration quenching of luminescence caused by Eu3+-induced phase transition in LaSc3 (BO3) 4. *Chemistry of Materials* **32**, 6958-6967 (2020).
91 Dong, H., Sun, L.-D. & Yan, C.-H. Local structure engineering in lanthanide-doped nanocrystals for tunable upconversion emissions. *Journal of the American Chemical Society* **143**, 20546-20561 (2021).
92 Cybińska, J. *et al.* Spectroscopic investigation and simulation of the crystal field effect as well as paramagnetic behavior of K2La1− xPrxCl5 ternary chlorides. *Optical materials* **29**, 287-303 (2006).
93 Marmodée, B., de Klerk, J. S., Ariese, F., Gooijer, C. & Kumke, M. U. High-resolution steady-state and time-resolved luminescence studies on the complexes of Eu (III) with aromatic or aliphatic carboxylic acids. *Analytica chimica acta* **652**, 285-294 (2009).
94 Ćirić, A., Stojadinović, S. & Dramićanin, M. D. An extension of the Judd-Ofelt theory to the field of lanthanide thermometry. *Journal of Luminescence* **216**, 116749 (2019).
95 Kitagawa, Y. *et al.* Site-selective Eu3+ luminescence in the monoclinic phase of YSiO2N. *Chemistry of Materials* **33**, 8873-8885 (2021).
96 Bi, J. *et al.* Rapid ultrasonic-microwave assisted synthesis of Eu3+ doped Y2O3 nanophosphors with enhanced luminescence properties. *Journal of Materials Research and Technology* **9**, 9523-9530 (2020).
97 Binnemans, K. Interpretation of europium (III) spectra. *Coordination Chemistry Reviews* **295**, 1-45 (2015).
98 Ćirić, A., Stojadinović, S., Sekulić, M. & Dramićanin, M. D. J. J. o. L. JOES: An application software for Judd-Ofelt analysis from Eu3+ emission spectra. **205**, 351-356 (2019).
99 Đačanin, L., Lukić, S., Petrović, D. M., Nikolić, M. & Dramićanin, M. J. P. B. C. M. Judd–Ofelt analysis of luminescence emission from Zn2SiO4: Eu3+ nanoparticles obtained by a polymer-assisted sol–gel method. **406**, 2319-2322 (2011).
100 Kumar, M., Seshagiri, T. & Godbole, S. J. P. B. C. M. Fluorescence lifetime and Judd–Ofelt parameters of Eu3+ doped SrBPO5. **410**, 141-146 (2013).
101 Ćirić, A., Stojadinović, S., Sekulić, M. & Dramićanin, M. D. JOES: An application software for Judd-Ofelt analysis from Eu3+ emission spectra. *Journal of Luminescence* **205**, 351-356 (2019).

102 Gavrilović, T. *et al.* Particle size effects on the structure and emission of Eu3+: LaPO4 and EuPO4 phosphors. *Journal of Luminescence* **195**, 420-429 (2018).
103 Mondal, S. S. *et al.* White light emission of IFP-1 by in situ co-doping of the MOF pore system with Eu 3+ and Tb 3+. *Journal of Materials Chemistry C* **3**, 4623-4631 (2015).
104 Li, G. *et al.* Eu3+/Tb3+-doped La2O2CO3/La2O3 nano/microcrystals with multiform morphologies: facile synthesis, growth mechanism, and luminescence properties. *Inorganic chemistry* **49**, 10522-10535 (2010).
105 Avram, D., Porosnicu, I., Cojocaru, B., Florea, M. & Tiseanu, C. Time-gated down-/up-conversion emission of Ho–CeO2 and Ho, Yb–CeO2 nanoparticles. *Journal of Luminescence* **179**, 265-271 (2016).
106 Zhang, H., Chen, Z.-H., Liu, X. & Zhang, F. A mini-review on recent progress of new sensitizers for luminescence of lanthanide doped nanomaterials. *Nano Research* **13**, 1795-1809 (2020).
107 Chen, J. & Zhao, J. X. Upconversion nanomaterials: synthesis, mechanism, and applications in sensing. *Sensors* **12**, 2414-2435 (2012).
108 Montoya, E., Sanz-García, J. & Bausa, L. Temperature dependence of the optical properties of Yb3+ ions in LiNbO3 crystals. *Spectrochimica Acta Part A: Molecular and Biomolecular Spectroscopy* **54**, 2081-2085 (1998).
109 Kaminska, A. *et al.* Luminescent properties of ytterbium-doped ternary lanthanum chloride. *Journal of alloys and compounds* **509**, 7993-7997 (2011).
110 Lakshminarayana, G., Yang, H., Ye, S., Liu, Y. & Qiu, J. Co-operative downconversion luminescence in Tm3+/Yb3+: SiO2–Al2O3–LiF–GdF3 glasses. *Journal of Physics D: Applied Physics* **41**, 175111 (2008).
111 Kaczmarek, S. M., Tsuboi, T., Ito, M., Boulon, G. & Leniec, G. Optical study of Yb3+/Yb2+ conversion in CaF2 crystals. *Journal of Physics: Condensed Matter* **17**, 3771 (2005).
112 Kallel, T. *et al.* Spectra and energy levels of Yb3+ ions in CaF2 transparent ceramics. *Journal of alloys and compounds* **584**, 261-268 (2014).
113 Ito, M. *et al.* Crystal growth, Yb3+ spectroscopy, concentration quenching analysis and potentiality of laser emission in Ca1− xYbxF2+ x. *Journal of Physics: Condensed Matter* **16**, 1501 (2004).
114 Schaudel, B., Goldner, P., Prassas, M. & Auzel, F. Cooperative luminescence as a probe of clustering in Yb3+ doped glasses. *Journal of alloys and compounds* **300**, 443-449 (2000).
115 Dwivedi, Y., Thakur, S. & Rai, S. Study of frequency upconversion in Yb 3+/Eu 3+ by cooperative energy transfer in oxyfluoroborate glass matrix. *Applied Physics B* **89**, 45-51 (2007).
116 Bro, R. & Andersson, C. J. L. S. Chemometr. Intel. **42**, 105 (1998).
117 Claus, A. & Bro, R. J. C. I. L. S. The N-way Toolbox for MATLAB. **52**, 1-4 (2000).
118 Lin, Y., Ren, J. & Qu, X. Catalytically active nanomaterials: a promising candidate for artificial enzymes. *Accounts of chemical research* **47**, 1097-1105 (2014).
119 Korsvik, C., Patil, S., Seal, S. & Self, W. T. Superoxide dismutase mimetic properties exhibited by vacancy engineered ceria nanoparticles. *Chemical communications*, 1056-1058 (2007).
120 Liu, B., Sun, Z., Huang, P.-J. J. & Liu, J. Hydrogen peroxide displacing DNA from nanoceria: mechanism and detection of glucose in serum. *Journal of the American Chemical Society* **137**, 1290-1295 (2015).
121 Eriksson, P. *et al.* Cerium oxide nanoparticles with antioxidant capabilities and gadolinium integration for MRI contrast enhancement. *Scientific reports* **8**, 6999 (2018).
122 Sahu, T., Singh Bisht, S., Ranjan Das, K. & Kerkar, S. Nanoceria: synthesis and biomedical applications. *Current Nanoscience* **9**, 588-593 (2013).
123 Wang, G., Zhang, J., He, X., Zhang, Z. & Zhao, Y. Ceria nanoparticles as enzyme mimetics. *Chinese Journal of Chemistry* **35**, 791-800 (2017).

124 Nethi, S. K., Nanda, H. S., Steele, T. W. & Patra, C. R. Functionalized nanoceria exhibit improved angiogenic properties. *Journal of Materials Chemistry B* **5**, 9371-9383 (2017).
125 Xu, C. & Qu, X. Cerium oxide nanoparticle: a remarkably versatile rare earth nanomaterial for biological applications. *NPG Asia Materials* **6**, e90 (2014).
126 Abbas, F. *et al.* Structural, morphological, Raman, optical, magnetic, and antibacterial characteristics of CeO 2 nanostructures. *International Journal of Minerals, Metallurgy, and Materials* **23**, 102-108 (2016).
127 Eom, H.-J. & Choi, J. Oxidative stress of CeO2 nanoparticles via p38-Nrf-2 signaling pathway in human bronchial epithelial cell, Beas-2B. *Toxicology letters* **187**, 77-83 (2009).
128 Kumari, M. *et al.* Toxicity study of cerium oxide nanoparticles in human neuroblastoma cells. *International journal of toxicology* **33**, 86-97 (2014).
129 Soh, M. *et al.* Ceria–Zirconia Nanoparticles as an Enhanced Multi-Antioxidant for Sepsis Treatment. *Angewandte Chemie* **129**, 11557-11561 (2017).
130 Pratsinis, A. *et al.* Enzyme-mimetic antioxidant luminescent nanoparticles for highly sensitive hydrogen peroxide biosensing. *ACS nano* **11**, 12210-12218 (2017).
131 Menchón, C. *et al.* Gold nanoparticles supported on nanoparticulate ceria as a powerful agent against intracellular oxidative stress. *Small* **8**, 1895-1903 (2012).
132 Liu, B. & Liu, J. Surface modification of nanozymes. *Nano Research* **10**, 1125-1148 (2017).
133 Caracciolo, G., Farokhzad, O. C. & Mahmoudi, M. Biological identity of nanoparticles in vivo: clinical implications of the protein corona. *Trends in biotechnology* **35**, 257-264 (2017).
134 Heckert, E. G., Karakoti, A. S., Seal, S. & Self, W. T. The role of cerium redox state in the SOD mimetic activity of nanoceria. *Biomaterials* **29**, 2705-2709 (2008).
135 Carnovale, C., Bryant, G., Shukla, R. & Bansal, V. in *Metal Nanoparticles in Pharma* 419-436 (Springer, 2017).
136 Foroozandeh, P. & Aziz, A. A. Merging worlds of nanomaterials and biological environment: factors governing protein corona formation on nanoparticles and its biological consequences. *Nanoscale research letters* **10**, 221 (2015).
137 Nierenberg, D., Khaled, A. R. & Flores, O. Formation of a protein corona influences the biological identity of nanomaterials. *Reports of Practical Oncology & Radiotherapy* **23**, 300-308 (2018).
138 Müller, J. *et al.* Coating nanoparticles with tunable surfactants facilitates control over the protein corona. *Biomaterials* **115**, 1-8 (2017).
139 Blanco, E., Shen, H. & Ferrari, M. Principles of nanoparticle design for overcoming biological barriers to drug delivery. *Nature biotechnology* **33**, 941 (2015).
140 Yang, Z.-Y. *et al.* Alendronate as a robust anchor for ceria nanoparticle surface coating: facile binding and improved biological properties. *RSC Advances* **4**, 59965-59969 (2014).
141 Li, L.-L., Wu, P., Hwang, K. & Lu, Y. An exceptionally simple strategy for DNA-functionalized up-conversion nanoparticles as biocompatible agents for nanoassembly, DNA delivery, and imaging. *Journal of the American Chemical Society* **135**, 2411-2414 (2013).
142 Fu, J., Liu, M., Liu, Y., Woodbury, N. W. & Yan, H. Interenzyme substrate diffusion for an enzyme cascade organized on spatially addressable DNA nanostructures. *Journal of the American Chemical Society* **134**, 5516-5519 (2012).
143 Seeman, N. C. J. N. DNA in a material world. **421**, 427-431 (2003).
144 Bathe, M. & Rothemund, P. W. J. M. B. DNA nanotechnology: A foundation for programmable nanoscale materials. **42**, 882-888 (2017).
145 Heck, C., Kanehira, Y., Kneipp, J. & Bald, I. J. A. C. I. E. Placement of Single Proteins within the SERS Hot Spots of Self-Assembled Silver Nanolenses. **57**, 7444-7447 (2018).
146 Choi, Y., Schmidt, C., Tinnefeld, P., Bald, I. & Rödiger, S. J. S. r. A new reporter design based on DNA origami nanostructures for quantification of short oligonucleotides using microbeads. **9**, 1-8 (2019).

147 Choi, Y. *et al.* DNA origami-based Förster resonance energy-transfer nanoarrays and their application as ratiometric sensors. **10**, 23295-23302 (2018).
148 Grossi, G., Jaekel, A., Andersen, E. S. & Saccà, B. J. M. B. Enzyme-functionalized DNA nanostructures as tools for organizing and controlling enzymatic reactions. **42**, 920-924 (2017).
149 Kuzyk, A., Jungmann, R., Acuna, G. P. & Liu, N. J. A. p. DNA origami route for nanophotonics. **5**, 1151-1163 (2018).
150 Madhanagopal, B. R., Zhang, S., Demirel, E., Wady, H. & Chandrasekaran, A. R. J. T. i. b. s. DNA nanocarriers: programmed to deliver. **43**, 997-1013 (2018).
151 Pilo-Pais, M., Goldberg, S., Samano, E., LaBean, T. & Finkelstein, G. Connecting the nanodots: programmable nanofabrication of fused metal shapes on DNA templates. *Nano letters* **11**, 3489-3492 (2011).
152 Wang, Z.-G., Liu, Q., Li, N. & Ding, B. DNA-Based Nanotemplate Directed In Situ Synthesis of Silver Nanoclusters with Specific Fluorescent Emission: Surface-Guided Chemical Reactions. *Chemistry of Materials* **28**, 8834-8841 (2016).
153 Helmig, S. *et al.* Single molecule atomic force microscopy studies of photosensitized singlet oxygen behavior on a DNA origami template. **4**, 7475-7480 (2010).
154 Rackwitz, J. *et al.* Sensitizing DNA Towards Low-Energy Electrons with 2-Fluoroadenine. *Angewandte Chemie International Edition* **55**, 10248-10252 (2016).
155 Schürmann, R. *et al.* Resonant Formation of Strand Breaks in Sensitized Oligonucleotides Induced by Low-Energy Electrons (0.5–9 eV). *Angewandte Chemie International Edition* **56**, 10952-10955 (2017).
156 Vogel, S. *et al.* Using DNA origami nanostructures to determine absolute cross sections for UV photon-induced DNA strand breakage. *The journal of physical chemistry letters* **6**, 4589-4593 (2015).
157 Schürmann, R., Vogel, S., Ebel, K. & Bald, I. J. C. A. E. J. The Physico-Chemical Basis of DNA Radiosensitization: Implications for Cancer Radiation Therapy. **24**, 10271-10279 (2018).
158 Schneider, F. *et al.* SpraySyn—A standardized burner configuration for nanoparticle synthesis in spray flames. *Review of Scientific Instruments* **90**, 085108 (2019).
159 Angel, S. *et al.* Spray-flame synthesis of La (Fe, Co) O3 nano-perovskites from metal nitrates. *AIChE Journal* **66**, e16748 (2020).
160 Bald, I. & Keller, A. Molecular processes studied at a single-molecule level using DNA origami nanostructures and atomic force microscopy. *Molecules* **19**, 13803-13823 (2014).
161 Drobot, B. *et al.* Combining luminescence spectroscopy, parallel factor analysis and quantum chemistry to reveal metal speciation–a case study of uranyl (VI) hydrolysis. **6**, 964-972 (2015).
162 Xu, Y. *et al.* Continuous hydrothermal flow synthesis of Gd-doped CeO2 (GDC) nanoparticles for inkjet printing of SOFC electrolytes. **15**, 315-327 (2018).
163 Primus, P.-A. *et al.* High-resolution spectroscopy of europium-doped ceria as a tool to correlate structure and catalytic activity. **118**, 23349-23360 (2014).
164 Tok, A., Du, S., Boey, F. & Chong, W. Hydrothermal synthesis and characterization of rare earth doped ceria nanoparticles. *Materials Science and Engineering: A* **466**, 223-229 (2007).
165 Soni, S. *et al.* Electronic Structure and Room Temperature Ferromagnetism in Gd-doped Cerium Oxide Nanoparticles for Hydrogen Generation via Photocatalytic Water Splitting. **3**, 1800090 (2019).
166 Soni, S. *et al.* Electronic Structure and Room Temperature Ferromagnetism in Gd-doped Cerium Oxide Nanoparticles for Hydrogen Generation via Photocatalytic Water Splitting. *Global Challenges* **3**, 1800090 (2019).
167 Binnemans, K. J. C. C. R. Interpretation of europium (III) spectra. **295**, 1-45 (2015).

168 Vuković, K., Ćulubrk, S., Sekulić, M. & Dramićanin, M. D. J. J. o. R. i. P. Analysis of luminescence of Eu3+ doped Lu2Ti2O7 powders with Judd-Ofelt theory. **38**, 23-32 (2015).
169 Gavrilović, T. *et al.* Particle size effects on the structure and emission of Eu3+: LaPO4 and EuPO4 phosphors. **195**, 420-429 (2018).
170 Barve, R., Suriyamurthy, N., Panigrahi, B. & Venkatraman, B. Optical properties and Judd–Ofelt analysis of Eu3+ activated calcium silicate. *Physica B: Condensed Matter* **475**, 156-161 (2015).
171 Ramos, I. A. C. *et al.* Hydrogen production from ethanol steam reforming on M/CeO2/YSZ (M= Ru, Pd, Ag) nanocomposites. *Catalysis Today* **180**, 96-104 (2012).
172 Raharjo, J., Aninda, R. S. & Lestari, N. A. in *Journal of Physics: Conference Series.* 012077 (IOP Publishing).
173 Melchionna, M. & Fornasiero, P. The role of ceria-based nanostructured materials in energy applications. *Materials Today* **17**, 349-357 (2014).
174 Montini, T., Melchionna, M., Monai, M. & Fornasiero, P. Fundamentals and catalytic applications of CeO2-based materials. *Chemical reviews* **116**, 5987-6041 (2016).
175 Primus, P. A., Menski, A., Yeste, M. P., Cauqui, M. A. & Kumke, M. U. Fluorescence Line-Narrowing Spectroscopy as a Tool to Monitor Phase Transitions and Phase Separation in Efficient NanocrystallineCexZr−xO2:Eu3+Catalyst Materials. *Physical Chemistry*, 10682-10692 (2015).
176 Younis, A., Chu, D. & Li, S. in *Functionalized Nanomaterials* (InTech, 2016).
177 Babu, S., Schulte, A. & Seal, S. Defects and symmetry influence on visible emission of Eu doped nanoceria. *Applied Physics Letters* **92**, 123112 (2008).
178 Tiseanu, C., Parvulescu, V. I., Sanchez-Dominguez, M. & Boutonnet, M. Temperature induced conversion from surface to "bulk" sites in Eu3+-impregnated CeO2 nanocrystals. *Journal of Applied Physics* **112**, 013521 (2012).
179 Avram, D. *et al.* Heavily impregnated ceria nanoparticles with europium oxide: spectroscopic evidences for homogenous solid solutions and intrinsic structure of Eu3+-oxygen environments. *Journal of materials science* **49**, 2117-2126 (2014).
180 Prakasam, M. *et al.* Nanostructured pure and doped zirconia: syntheses and sintering for SOFC and optical applications. *Sinter. Technol. Method Appl* **85** (2018).
181 Scherrer, B. *et al.* Crystallization and microstructure of yttria-stabilized-zirconia thin films deposited by spray pyrolysis. *Advanced Functional Materials* **21**, 3967-3975 (2011).
182 Chervin, C. N. *et al.* Aerogel synthesis of yttria-stabilized zirconia by a non-alkoxide sol− gel route. *Chemistry of materials* **17**, 3345-3351 (2005).
183 Heiroth, S. *et al.* Crystallization and grain growth characteristics of yttria-stabilized zirconia thin films grown by pulsed laser deposition. *Solid State Ionics* **191**, 12-23 (2011).
184 Chervin, C. N. *et al.* Role of Cyclic Ether and Solvent in a Non-Alkoxide Sol− Gel Synthesis of Yttria-Stabilized Zirconia Nanoparticles. *Chemistry of materials* **18**, 4865-4874 (2006).
185 Wang, Z., Qu, Z., Quan, X. & Wang, H. Selective catalytic oxidation of ammonia to nitrogen over ceria–zirconia mixed oxides. *Applied Catalysis A: General* **411**, 131-138 (2012).
186 Wang, X., Liu, Y., Yao, W. & Wu, Z. Boosting the low-temperature activity and sulfur tolerance of CeZr2Ox catalysts by antimony addition for the selective catalytic reduction of NO with ammonia. *Journal of colloid and interface science* **546**, 152-162 (2019).
187 Choudhury, B., Chetri, P. & Choudhury, A. Annealing temperature and oxygen-vacancy-dependent variation of lattice strain, band gap and luminescence properties of CeO2 nanoparticles. *Journal of Experimental Nanoscience* **10**, 103-114 (2015).
188 Voron'Ko, Y. K., Osiko, V. & Shcherbakov, I. Optical centers and interaction of Yb3+ ions in cubic fluorite crystals. *Sov. Phys. JETP.* **29**, 86-90 (1969).

189 Wang, F. *et al.* Manipulating refractive index, homogeneity and spectroscopy of Yb 3+-doped silica-core glass towards high-power large mode area photonic crystal fiber lasers. *Optics express* **25**, 25960-25969 (2017).
190 Kirton, J. & McLaughlan, S. Correlation of Electron Paramagnetic Resonance and Optical-Absorption Spectra of Ca F 2: Yb 3+. *Physical Review* **155**, 279 (1967).
191 Zhang, Q. & Liang, X. Cooperative downconversion in Y3Al5O12: RE3+, Yb3+ (RE= Tb, Tm, and Pr) nanophosphors. *Journal of the Society for Information Display* **16**, 755-758 (2008).
192 Xia, L. *et al.* Preparation and characterization of sol-gel derived highly transparent aluminosilicate glass thin films with ultrahigh doping level of Yb3+ ions. *Optical Materials* **98**, 109352 (2019).
193 Li, J. *et al.* Intense upconversion luminescence and origin study in Tm3+/Yb3+ codoped calcium scandate. *Applied Physics Letters* **101**, 121905 (2012).
194 Karakoti, A. *et al.* Nanoceria as antioxidant: synthesis and biomedical applications. *Jom* **60**, 33-37 (2008).

Chapter 11 Publications, Communications and Awards

Sitshengisiwe Chemura, Toni Haubitz, Philipp A. Primus, Martin Underberg, Tim Hülser, Michael U. Kumke, Europium doped ceria-gadolinium mixed oxides: PARAFAC and high-resolution emission spectroscopy under cryogenic conditions for structural analysis J. Phys A 2020, 124, 24;

doi: 10.1021/acs.jpca.0c03188.

Oral communications

Poster presentations at the Physical Chemistry research seminar (MDDS); (Physical Chemistry, University of Potsdam):

- Monitoring reactive oxygen species (ROS) on the nanoscale - Combination of DNA origami and ceria nanoparticles., 08.2022
- Combination of ultra-low high-resolution spectroscopy and Eu^{3+}: a powerful structural probe for in homogenous samples., 07.2019

Scholarships

PhD Scholarship from the University of Potsdam Graduate School, 01.2019-06.2019

Deutsche Forschungsgemeinschaft (DFG) scholarship, 04.2021-04.2024.

Chapter 12: Acknowledgements

This study could not have been successful if it were not for the assistance, contributions and cooperation I got from organizations and individuals for which I am very grateful. I am sincerely grateful to my supervisor Prof. Michael U. Kumke whose invaluable advice, guidance, patience and wit helped me to properly shape this research work. In addition, I am grateful to my second supervisor Prof. Ilko Bald for his support. The input and support of Dr. Philipp-Alexander Primus and Dr. Anushree Dutta is also greatly appreciated in facilitating the experimental work and providing technical support especially during the first steps in tackling the subjects of the projects I was involved in. I also wish to thank my colleagues at the University of Potsdam, Physical Chemistry group, for their collaboration, advice and moral support during our biweekly AFP talks and scientific journey. I also want to thank my husband Abel, *baba vana2*, for supporting me, purifying my research ideas and proof-reading all my writings. The study also ran partly and concurrently with the University of Potsdam and Deutsche Forschungsgemeinschaft (DFG) funding that provided financial support for carrying out some aspects of this study. I also would like to thank Dr. Christina Günter for helping with the XRD measurements and Dr. Sibylle Rüstig for the TEM measurements and many more people who contributed along the way to ensure that I had a walk I will always remember. This research project and the entire study also drew a lot of inspiration from my twins Chömunoda Ayden and Taembedzwa Aàyan for whom I will always work hard for. My mum, sister and brother were a pillar of strength during my study. This is also to my dad who always told me that whatever I can dream, I can get! God gave me a wonderful and smooth journey and would like to thank Him for making all possible.

Declaration

Hiermit versichere ich, dass ich die hier vorgelegte Dissertation selbstst¨andig verfasst und keine anderen als die angegebenen Quellen und Hilfsmittel verwendet habe. Ich versichere, dass diese Arbeit noch nicht an anderer Stelle zur Erlangung des Doktorgrades eingereicht worden ist.

Potsdam, 06 June 2023

(Sitshengisiwe Chemura)